MINISTRY OF EDUCATION, RESEARCH, YOUTH AND SPORT

THE ANNALS OF “DUNAREA DE JOS” UNIVERSITY OF GALATI

Fascicle IX
METALLURGY AND MATERIALS SCIENCE

YEAR XXX (XXXV),
March 2012, no.1

ISSN 1453-083X

2012
GALATI UNIVERSITY PRESS

EDITORIAL BOARD

PRESIDENT OF HONOUR

Prof. Olga MITOSERIU - ’’Dunarea de Jos’’ University of Galati, Romania

EDITOR-IN-CHIEF

Prof. Nicolae CANANAU - ’’Dunarea de Jos’’ University of Galati, Romania

EXECUTIVE EDITOR

Prof. Marian BORDEI - ’’Dunarea de Jos’’ University of Galati, Romania

SCIENTIFIC ADVISORY COMMITTEE

Prof. Lidia BENEA – ’’Dunarea de Jos’’ University of Galati, Romania
Acad. Prof. Ion BOSTAN - Technical University of Moldova, Moldova Republic
Prof. Francisco Manuel BRAZ FERNANDES - New University of Lisbon Caparica, Portugal
Acad. Prof. Valeriu CANTSER - Academy of Moldova Republic, Moldova Republic
Prof. Jean Pierre CELIS - Katholieke Universiteit Leuven, Belgium
Prof. Anisoara CIOCAN - ’’Dunarea de Jos’’ University of Galati, Romania
Prof. Alexandru CHIRIAC - ’’Dunarea de Jos’’ University of Galati, Romania
Assoc. Prof. Stela CONSTANTINESCU - ’’Dunarea de Jos’’ University of Galati, Romania
Prof. Elena DRUGESCU - ’’Dunarea de Jos’’ University of Galati, Romania
Prof. Valeriu DULGHERU - Technical University of Moldova, Moldova Republic
Prof. Jean Bernard GUILLOT – École Centrale Paris, France
Assoc. Prof. Gheorghe GURAU - ’’Dunarea de Jos’’ University of Galati, Romania
Prof. Iulian IONITA – ‘‘Gheorghe Asachi’’ Technical University Iasi, Romania
Prof. Philippe MARCUS - École Nationale Supérieure de Chimie de Paris, France
Prof. Vasile MARINA - Technical University of Moldova, Moldova Republic
Prof. Rodrigo MARTINS–NOVA University of Lisbon, Portugal
Prof. Strul MOISA - Ben Gurion University of the Negev, Israel
Prof. Daniel MUNTEANU - Transilvania University of Brasov, Romania
Prof. Viorel MUNTEANU - ’’Dunarea de Jos’’ University of Galati, Romania
Prof. Viorica MUSAT - ’’Dunarea de Jos’’ University of Galati, Romania
Prof. Maria NICOLAE - Politehnica University Bucuresti, Romania
Prof. Petre Stelian NITA - ’’Dunarea de Jos’’ University of Galati, Romania
Prof. Pierre PONTHIAUX – École Centrale Paris, France
Prof. Florentina POTECASU - ’’Dunarea de Jos’’ University of Galati, Romania
Assoc. Prof. Octavian POTECASU - ’’Dunarea de Jos’’ University of Galati, Romania
Prof. Cristian PREDESCU - Politehnica University Bucuresti, Romania
Prof. Iulian RIPOSAN - Politehnica University Bucuresti, Romania
Prof. Rami SABAN - Politehnica University Bucuresti, Romania
Prof. Antonio de SAJA - University of Valladolid, Spain
Prof. Wolfgang SAND - Duisburg-Essen University Duisburg Germany
Prof. Ion SANDU – ’’Al. I. Cuza’’ University of Iasi
Prof. Georgios SAVAIDIS - Aristotle University of Thessaloniki, Greece
Prof. Ioan VIDA-SIMITI - Technical University of Cluj Napoca, Romania
Prof. Mircea Horia TIEREAN - Transilvania University of Brasov, Romania
Assoc. Prof. Petrica VIZUREANU – ‘‘Gheorghe Asachi’’ Technical University Iasi, Romania
Prof. Maria VLAD - ’’Dunarea de Jos’’ University of Galati, Romania
Prof. François WENGER – École Centrale Paris, France

Table of Content

1. Alexandrina TEODORU, Tănase PANAIT, Krisztina UZUNEANU, Daniela TASMA, Cătălin MOCANU - Setting the Optimum Angle of Solar Collectors Settlement 5

2. Anişoara CIOCAN, Lucica BALINT - Reducing the Zinc Emissions by Upgrading of Steel Scraps Quality........ 10

3. A.M. CANTARAGIU, M.D. GAVRIL (DONOSE), D.C. VLADU (RADU), C. GHEORGHIES, N. TIGAU, C.M. CANTARAGIU - Copper Plating Corrosion Study in Certain Environments........ 18

4. Constantin GHEORGHIES, Mihaela BUCIUMEANU, Dan SCARPETE, Livia GHEORGHIES, Dorian BOLD - A Test for Rapid Tribological Characterization of Bearing Steels........ 25

5. Elisabeta VASILESCU, Ana DONIGA - Modern Approaches in Design Optimization of Parts and the Development Trend of Surface Treatments........ 30

6. Viorica VASILACHE, Dan APARASCHIVEI, Ion SANDU, Violeta VASILACHE, Ioan Gabriel SANDU - Integrated Analytical Study for the Somes Metalic Artefact Discoveri in Ibida Site, Romania........ 36

7. Daniela TASMA, Tănase PANAIT, Krisztina UZUNEANU, Cătălin MOCANU, Raluca-Cristina BUŢURCĂ - Composition of Syngas Produced by Gasification of Agricultural Residue Briquettes........ 42

8. Tamara RADU, Anisoara CIOCAN, Maria VLAD, Stela CONSTANTINESCU - Obtaining and Characterizing Tin-Lead Coatings on Steel Band........ 46

9. Stela CONSTANTINESCU, Maria VLAD, Tamara RADU - Characterisation of CVD Niobium Carbide Coatings on Hard Carbide Substrate........ 51

10. Stefan DRAGOMIR, Nicolae DIACONU, Marian BORDEI - Vibrations and Torque Monitoring Processes for a Cold Rolling Mills........ 56

11. Eliza MARDARE, Lidia BENEA, Jean-Pierre CELIS - Influence of Normal Loads on Corrosion Behaviour of Ti-6Al-4V Alloy during Fretting in Artificial Saliva........ 62

12. Anca-Ionela DANCIU, Viorica Muşat, Tito BUSANI, Alexandra Gonçalves, Joana V. PINTO, Mafalda COSTA, Iwona BERNACKA-WOJCIK, Rodrigo MARTINS, Elvira FORTUNATO - Selective Growth of 1D Nanostructures Oxide Materials Using PDMS Stamp........ 67

13. Virgil GEAMĂN, Mihai Alin POP, Vasile JIMAN - Aluminum Foams with Closed Pores Obtained by Casting Techniques........ 71

14. Ioan CARCEA, Oana BĂLŢĂTESCU, Raluca-Maria FLOREA - Aspects Regarding the Tradition of Bell Manufacture and Use........ 74

THE ANNALS OF “DUNAREA DE JOS” UNIVERSITY OF GALATI.
FASCICLE IX. METALLURGY AND MATERIALS SCIENCE
N^0. 1 – 2012, ISSN 1453 – 083X

SETTING THE OPTIMUM ANGLE OF SOLAR COLLECTORS SETTLEMENT

Alexandrina TEODORU, Tănase PANAIT, Krisztina UZUNEANU, Daniela TASMA, Cătălin MOCANU
“Dunărea de Jos” University of Galati
email: dtasma@ugal.ro

ABSTRACT

The performance of any solar energy system depends very much on the availability of solar radiation and the orientation of solar collectors. Solar collectors need to be inclined at the optimum angle to maximize the receiving energy. In this work, we proposed to analyze the optimum tilt angle for compound parabolic collectors CPC with different concentration ratios. There are analyzed the energy gains when the collector keeps the same position during the whole year and when the collector changes its tilt twice a year, in summer and in winter.

KEYWORDS: solar collectors, CPC, orientation, optimum tilt angle, useful energy gain

1. Introduction

The conversion of renewable energies becomes more important day by day, because of the conventional fuels cost and the environmental pollution. Solar energy is one of these renewable energies which can be converted directly into electricity or into heat. The efficiency of solar collector depends on many factors: design, construction, position, orientation, climatic condition of the place, application for which they are used. The best way to collect maximum solar energy is to optimize the position and orientation of solar collectors.

The factors which affect the value of the optimum tilt angle are [1]:

–the type of application, i.e. stand alone or grid connected;

–maximization the amount of collectable radiation for the whole year or a certain period of time;

–actual climatic condition of the site, regarding snow fall, dust storms or polluted air.

Many papers present optimum tilt angle of the collectors for different locations. Moghadam et al [2], determined the optimum tilt angle for each month of the year, for the first half and the second half of the year and for the whole year. First half, second half and annual optimum tilt β were determined as $\beta=\Phi-23^o$, $\beta=\Phi+23^o$, $\beta=\Phi$, where Φ is the latitude. Shariah et al [3] concluded that for the chosen location, Jordan, the system is operating with sufficiently high solar fraction when the tilt angle is $\beta=\Phi+(0^o\rightarrow10^o)$ for the northern region and $\beta=\Phi+(0^o\rightarrow20^o)$ for the southern region. Skeiker [1] developed an analytical procedure to obtain formulas which require the least number of parameters to determine the angle β for any chosen day, latitude and for any value of the surface azimuth angle. The results of Gunerhan [4] and Elminir [5] suggest that for the systems which utilize solar energy throughout the year, the optimum tilt angle is taken to be equal to the location latitude, while for summer $\beta=\Phi-15^o$ and for winter $\beta=\Phi+15^o$. Yakup [6] concluded that changing the tilt angle 12 times in a year (monthly changing), the solar radiation gain increases by 4.5% more than the case of a horizontal stationary collector ($\beta=0$). Also, his studies show an increase of 3.9% of solar energy gain when the tilt angle is changed four times a year (seasonal optimum tilt angle).

Being stationary and producing concentration, the CPC collects solar radiation for a more limited time than flat plate collectors. This time depends on its design (concentration ratio) and orientation. To estimate the absorbed radiation it is necessary to determine the instance at which acceptance of the sun’s beam radiation begins and stops for the considered collector [7].

This paper presents one comparison between useful energy gains for CPC for different tilt angles.

There was considered the tilt angle when the collector has the same position during the whole year and when the position of the collector is changed twice for a year (in spring and in autumn). The diffuse radiation and total radiation data values used in this work were taken from „Instituto Nacional de Meteorologia e Geofisica”, [8] for the city of Porto, in Portugal. This city is located on latitude 41° N and longitude 8° W [8], in northern Portugal.

2. Sun’s position

The azimuth angle (γ_s) and the zenith angle (θ_s) are the angles which describe the sun’s position (Fig. 1) [9], [10].

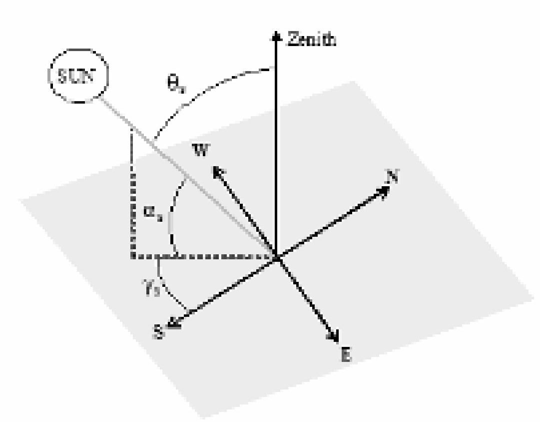

Fig. 1. *Sun’s position*

These two angles are defined by the equations (1) and (2):

$$\cos\theta_S = \sin\delta\sin\Phi + \cos\delta\cos\Phi\cos h = \sin\alpha_S \quad (1)$$

$$\cos\gamma_S = \frac{\sin\alpha_S\sin\Phi - \sin\delta}{\cos\alpha_S\cos\Phi} \quad (2)$$

In these equations, Φ is the location latitude, δ is the declination given by equation (3) and h is the hour angle determined by equation (4).

$$\delta = 23.35\sin\frac{360(284+d)}{365} \quad (3)$$

where d is the day of year starting from the first of January:

$$h = -15(12 - \text{hour}) \quad (4)$$

The position of the sun can be described by the terrestrial horizon coordinate system, where axis V represents the vertical direction, axis E points the east and axis S points south (Figure 2). In this coordinate system, the unit vector from the earth to the sun can be expressed by [7], [11]:

$$\overline{SUN} = (\cos\sigma\overline{S}\ ,\cos\xi\overline{V}\ ,\cos\pi\overline{E}\,) \quad (5)$$

where:

$$\cos\sigma = -\sin\delta\cos\Phi + \cos\delta\sin\Phi\cos h \quad (6)$$

$$\cos\xi = \sin\delta\sin\Phi + \cos\delta\cos\Phi\cos h \quad (7)$$

$$\cos\pi = \cos\delta\sin h \quad (8)$$

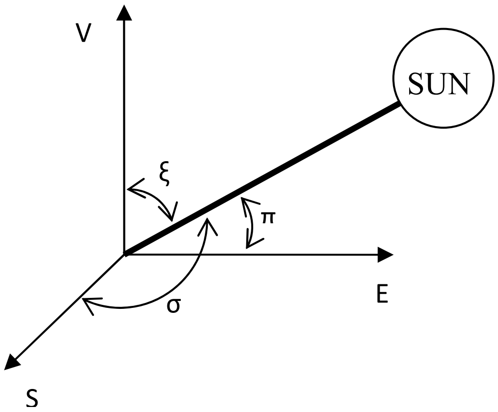

Fig. 2. *Angles for the Sun*

3. Collection angle

The collection angle (θ_c) must be calculated and compared to the acceptance half-angle θ_a (Figure 3), to determine when the CPC is receiving energy from the sun. This angle θ_c represents the angle between sun’s position vector and normal to the collector surface projected onto the transverse plane (Fig. 3).

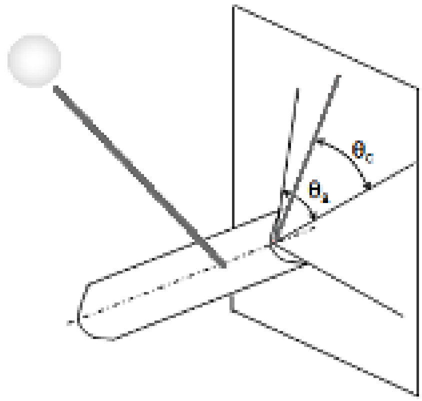

Fig. 3. *Representation of collection angle and acceptance half angle*

The position of a CPC collector is determined by three angles, the tilt β, surface azimuth and rotation ω. When all these angles are zero, the collector is horizontal and oriented east-west.

The tilt angle β represents the tilt of surface with respect to the horizontal.

The azimuth angle γ shows the orientation in relation to the east-west direction.

Therefore, when the azimuth surface angle γ=0°, the collector is orientated east-west and when γ=90°, it is orientated north-south. The rotation angle ω is resulting from a rotation around an axis perpendicular to the collector surface.

The collection angle is given by [7]:

$$\theta_c = \operatorname{atan} \frac{S_c}{V_c} \qquad (9)$$

where:

$$S_c = (\cos\omega\cos\beta\cos\gamma - \sin\omega\sin\gamma)\cos\sigma - (\cos\omega\sin\beta)\cos\xi + (\cos\omega\cos\beta\sin\gamma + \sin\omega\cos\gamma)\cos\pi \qquad (10)$$

and:

$$V_c = (\sin\beta\cos\gamma)\cos\sigma + (\cos\beta)\cos\xi + (\sin\beta\sin\gamma)\cos\pi \qquad (11)$$

4. Results and discussions

Table 1 presents the collector tilt optimized for different concentration ratios, for the whole year. The maximum useful energy gain is for a concentration of C=2 and a tilt of 15° less than the latitude of the location.

The results are presented in Table 2, where we can state that the optimal gain for summer is a concentration ratio of C=3 and a tilt of Φ -21, but for winter the optimal is for C=5 and Φ +13.

Table 1. *The optimum tilt angles for different concentration ratio, when γ=0 and ω=0 for entire year*

C (concentration ratio)	**β (tilt angle)**	**Q (useful energy gain)**
		[kWh/m^2]
1	Φ-20	96.431
1.2	Φ -19	95.042
1.5	Φ -18	97.898
1.7	Φ -20	98.556
2	Φ-15	100.89
2.5	Φ -9	99.795
3	Φ -9	91.809
3.5	Φ -18	91.658
4	Φ -16	89.088
4.5	Φ -22	78.928
5	Φ -21	77.676

Table 2. *The optimum tilt angles for different concentration ratio, when γ=0 and ω=0 for summer and winter*

C (concentration ratio)	**β (tilt angle)**	**Q (useful energy gain)**	**β (tilt angle)**	**Q (useful energy gain)**	**Q (useful energy gain)**
		[kWh/m^2]		[kWh/m^2]	
	Summer		Winter		Year
1	Φ -23	86.065	Φ +2	11.91	97.975
1.2	Φ -23	84.258	Φ +2	12.668	96.926
1.5	Φ -23	85.747	Φ +3	14.435	100.182
1.7	Φ -23	87.035	Φ +4	15.686	102.721
2	Φ-23	89.248	Φ +5	17.419	106.667
2.5	Φ -25	91.248	Φ +4	19.771	111.019
3	Φ -21	92.923	Φ +8	21.376	114.299
3.5	Φ -18	91.658	Φ +10	22.522	114.18
4	Φ -16	89.088	Φ +13	23.396	112.484
4.5	Φ -22	78.928	Φ +15	24.089	103.017
5	Φ -21	77.676	Φ +13	24.2	101.876

In Fig. 4 is shown the energy gain when the collector tilt is optimizing for different concentration ratios for the whole year (ω=0, γ=0) compared to the energy gain when the tilt angle is equal by latitude.

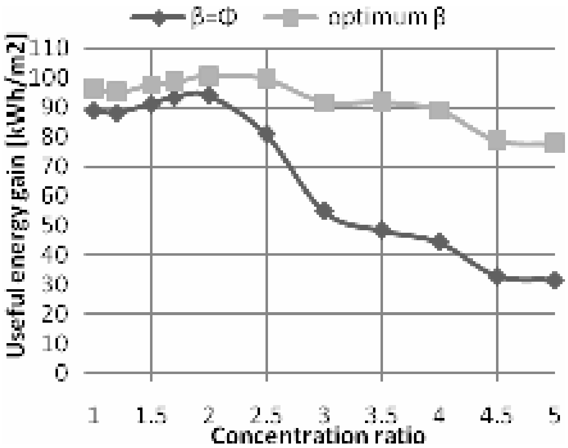

***Fig. 4.** Energy gain for the tilt equal by latitude and the optimum tilt*

Another possibility for enhancing the useful energy gain of the whole year is to change the position (tilt) of the south facing collector twice a year, one angle for the summer and another for the winter.

We considered that the tilt angle in changed seasonally twice a year, one time in April and the second time in October. Fig. 5 shows the increase of useful energy gain when the tilt angle is changed twice for a year.

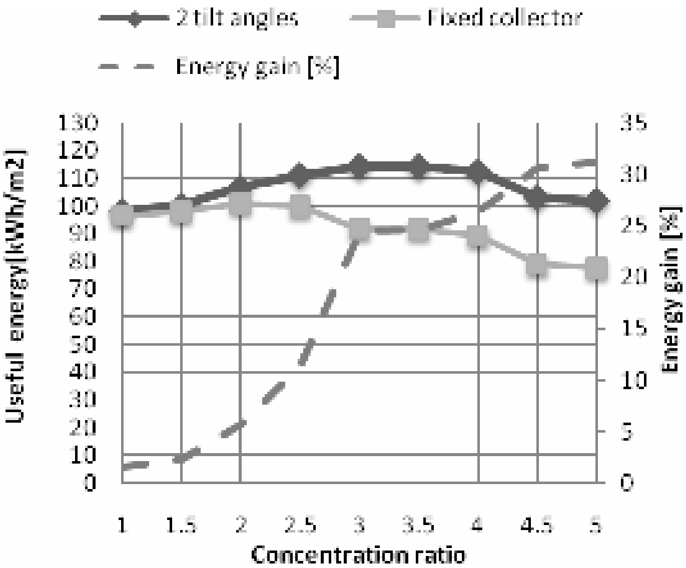

***Fig. 5.** The useful energy gain against concentration ratio and collector tilt angle for fixed collectors and changing the tilt angle twice (summer and winter)*

5. Conclusions

In this paper were analyzed the influence of the tilt angle when the collector has the same position during the whole year and when the tilt angle is changed twice for a year (in spring and in autumn).

From this study the following conclusions can be drawn:

1) When the collector tilt is optimizing for different concentration ratios for the whole year ($\omega=0$, $\gamma=0$), the result was the same, with the maximum useful energy gain being for a concentration of C=2 and a tilt of 15° less than the latitude of the location.

2) When the tilt angle is changed twice in a year, the useful energy gain increases. The gain is better for concentration ratio up to C=3 and it is more than 23%.

Acknowledgements

The work described in this paper was supported by Project SOP HRD - SIMBAD 6853, 1.5/S/15 - 01.10.2008 and by Project SOP HRD – EFICIENT 61445/2009.

References

[1]. Skeiker, K. - *Optimum tilt angle and orientation for solar collectors in Syria*, Energy Conversion and Management 502439–2448, (2009).

[2]. Moghadam, H. et al. - *Optimization of solar flat collector inclination*, Desalination, (2010).

[3]. Adnan Shariah, M-Ali Al-Akhras, I.A. Al-Omari - *Optimizing the tilt angle of solar collectors*, Renewable Energy 26, (2002).

[4]. Huseyin Gunerhan, Arif Hepbasli - *Determination of the optimum tilt angle of solar collectors for building applications,* Building and Environment 42, (2007).

[5]. Hamdy K. Elminir, Ahmed E. Ghitas, F. El-Hussainy, R. Hamid, M.M. Beheary, Khaled M. Abdel-Moneim - *Optimum solar flat-plate collector slope: Case study for Helwan, Egypt*, Energy Conversion and Management 47, (2006).

[6]. Mohd Azmi bin Hj Mohd Yakup, A.Q. Malik - *Optimum tilt angle and orientation for solar collector in Brunei* Darussalam, Renewable Energy 24, (2001).

[7]. J.M. Pinazo, J. Canada, F. Arago - *Analysis of the Incidence Angle of the Beam Radiation on CPC*, Solar Energy 49, (1992).

[8]. *** - *Boletim Actinometrico de Portugal,* Instituto Nacional de Meteorologia e Geofisica, ISSN 0870 – 4740, (1989).

[9]. R. E. Parkin - *Solar angles revisited using a general vector approach,* Solar Energy 84, (2010).

[10]. Duffie, J.A,. Beckman, W. A. – *Solar Engineering of Thermal Processes,* (1980).

[11]. Runsheng Tang, Wenfeng Gao, Yamei Yu, Hua Chen - *Optimal tilt-angles of all-glass evacuated tube solar collectors,* Energy 34, (2009).

THE ANNALS OF "DUNAREA DE JOS" UNIVERSITY OF GALATI.
FASCICLE IX. METALLURGY AND MATERIALS SCIENCE
N^0. 1 – 2012, ISSN 1453 – 083X

REDUCING THE ZINC EMISSIONS BY UPGRADING OF STEEL SCRAPS QUALITY

Anișoara CIOCAN, Lucica BALINT
Faculty of Metallurgy, Materials Science and Environment
"Dunarea de Jos" University of Galati
email: aciocan@ugal.ro

ABSTRACT

The steel production is one of the major sources of heavy metals emissions to the environment. There are several possibilities for prevention and minimization of these pollutants. Emission reduction measures focus on add-on technologies and process modifications (including operating control). The prevention of the raw materials use that may have an unacceptable environmental impact in steel manufacture is important in achieving good environmental performance. A preventive measure specified by steel making BAT is the lowering the zinc-content of scraps. A way to make this possible is to treat these scraps before their charging in the furnace (BOF or EAF). In this paper a method for removing zinc surface layers of galvanized steel scraps is studied. The principle of separation is based on the difference in vapor pressures and stabilities with the formation of zinc and iron chlorides. A series of thermal experiments was carried out in an atmosphere of gaseous HCl. As result of the treatment applied on galvanized steel samples, zinc surface layers were removed and steel scraps remain unattacked.

KEYWORDS: zinc emission, steelmaking process, galvanized scrap cleaning, chlorination

1. Introduction

In the conventional integrated steel manufacturing process, the ferrous scraps along with iron from the blast furnace in molten form are converted to steel in a basic oxygen furnace (BOF).

Also the scraps form the metallic feedstock for obtaining the steels in an electric arc furnace (EAF).

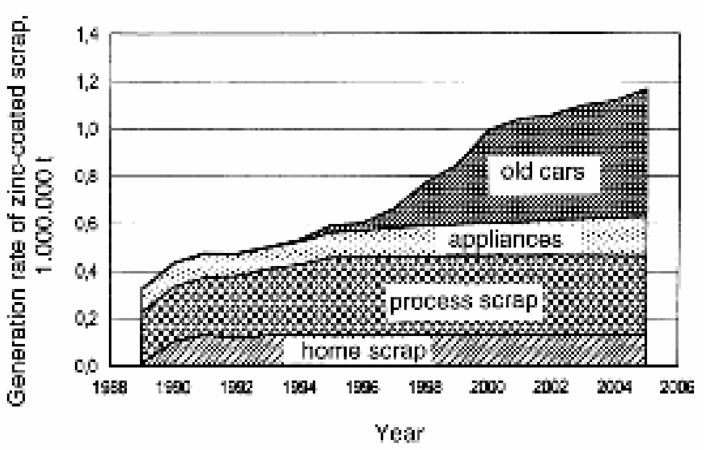

Fig. 1. *Development of the generation rate of scrap from zinc-coated steel in Germany*

This feedstock for steel manufacturing encompass a variety of different steel scraps and qualities derived from three categories: home scrap arising during steel making, process scrap from steel use and obsolete scrap at the end of the products' lifetime. Many of obsolete scraps are contaminated with galvanized coatings. In accordance with continued development of the production of zinc-coated steel the quantity of obsolete scrap originating from zinc-coated steel has registered a permanent increasing in the past years, Figure 1 [1 - 3].

The coating weight of these protective layers (Figure 2) varies from 40g/m^2/2-sides for coating weight obtained on electrogalvanized steel sheet to 610g/m^2/2-sides for coating weight deposed by hot dip galvanized process [4].

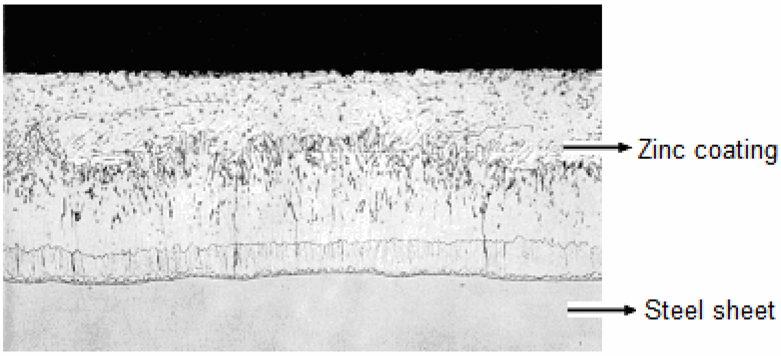

Fig. 2. *Cross section of galvanizing coating at surface of the steel sheets*

In terms of environmental the presence of zinc in steel scraps is undesirable, because more important part of this will eliminate as pollutant from steel making processes.

Large amounts of galvanized steel are produced world-wide, which will lead to the generation of dusts/sludges with a relatively high Zn content when the steel will become available as scrap in the steelmaking process. Moreover dust emissions contain higher levels of zinc and other heavy metals contained in the zinc coating. As result the steel production is a major source of zinc emissions. When galvanized scrap is melted in a steelmaking furnace, the zinc is volatizes and emitted as Zn oxide mainly airborne in the flue gas. At most BOF zinc is mainly emitted from the converter in the first few minutes of oxygen blowing.

All zinc emitted is transferred to air emissions from steel manufacturing using the BOF may include PM (ranging from less than 15kg/t to 30kg/t of steel). The stricter regulations about environmentally protection require flue gas treatment. Several methods (dry or/and wet) already used to clean up the environment from this kind of contaminant [5]. Most of them are costly.

The costs of the recycling technologies for the resulting zinc-laden dust and sludge by-products are also significant. Increased levels of zinc in the BOF dust make its usual recycling route via the sinter plant/blast furnace problematic because of the harmful effects of zinc in the blast furnace. By other hand at cleaning methods application is difficult to get optimum results. Thus its emission to air remains significant: as particulate matter and also as fumes produced for example during charging, tapping and casting. Zinc emission to water from wet dedusting process must be considered. Wastewaters generated from steel manufacturing using the BOF include 14 mg/L zinc. This BOF scrubber discharge water usually requires treatment to lower its zinc content. As a consequence of the major problems associated of this pollutant and its persistence in contaminated soil when it is finally deposed (contamination of soil appears to be virtually permanent because the first half-life of zinc, for soils in lysimetric conditions, varies greatly between 70 to 510 years [6]), the zinc emissions must be perpetually monitored. For BOFs integrated into iron and steel manufacturing plants, specific emission value for zinc is 8.2 g/t liquid steel. The target of zinc emission level per metric ton of product is 3g. Also maximum value for zinc emission into effluents from iron and steel manufacturing plants must be 2 milligrams per liter. According to recommendations PARCOM-ATMOS, the zinc emission level in the dust emitted at melting for EAF process is in the range 20-90g/t [7]. BATs on the Production of Iron and Steel Associated Emission levels recommend the following values for zinc [8]:

- BAT Associated Emission Levels for Emissions to Air

  - Emission Level of zinc = 5 - 10 mg/m^3

- BAT Associated Emission Limits for Discharges to Water

  - Emission Level of zinc = 0.5mg/L unless otherwise stated.

To prevent and minimize the presence of zinc and other heavy metals from the surface of the protected steel scraps, must to implement the operating practices e.g. to remove zinc-bearing components prior to recycling in secondary steel facilities.

The lowering of the zinc-content of scrap is distinguished as process-integrated measure recommended among the techniques considered in the determination of BAT for the steel industry. Techniques to consider in the determination of BAT In the literature there are several methods described to remove coatings from the surface of scrap that are efficient to zinc recycling. These can be divided into two main principles: leaching and thermal treatment. Research regarding leaching based on acid solutions (HCl, H_2SO_4) and basic solutions (NaOH) are covered in the literature [9]. In 1987, Argonne and its industrial partner, Metal Recovery Industries, U.S., Inc., sought to develop a new technology for converting galvanized scrap to clean scrap for steel making. The zinc is dissolved in a hot-water solution (70 to 90°C) of about 20 to 32% sodium hydroxide [10]. The metal chlorides formed by gaseous HCl released by the pyrolysis of PVC to remove surface layers from plated materials were proposed [2, 11-14] have been concentrated on the possibility to vaporize coatings with an air and chlorine gas mixture. Chlorination method was studied for recycling galvanized steel scrap. In this paper a method for removing zinc surface layer from the surface of the galvanized steel scraps is studied. The principle of separation is based on the difference in vapor pressures and stabilities with the formation of zinc and iron chlorides. A series of thermal experiments was carried out in an atmosphere of gaseous HCl.

As result of the treatment applied on galvanized steel samples, zinc surface layer was removed and steel scrap was remaining unattached. The economic removal and recovery of the zinc coating from scrap prior to melting would provide a number of cost and especially environmental advantages. The recovery of the zinc from the chemical solution is easily. Air and chlorine are readily available, and volatile chlorides are easy to separate

2. Experimental and materials

Experiments were carried out in a precinct which was placed in a chamber furnace, Figure 3. Air with gaseous HCl was mixed to obtain an atmosphere that was constantly maintained and utilized for obtaining an acceptable rate of removal. In accordance with literature an O_2:Cl_2 molar ratio of 10:1 is used [13, 15].

The literature specified that in these conditions the metal losses are acceptable and the chlorine is selectively reacting with the zinc.

Heat treatments were conducted at variable temperatures from 570 to 860^{0}C to establish the optimum thermal regime. Each sample was maintained then minutes to a constant temperature preheating and then it was slowly cooled in the air.

For the zinc-plated steel samples the electrolytic galvanized sheet scraps from car body were used.

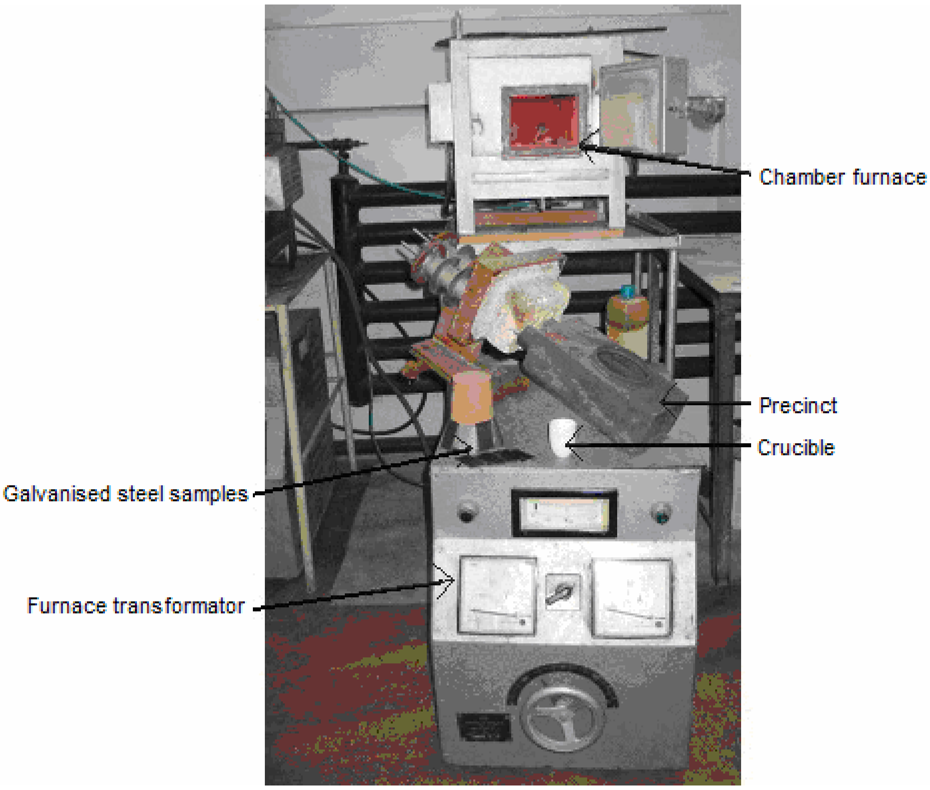

Fig. 3. *Experimental installation for the galvanized steel scraps treatment*

3. Results and discussions

Each test used hydrochloric acid as the chlorine source. The removal of the zinc coating is based on its evaporating in this gas phase. The optimum process parameters were established by analyzing the vapors pressures of chlorides of metals (Figure 4).

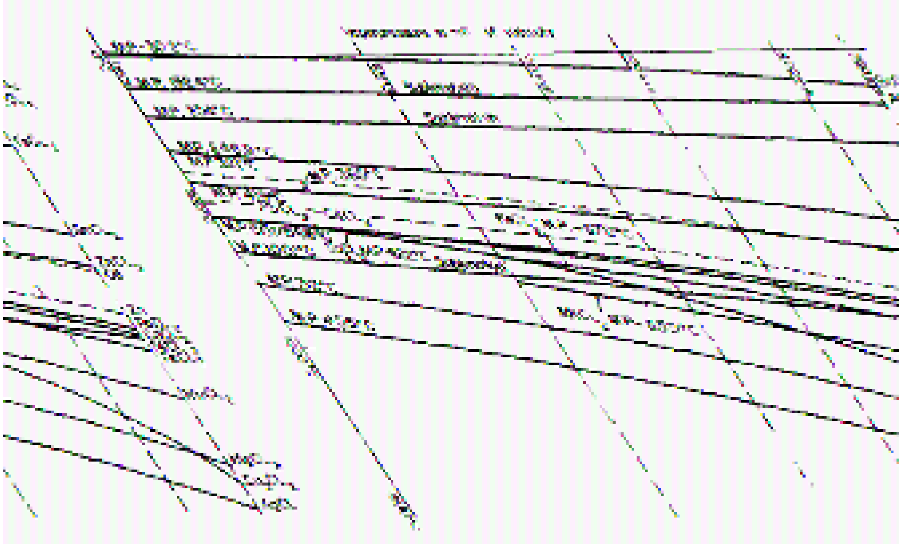

Fig. 4. *Vapors pressures of chlorides for some relevant metals [16]*

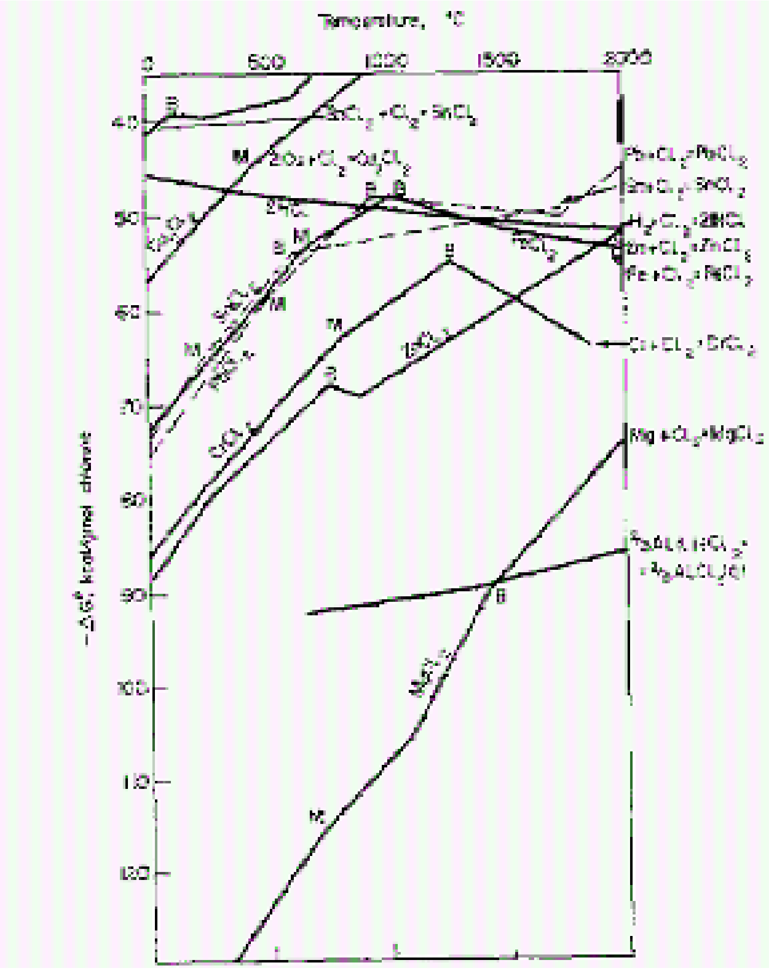

Fig. 5. *Standard free energies of formation for metal chlorides [16]*

Also has been taken into account the standard free energies of the metals chlorides formation as functions of the temperature (Figure 5). The possible reactions together with their respective standard free energy changes (ΔG^0) are given in the following equations (Table 1).

Table 1. *Standard free energy changes, ΔG^0 [18]*

Reactions	ΔG^0, kJ/mol (at 800 ^{0}C)
$Zn(l) + Cl_2(g) \rightarrow ZnCl_2(g)$	- 272.430
$Zn(l) + 1/2\ O_2(g) \rightarrow ZnO$	- 240.160
$ZnO + Cl_2(g) \rightarrow ZnCl_2(g) + 1/2\ O_2(g)$	- 32.270
$Fe + 1/2\ O_2(g) \rightarrow FeO$	- 202.347
$3\ FeO + 1/2\ O_2(g) \rightarrow Fe_3O_4$	- 163.111
$2\ Fe_3O_4 + 1/2\ O_2(g) \rightarrow 3\ Fe_2O_3$	- 86.371
$Fe_3O_4 + 9/2\ Cl_2(g) \rightarrow 3\ FeCl_3(g) + 2\ O_2(g)$	+ 73.550
$Fe_2O_3 + 3\ Cl_2(g) \rightarrow 2\ FeCl_3(g) + 3/2\ O_2(g)$	+ 77.831

The zinc removal is greatly dependent on the gas composition and temperature.

The thermodynamically data show that under reducing conditions only volatile zinc is thermodynamically stable, whereas under oxidizing conditions solid ZnO and volatile $ZnCl_2$ are present in about equivalent amounts. Up to a temperature of about 1900 ^{0}C, $ZnCl_2$ is more stable than $FeCl_2$. Moreover $ZnCl_2$ is more volatile than $FeCl_2$.

Up to temperatures of about 670 ^{0}C, the vapors pressure of $FeCl_2$ is almost zero. Formation of $FeCl_2$ will be suppressed as long as metallic zinc is present. The phase stability diagram (Figure 6) shows that with an O_2:Cl_2 ratio of 10:1, zinc exists as $ZnCl_2$ and iron as hematite, Fe_2O_3 [15].

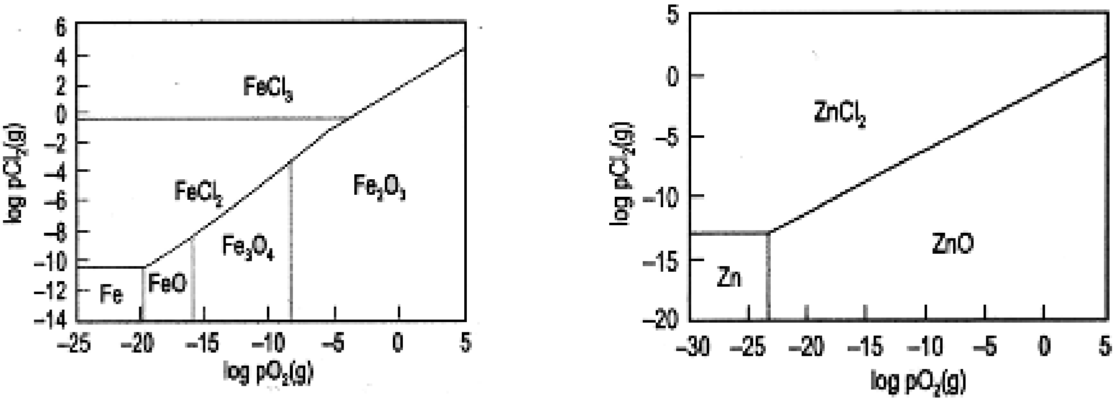

a b

Fig. 6. *Phase stability diagrams for the systems Fe-O_2-Cl_2 (a) and Zn-O_2-Cl_2 (b) [13]*

During chlorination at the varied heating temperatures, the appearance of the galvanized steel samples is modified. Their aspects are dependent which on the gas composition also. Theirs comparable evolution is given in Figure 7.

A lower temperature the zinc removal rate is significantly reduced.

The high zinc removal efficiency as result of fast reaction was developed at high temperature (up to 700ºC): at 570^{0}C, small areas of the unconsumed zinc coating (grey areas) and zinc free-zone composed by the ferric oxide (red areas) are present (Figure 7b); ferric oxide is greatly extended of the all area (homogeneous red areas) at 680^{0}C and small oxide areas are detached from the surface sample (Figure 7c); at 790^{0}C and decreasing of the chlorination conditions ferric oxide areas (red color) alternate with ferroferric oxide areas (black color) appear (Figure 7d); at 860^{0}C, Fe_2O_3 are predominantly (Figure 7e).

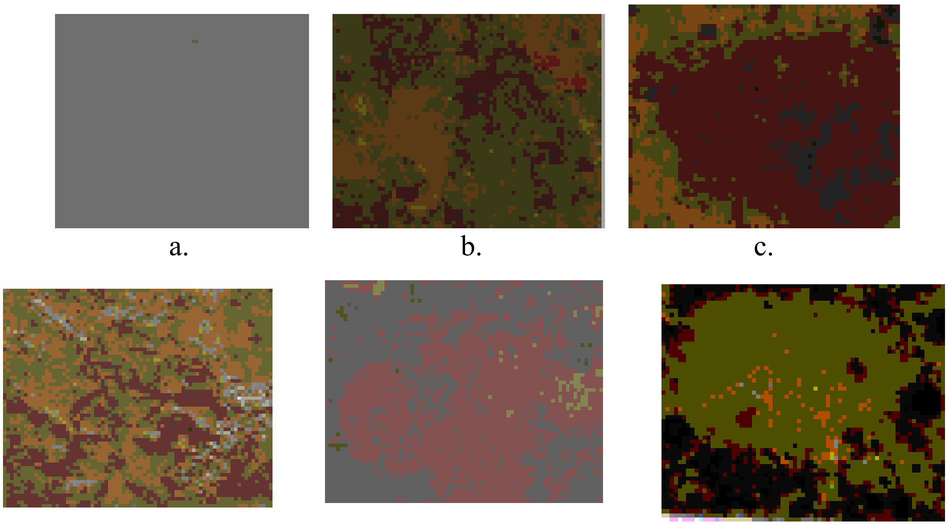
a. b. c.
c. d. e.

Fig. 7. *Aspect of samples after chlorination at different heating temperatures: initial steel sample before its heating (a); 570 ^{0}C (b); 680 ^{0}C (c); 790 ^{0}C (d); 860 ^{0}C (e)*

The microstructural analyses of selected samples reveal the removal of zinc coating at preheating of steel samples into chlorine atmosphere, Figures 8-10. The selected samples were those from 570, 680 and 860^{0}C.

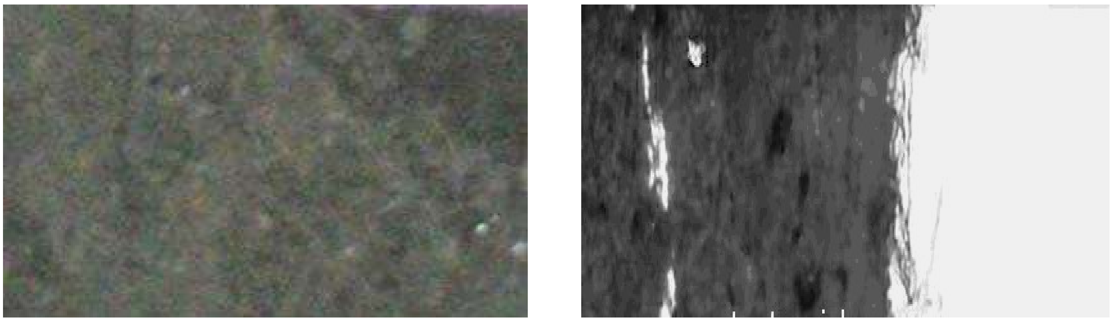
a b

Fig. 8. *Surface of the zinc coated steel scrap after treatment (temperature 570^{0}C) (a) and microstructure of the sample (500x) (b)*

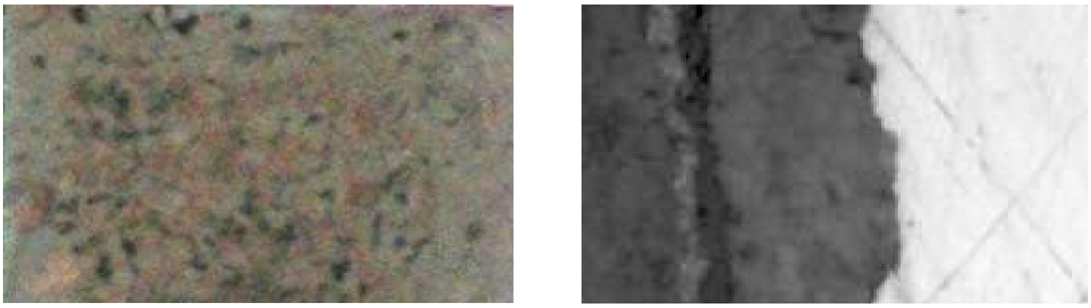
a *b*

Fig. 9. *Surface of the zinc coated steel scrap after treatment (temperature 680^{0}C) (a) and microstructure of the sample (500x) (b)*

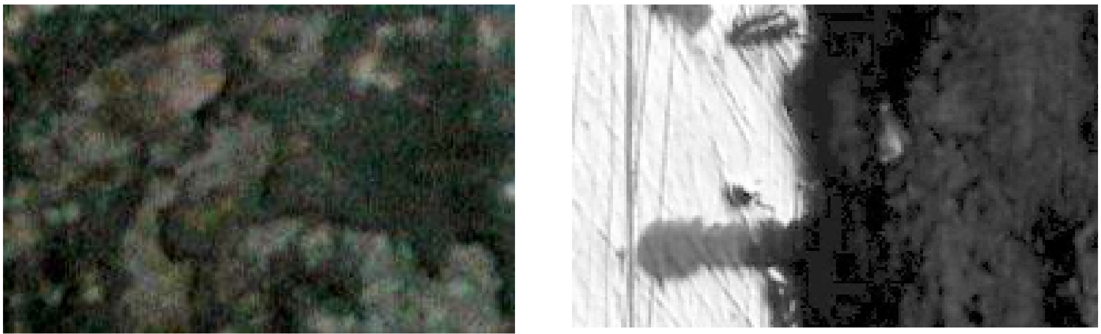

***Fig. 10.** Surface of the zinc coated steel scrap after treatment (temperature 860 ^{0}C) (a) and microstructure of the sample (500x) (b)*

For the treatment at temperature up to 800 ^{0}C, the structural analyze put in evidence a strongly oxidized zone with intergrains attack (about 5 - 6μm depth). The steel is corroded and the iron oxides Fe_2O_3 and Fe_3O_4 are formed (thickness of this layer is about 12 - 13μm). In this case the quality of the steel scrap is affected by oxidizing process of iron.

4. Conclusions

The removal of the zinc as contaminant from steel scrap leads to upgrading the steel scrap quality. The quantity of the Zn-containing dust and arising in the flue gas produced at steel making process is reduced. That led to diminishing of the cost for the dedusting operation and to lower zinc emission to air. Also the zinc emission from waste water released from wet dedusting installation.

Chlorine has been shown to be an effective reagent to remove zinc as $ZnCl_2$. As result of the treatment applied on galvanized steel samples, zinc surface layers were removed and steel scraps remain unattacked. The zinc removal has been as high as 99% at preheating temperatures ~ 700ºC. Over this temperature, the quality of the steel scrap is negatively influenced. The higher temperature and the increasing of the O_2:Cl_2 ratios are favorable for developing the interaction between iron and oxygen. The formation of the scale is passed in the depth of the heated steel. Must be specified that one grade of galvanized steel were used in all experimental tests. For industrial conditions the chlorination process must be adapted to different steel qualities with variable compositional layers.

In the industrial steel making plants, the energy contained in the flue gas emitted from furnaces (BOF or EAF) can be valorized. By this way the energy consumption is reduced.

The conditions for dioxins forming must be taken in account. The selection of the steel scrap must be accurately carried. The advanced eliminating of other contaminants that are mixed with the metallic feedstock is necessary. At steel scrap preheating the presence of certain metals is favorable for the dioxins formation (by „novo synthesis process"). Copper, iron, zinc, aluminum, chromium, and manganese are known to catalyze PCDD/PCDF formation [18].

The formation of the chlorides involves an important risk associated to corrosion of the process equipment. For this reason these must be collected and decomposited for chlorine recovery.

References

[1]. A. Ender - *Recycling von oberflächenverdeltem Stahlschrott*, VDEh Kontakstudium Metallurgie, Teil IV: "Recycling", Freiberg, 26-28.05, (1997).

[2]. D. Janke, **L. Savov**, **H.-J. Weddige**, **E. Schulz** - *Scrap-based steel production and recycling of steel*, Mat. in Tehnol. 34(6)387, (2000), p.387-399.

[3].*** - *Prospect Material of Informations-Zentrum Weissbleche.* V., Kasernenstr. 36, 40213 Düsseldorf, Germany.

[4].*** - *Metallic-Coated Products and Specifications*, GalvInfoNote 2.4, Rev 1.1 Jan 2011.

[5]. *** - *Integrated Pollution Prevention and Control (IPPC), Best Available Techniques Reference Document on the Production of Iron and Steel*, March (2000), http://www.mst.dk..

[6]. K. Iimura, **H. Ito**, **M. Chino, T. Morishita, H. Hirata** - *Behaviour of contaminant heavy metals in soil-plant system.* Proc. Inst. Sem. SEFMIA, Tokyo, (1977), p.357.

[7]. P.F.J. Van der Most, **C. Veldt** - *Emission Factors Manual Parcom-Atmos: Emission factors for air pollutants,* (1992). TNO, NL (Ed.).

[8]. *** - *BAT Guidance Note On Best Available Techniques for the Initial Melting and Production of Iron or Steel*, ENVIRONMENTAL PROTECTION AGENCY, December, (2009), http://www.epa.ie.

[9]. M. Larsson, **P. Johansson** - *Surface cleaning of steel scrap* (88020), The Steel Eco-Cycle Environmental Research Programme for the Swedish Steel Industry 2004 – 2012, http://www.stalkretsloppet.se/rapporter/pdf/scientific_report_20042008.pdf.

[10]. *** http://www.transportation.anl.gov/materials/dezinc_recycling.html

[11]. J. Wichterlová, **R. Škuta**, **M. Metzing**, **D. Matýsek**, **K. Wichterle** - *Simultaneous Thermal Decomposition of PVC and Zinc Ferrite*, 36th International Conference of SSCHE, May 25–29, 2009, Tatranske Matliare, Slovakia.

[12]. J.K.S Tee, **D. J. Fray** - *Recycling of Galvanised Steel Scrap Using Chlorination*, EDP Congress, (1999), The minerals, Metals Materials Society, pp.883-891, (1999).

[13]. J.K.S Tee, **D. J. Fray** - *Removing Impurities from Steel Scrap Using Air and Chlorine Mixtures*, JOM, August, (1999), pp 24-27.

[14]. J.K.S Tee, **D. J. Fray** - *Recycling of Galvanised Steel Scrap Using Chlorination*, Ironmaking and Steelmaking, Vol. 32, (2005), No. 6, pp.509-514.

[15]. *** - *Steel Eco-Cycle, Closing the Loop in the Manufacture and Use of Steel in the Society*, Scientific Report, Phase 1, 2004-2008, www.steelecocycle.com.

[16]. G. Dapper, **W. Sloterdijk and C. A. Verbraak** - *Removal of surface layers from plated materials: upgrading of scrap*, Comervcrtion & Recycling, Vol. 2, No. 2. (1978), pp. 117 – 121.

[17]. J.K.S. Tee, **D.J. Fray** - *Recycling of Galvanised Steel Scrap - A Feasibility Study*, Paper presented at the R´99 Congress (Recovery, Recycling, Reintegration), February, (1999).

[18]. *** - *Standardized Toolkit for Identification and Quantification of Dioxin and Furan Releases*, Edition 2.1, December 2005, Prepared by UNEP Chemicals Geneva, Switzerland.

THE ANNALS OF “DUNAREA DE JOS” UNIVERSITY OF GALATI.
FASCICLE IX. METALLURGY AND MATERIALS SCIENCE
N^0. 1 – 2012, ISSN 1453 – 083X

COPPER PLATING CORROSION STUDY IN CERTAIN ENVIRONMENTS

A.M. CANTARAGIU[1], **M.D. GAVRIL (DONOSE)**[1], **D.C. VLADU (RADU)**[1], **C. GHEORGHIES**[2], **N. TIGAU**[2], **C.M. CANTARAGIU**[3]
[1]PhD students, [2]Faculty of Sciences and Environment, Chemistry, Physics and Environment Department
[3]Student, Faculty of Metallurgy, Materials Science and Environment
„Dunarea de Jos” University of Galati
email: cantaragiu_alina@yahoo.com

ABSTRACT

Copper plating was performed on nickel substrate by means of the potentiostatic electrodeposition method from a sulphate electrolyte solution. The copper coatings morphology was studied by means of the optical and electronic scanning microscopy techniques. The uniform electrodeposited films have a thickness of about 15 μm measured in cross-section. The corrosion behaviours of nickel substrate and copper films in different corrosive environments were studied. The corrosion study was performed by means of the linear polarisation method in four acid environments: 0.5 M H_2SO_4, HCl, HNO_3 and glacial CH_3COOH. From the recorded Tafel curves it was possible to obtain some information about the corrosion rate and the polarization resistance. In order to confirm these results, the gravimetric parameter was calculated by means of the “mass loss” method. By means of the X-ray diffraction analysis, the crystallographic structure of the specimens before and after corrosion was revealed. By means of the spectrophotometer device, the optical properties of the specimens were analysed.

KEYWORDS: electrodeposition, copper plating, corrosion, nickel substrate

1. Introduction

In recent years, copper has replaced aluminum as a metal for interconnects in electronic industry. Copper thin films are also used in the multilayer sandwiches of GMR hard disk read heads.

Among various methods of copper thin film deposition onto substrates, such as PVD, CVD, and sputtering, the electrochemical methods (electrolytic) have proven to be the least expensive, highly productive and readily adoptable [1].

Copper electrodeposition mechanisms have been studied in two chemical systems: the acidic without complexation [1] and the basic one, requiring the presence of buffering [2-4] and complexing reagents.

For obtaining the copper from the negative electrode some processes can be related, such as: precipitation, extraction, or electrodeposition [5,6]. One of these is the electrochemical process where electrodeposition baths are made, with or without the addition of complexing additives to increase efficiency.

An important characteristic of these electrodeposits is the morphology, where the electrodeposit growth can be related to the nucleation process (in two or three dimensions).

Searson et al. [7] studied the morphology and kinetics for copper nucleation during the electrodeposition in strongly acid media (pH~1.0) without additives. They observed that copper electrodeposition occurs at potentials over -0.04V and consists of the direct reduction of Cu^{2+} ions to metallic copper. They also observed that the current increases at slower rates related to the decrease in the quantity of ions from the bulk to the interface, showing a diffusion reaction-controlled process. For more negative potentials, the growth of nuclei was controlled by diffusion.

Zangari et al. [8] observed that, at pH of 2.5, the copper morphology shows a dendritic form and then forms clusters in the electrodeposit.

Pesic and Grujicic [4] correlated the nucleation process of copper electrodeposition and morphology and observed that at pH values over 3 the nucleation process was progressive (threedimensional growth) and, below this value, the model tended to an instantaneous nucleation, related to a bi-dimensional growth.

Pasquale et al. [9] studied the morphology of copper electrodeposits. They observed that the bath composition (preferably pH values) has a significant influence on the copper morphology, with well-formed grains and nuclei being formed in acid media.

Otherwise, at higher pH values, *Gabrielli et al.* [10] observed that copper electrodeposition formed small dendrites related to a copper metallic layer and another oxide layer, normally Cu_2O.

Nikolitic et al. [11] observed that the hydrogen co-deposition with metallic copper was related to a three-dimensional growth due to the porous morphology [12].

The aim of this investigation was to obtain copper films onto nickel substrate by means of the potentiostatic electrochemical deposition method. Also, the corrosion behaviour of these deposits in acid environments (0.5M H_2SO_4, HCl, HNO_3 and glacial CH_3COOH) was studied. Nickel surface was copper coated to evaluate the properties of the un-coated and coated surface during the corrosion process. These properties refer to the microstructural feature analysed by the optical and scanning electron microscopy (SEM), energy dispersive X-ray (EDX), as well as by X-ray diffraction (XRD) techniques where the corrosion resistance enhanced. The increased corrosion resistance results in improved protective coating performance that can be used as a hard surface on softer substrates.

2. Materials and methods

2.1. Materials

The copper chemical powder was purchased from commercial sources and has the highest purity available. The copper films have been electrodeposited onto nickel substrate from sulphate electrolyte solution having the composition presented in Table 1 [4,14].

***Table 1**. Copper plating bath composition and working conditions (no magnetic stirring)*

$CuSO_4 \times 5H_2O$	0.8 M
H_2SO_4	0.55 M
HCl	3.26×10^{-3} M
pH	1.7
T	50°C
Acid environments	0.5 M H_2SO_4, HCl, HNO_3, CH_3COOH

Before the electrochemical study, the samples were mechanically polished with fine grit SiC paper. Afterwards, the polished substrates were carefully chemically degreased with acetone and alcohol, etched with 1:10 HNO_3:H_2O, rinsed with distilled water and then, dried in air before their immersion in the electrolyte.

2.2. Methods and instruments

A standard three electrode system (electrochemical cell from Pyrex glass) with a cell (Fig. 1) volume of 100 mL was used to perform the electrochemical investigations at 50°C temperature. Temperature was controlled with a thermostat (model VEB MLW Prufgerate-Werk Medingen/Sitz Freital). An Ag/AgCl saturated electrode (SCE) served as the reference electrode (RE), and the counter electrode (CE) was a platinum sheet. A plate-shaped working electrode, WE, was made of nickel. The WE electroactive area was 2.5 cm^2. The electrolyte pH was recorded by means of Consort C931 equipment. Also, before and after deposition, the samples weight was measured using an electronic balance (model ESJ200-4).

The coatings preparation and corrosion behaviour were carried out potentiostatically with a potentiostat/galvanostat VoltaLab10 interfaced with VoltaMaster4 software for data acquisition and analysis [15].

***Fig. 1**. The experimental setup*

Potentiodynamic polarisation curves of the deposited films were measured from - 500mV toward the anodic direction of 500mV, with a scan rate of 50mV/s. The corrosion behaviour of deposited films has been observed by introducing them in different corrosive environments: 0.5M H_2SO_4, HCl, HNO_3 and glacial CH_3COOH. The same electrodes presented above were used in this case. The exposure corrosion time was one hour. The linear polarisation (Tafel curves) was used as method to study the corrosion behaviour. The corrosion rate is automatically calculated by specialized computer software using the Randles-Sevcik equation (1). Before and after each experiment the samples weight was measured by means of analytical balance. The mass losses (Δm_{corr}) and penetration index (p) values are shown in Table 2.

2.3. Morphology and structural characterization of metallic samples

The surface morphological features of the metallic specimens were examined by means of SEM measurements. Also, the chemical composition was achieved by means of EDX measurements. The micrographs and chemical compositions were registered using Quanta 200 Philips FEI Company device.

The crystallographic characteristics of the samples were analysed through the XRD using DRON-3M diffractometer. The XRD spectra were recorded at room temperature, X-ray diffractometer using the CoK$_\alpha$ radiation (λ = 1.79Å) in 2θ configuration ranged between 30 and 70º, at 40 kV tension and 30 mA current intensity with a scanning speed of 0.02º min^{-1} and acquisition time of 1 s/step.

By means of the interaction between a polychromatic beam and a copper film coated its behaviour was examined by reflectance measurements recorded by means of Perkin Elmer (type Lambda) 35 UV-VIS Spectrophotometer with double beam in the spectral range of 190÷1100nm.

3. Results and discussion

The appearance of nickel and copper coatings is analysed by means of the optical microscope at 500× magnification (Fig. 2). Obviously, a colour difference between two optical images of nickel substrate and copper coating can be seen. The polishing traces from nickel substrate with a grey colour (Fig. 2a) are compared to the reddish colour and spots from copper the deposit (Fig. 2b).

The copper crystalline grains can be observed.

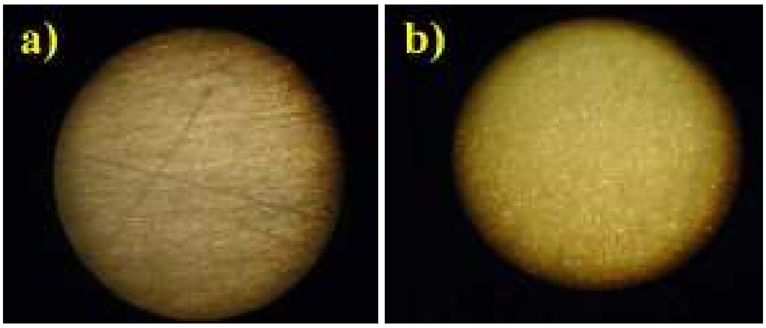

***Fig. 2**. The optical microstructure of a) nickel substrate and b) copper film before the corrosion test (500×)*

The above images are confirmed by the SEM micrographs (Fig. 3). Fig. 3a corresponds to the nickel substrate with the polishing direction traces, after the pre-treatment procedure. The chemical composition (Ni – 87wt %) of the substrate is confirmed by EDX analysis (Fig. 3d). The copper film shows the tetrahedral crystalline grains (Fig. 3b). The grain size is relatively faint and shows an excellent uniformity [16]. The EDX spectrum (Fig. 3e) shows the chemical composition of copper film deposited (Cu – 80wt %). Also, the thickness film was measured in cross section and it is around 25µm (Fig. 3c).

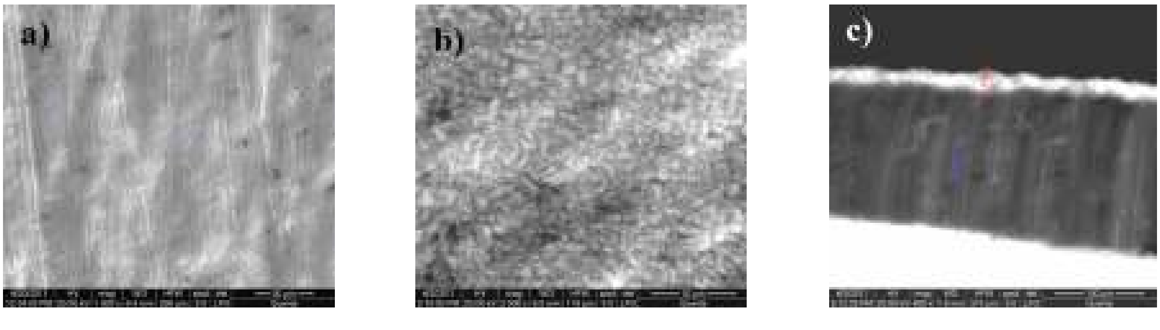

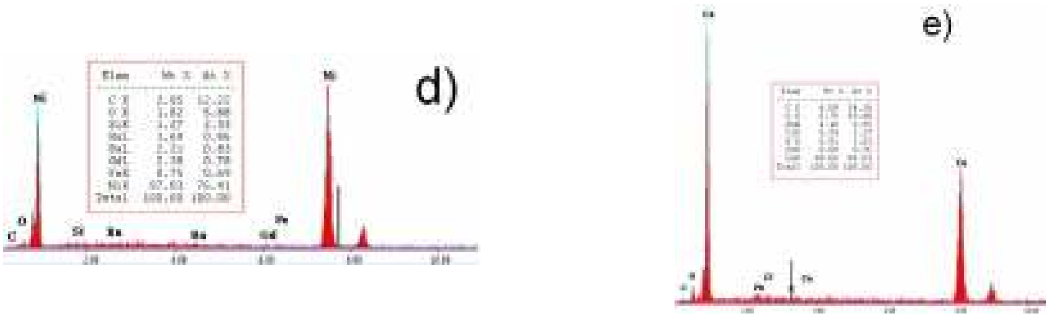

***Fig. 3**. Surface morphology of: a) nickel substrate; b) copper film; c) cross-sectioned copper coating obtained from a sulphate electrolyte (from top-down) at 50°C; d) EDX spectrum of nickel substrate and e) copper film*

The corrosion rates (Table 2) were achieved by means of the "mass loss method" [17,18], in static regime at room temperature and calculated based on equation (1):

$$V_{corr} = \frac{\Delta m}{S \cdot t} \qquad (1)$$

where: V_{corr} = gravimetric index [g/m^{2}s]; Δm = weight loss (before and after the corrosion test) by corrosion [g]; S = corroded surface area [m^2]; t = corrosion time [s].

The average depth of the composite corrosive destruction is calculated using the formula (2):

$$p = \frac{V_{corr}}{\rho} \cdot 8.76 \qquad (2)$$

where: p = penetration index [mm/y]; V_{corr} = gravimetric index [g/m^{2}s]; ρ = composite film density [g/cm^3].

The results are presented in Table 2.

***Table 2**. Corrosion behaviour of copper coatings onto nickel substrates immersed in acid solutions*

Sample	$\overline{d}$	Δm$_{corr}$	V$_{corr}$	p	Resistance group	Estimate note
	[µm)	[g]	[g/cm^{2}h]	[mm/y]		
1. with film	25	0.0516	-	-	-	-
2. with film in H_2SO_4		-0.0024	**0.096**	0.094	Very stable	2-3
3. with film in HCl		-0.0007	0.016	0.016	Very stable	2
4. with film in HNO_3		-0.002	0.047	0.046	Very stable	2
5. with film in CH_3COOH		0	0	0	Perfect stable	1

The copper growth is also affected by immersion in 0.5 M H_2SO_4 environment (Fig. 4a) which change the surface morphology and texture. Regarding the values in Table 2, this environment is the most aggressive environment having the highest corrosion rate. Also, the higher weight difference shows that a great number of copper ions were reduced from the surface during the electrochemical corrosion. The surface is coated with a uniform oxide layer on the copper film. The copper surface has a lower instability in contact with H_2SO_4 environment and the corrosion process is continuous. Also, this fact is confirmed by the EDX analysis (Fig. 4b). The sample insertion into a chloride solution (Fig. 4c) affects both the structure and morphology: the epitaxial growth on the nickel seed is favoured giving [111] and [200] textured layers; the grain size is slightly reduced and more uniform, with increased tendency to faceting and formation of triangular based pyramids, related to [111] texture, also with truncated apex, indicative of weak interfacial inhibition. The chloride oxide compounds on the surface were observed (Fig. 4d).

A few corrosion microelements on the copper film were observed when the sample was electrochemical by tested into the HNO_3 environment (Fig. 4e) [19]. The surface is instable inside the HNO_3 atmosphere. Due to the iron ions (Fig. 4f) content from the substrate, the aggressive action of this environment could be explained.

The copper deposition immersed into the glacial CH_3COOH environment presented a high surface stability having zero value for Δm, V_{corr} and p parameters (Table 2) and being perfectly stable as a resistance group.

The XRD technique has been used to identify the structure of copper thin films onto nickel substrates in two corrosion environments (0.5M H_2SO_4 and CH_3COOH) (Fig. 5).

The electrodeposition from sulphate bath on nickel substrate (with (111) and (200) specific crystallographic planes) gives copper layers two crystallographic orientations. The copper thin films are crystalline. The growth features are not well defined, apart from scattered square base pyramidal grains (Fig. 4c).

Compared to the database from the Reference Pattern the free energy of the surface-support-solution system allows the preferential growth of copper crystallites after the [111] and [200] crystallographic direction was observed.

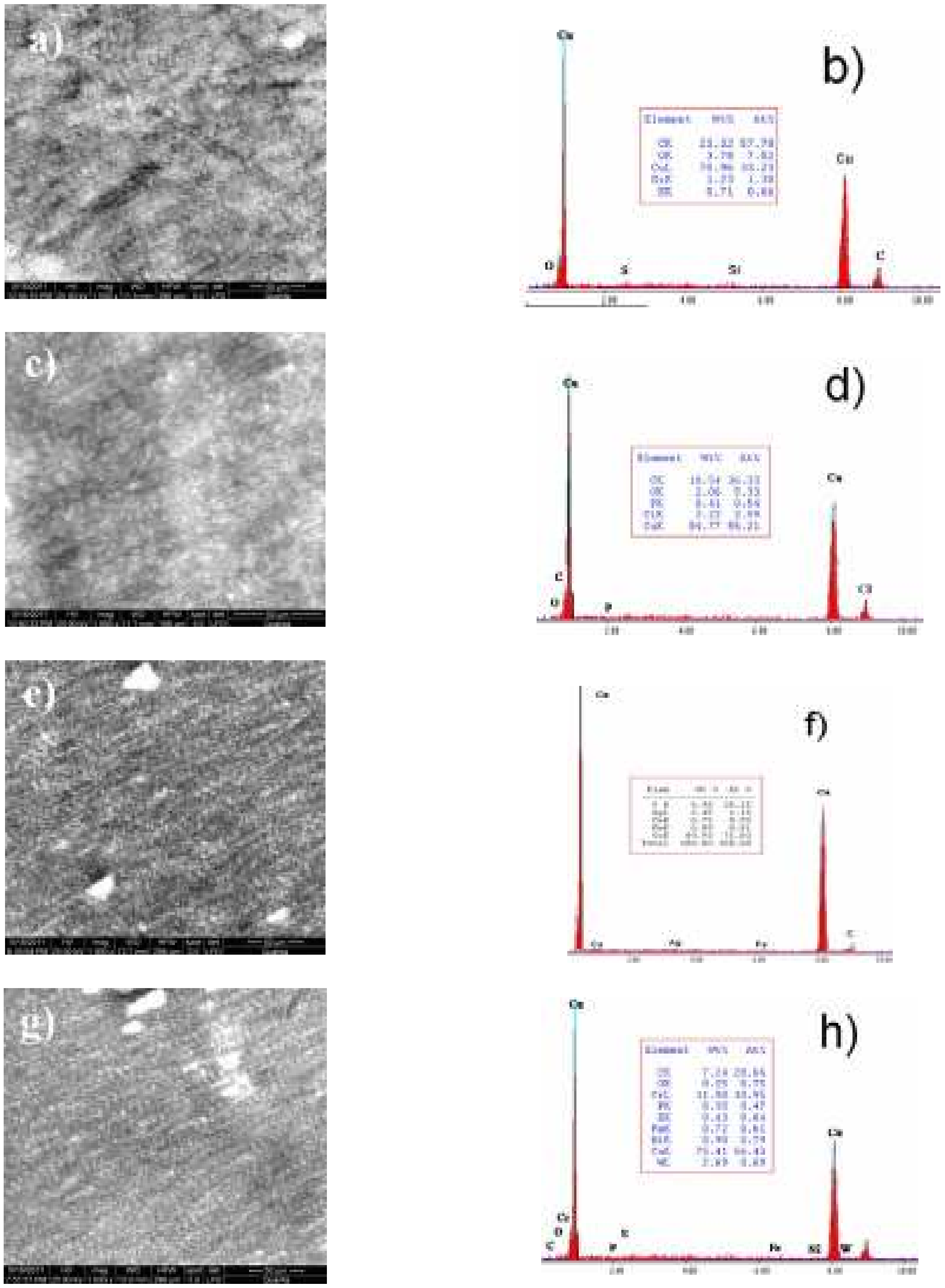

Fig. 4. *SEM images and EDX spectra of copper coating corroded surfaces in: a-b)* H_2SO_4*; c-d) HCl; e-f)* HNO_3 *and g-h)* CH_3COOH

The XRD analysis shows the peaks corresponding to [111] and [200] characteristic directions of an *fcc* structure for electrodeposited copper, according to the Joint Committee on Powder Diffraction Standards (JCPDS) [18]. Direction [002] is related to the Cu_2O structure [19].

The corrosion exposure to acid environment highlights the diffraction lines of oxide compounds (CuO, Cu_2O) formed during the experiment (Fig. 5). Therefore, the crystalline network is rearranged; the internal stresses are reduced by testing the sample in acid conditions [17]. Also, the intensity peaks of copper decrease during the testing. The oxides operated like a protective layer against the aggressive environmental factor. This fact is confirmed by microscopical analyses.

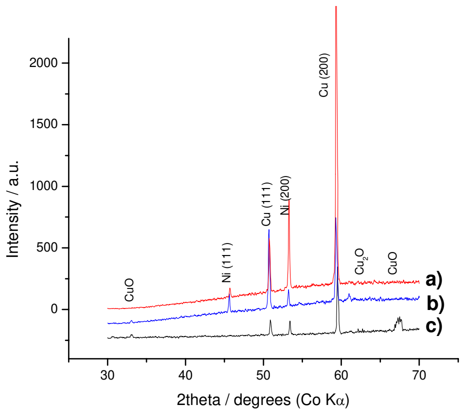

Fig. 5. *XRD patterns of a) copper coating and copper coating subjected to b) H_2SO_4 and c) CH_3COOH environments*

Fig. 5 shows a higher background radiation for the corroded copper versus the copper. A presence of numerous point defects can be seen onto the corroded surfaces in comparison with the copper sample. The crystallographic defects can be the vacancies, interstitials or replaced atoms of the crystal lattice. In other words, the copper samples are crystalline materials but they are not perfect, the regular pattern of atomic arrangement is interrupted by crystallographic defects [18].

Fig. 6 is shown the polarization curves in the case of copper films immersed in all acid solution studied in this paper.

For CH_3COOH environment the i_{corr} has the lower value while the R_p is high and the solution seems to have an inert activity. More corrosion resistance could be the CH_3COOH solution. Then, increasing the corrosive activity of acid environment (H_2SO_4), i_{corr} and V_{corr} increase and the R_p is drastically decreased. This fact can be due to the impurities inclusion which exists into a metallic matrix.

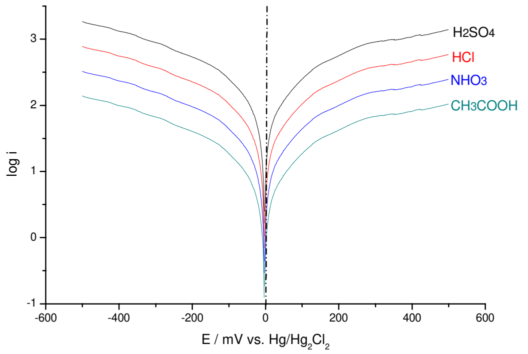

Fig. 6. *Polarisation curves (50 mV/s) of copper deposition at 25°C in various acid environments*

The HCl environment less corroded the surface and this fact means that the copper surface is quickly passivated. Thereby, these material surfaces could be classified in a very and perfectly stable resistance group due to the linear shape of the cathodic and anodic branches.

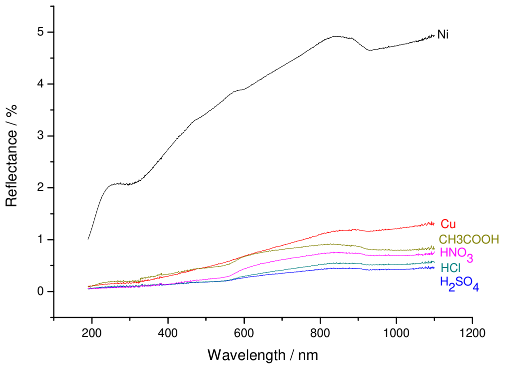

Fig. 7*. UV-VIS-IR spectra of nickel substrate, copper film and copper subjected to acid environments*

The curve in Fig. 7 corresponding to nickel indicates the formation of an inverse peak more evidently than those in the case of copper. This fact means that a minimum value of reflectance (R ≈ 2; 4.5%) appears at a maximum value of absorbance [20].

Increasing the wavelength increases the nickel surface capacity to reflect the light. The energy which is not adsorbed is reflected, being measured by means of the spectrometer. The amount of energy adsorbed can be easily determined by inspecting dips in the reflectance spectrum. Thereby, the nickel surface (linear shape of spectrum) is highly reflective in VIS region. For a thin and uniform copper layer appearance a linear shape curve was achieved having a good capacity to reflect the light. All copper deposition tested in the acid solution are good adsorber materials in VIS region due to the microelements presence on the surface.

4. Conclusions

✓ The corrosion behaviour of copper deposits immersed in acid environments was investigated using the linear polarization method.

✓ The electrochemical parameters were calculated by means of the gravimetric method and linear polarisation method.

✓ The free energy of the surface-support-solution system allows the preferential growth of copper crystallites after the [111] and [200] crystallographic direction was observed. Thereby, the copper thin films are crystalline.

✓ The corroded films are uniform and compact and have a crystalline structure. The oxides operated like a protective layer against the aggressive environmental factor. This fact is confirmed by microscopical analyses.

✓ These material surfaces could be classified in very and perfect stable like as resistance group due to the linear shape of the cathodic and anodic branches. The H_2SO_4 environment has the highest corrosion rate value. The HCl environment less corroded the surface and this fact means that the copper surface is passivated quickly. More corrosion resistant could be the CH_3COOH solution.

✓ Thin and uniform copper layer appearance has a good capacity to reflect the light. The copper deposits tested in the acid solutions are opaque materials in VIS region due to the microelements from the surface.

References

[1]. M. Schlesinger, M. Paunovic - *Modern Electroplating*, fourth ed., Wiley, New York, NY, (2000).

[2]. A. Radisic, J.G. Long, P.M. Hoffmann, P.C. Searson - J. Electrochem. Soc. 148 (1), (2001), C41.

[3]. G. Oskam, P.M. Vereecken, P.C. Searson - J. Electrochem. Soc. 146 (4), (1999), 1436.

[4]. D. Grujicic, B. Pesic - *Electrodeposition of copper: the nucleation mechanisms*, Electrochim. Acta 47, (2002), 2901-2912.

[5]. Aurbach D, Markovisky B et al - J. Power Sources 491:499, (2007).

[6]. Xu J, Thomas HR et al - J. Power Sources 512-527 (2008).

[7]. Searson PC, Ross FM et al - Surf. Sci. 1817-1826 (2006).

[8]. Zangari G, Arrington D et al - Electrochim. Acta 2644-2649 (2008).

[9]. Pasquale MA, Gassa LM et al - Electrochim. Acta 5891-5904 (2008).

[10]. Gabrielli C, Devos O et al - J. Electroanal. Chem. 95-102 (2007).

[11]. Nikolitic ND, Brankovic G et al - J. Electroanal. Chem. 13-21 (2008).

[12]. V. G. Celante, Ć M. K. Pietre, Ć M. B. J. G. Freitas - *Electrochemical and structural characterization of copper recycled from anodes of spent Li-ion batteries*, J. Appl. Electrochem. (2010) 40:23–28 DOI 10.1007/s10800-009-9959-2.

[13]. D. Grujicic, B. Pesic - *Electrodeposition of copper: the nucleation mechanisms*, Department of Materials, Mining and Metallurgical Engineering and Geology, University of Idaho, McClure Hall, Moscow, ID 83844-3024, USA.

[14]. A. Vicenzo, P.L. Cavallotti - Copper electrodeposition from a pH 3 sulfate electrolyte, J. Appl. Electrochem. 32: 743–753, (2002).

[15]. A.M. Cantaragiu - *Studii si cercetari privind obtinerea si caracterizarea unor acoperiri nanostructurate biocompatibile*, PhD Thesis, (2011).

[16]. D. Popovici, E. Trimbitasu, O. Pantea, D. Bombos, L. Antonescu - *Determinarea eficientei inhibitorului de coroziune Aticamina OTM 2 (The efficiency study of OTM2 Aticamina corrosion inhibitor)*, Buletinul Universității Petrol-Gaze din Ploieşti (Bulletin of the Petroleum-Gas University of Ploiesti), LIV, 4, 189-196, (2002).

[17]. P. Hagioglu, C. Gheorghies, A.M. Cantaragiu, S. Moisa - *The Accelerated Corrosion Behaviour in Saline Environments of Some Samples Made of Tombac, Copper and Aluminium*, J. Sci. Arts, Year 20, 1(12), pp. 153-160, (2010), ISSN: 1844-9581, eISSN: 2068-3049.

[18]. *** Joint Committee on Powder Diffraction Standards (1991) Diffraction Data File, No.45-0594, JCPDS international center for diffraction data, Pennsylvania.

[19]. *** Joint Committee on Powder Diffraction Standards (1991) Diffraction Data File, No.5-661, JCPDS international center for diffraction data, Pennsylvania.

[20]. P. Hagioglu, C. Gheorghies, A.M. Cantaragiu, R. Boiciuc, N. Tigau - *Corrosion Behaviour of Tombac Used in Cult Objects Manufacturing*, The Annals of “Dunarea de Jos” University of Galati, Fascicle IX, Metallurgy and Materials Sciences, 2, (2009), ISSN 1453-083X.

THE ANNALS OF “DUNAREA DE JOS” UNIVERSITY OF GALATI.
FASCICLE IX. METALLURGY AND MATERIALS SCIENCE
N^0. 1 – 2012, ISSN 1453 – 083X

A TEST FOR RAPID TRIBOLOGICAL CHARACTERIZATION OF BEARING STEELS

Constantin GHEORGHIES, Mihaela BUCIUMEANU,
Dan SCARPETE, Livia GHEORGHIES, Dorian BOLD
„Dunarea de Jos” University of Galati
email: constantin.gheorghies@ugal.ro

ABSTRACT

In this paper is a study the influence of the material and heat treatment on the changes of the fine structure parameters of the superficial layer of triboelements during the first cycles of rolling contact process. The tests were conducted by using a four-roller testing machine. The specimens (rollers) were made of case-hardening, through hardening and high frequency hardening steels. In order to induce different stress distributions in the superficial layer of the specimen specific treatments were applied. Using X-ray diffractometry can be appreciated that the durability of rolling tribosystems can be determined by an optimal relationship between studied parameters. The observed correlation can be used as a fast method to estimate the fatigue life of rolling bearing materials.

KEYWORDS: fine structure, steel, X-ray diffractometry, contact fatigue

1. Introduction

Generally, in the rolling tribosystems the durability is conditioned by the stress state and structure of the superficial layer. According to [1] for certain values of the Hertzian stress (σ_0>3.5GPa) the most important changes in the behaviour of the material occur during the first testing cycles (N<10). Residual stresses appear during this period. These stresses are added to the stresses due to the previous technological process. Such cases occur during thermal or thermochemical treatments performed in order to obtain a hard superficial layer.

The distribution of the thermal and structural stresses in the superficial layer of the material is presented in the figure 1 (S-surface, C-core) [2].

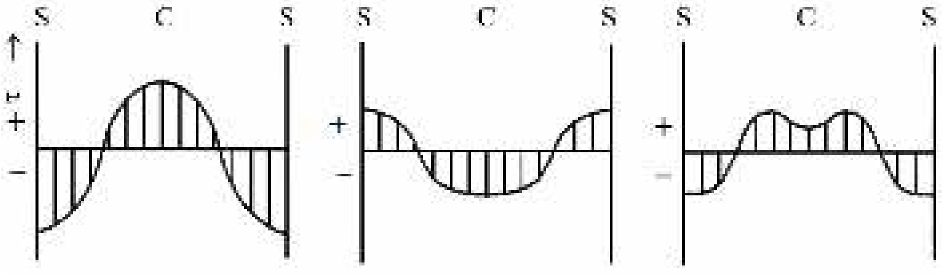

a b c

Fig. 1. *Distribution of the stresses in the superficial layer: a-thermal stress; b-structural stress; c-resultant stress.*

It is worth to mentioning that the total stress in the superficial layer can be either compressive (-) or tensile (+). It depends on the relation between those two types of stresses.

In this paper we propose a fast tribologial characterisation of some steels when they are subjected to rolling contact fatigue processes.

2. Experimental procedure

2.1. Materials

The specimens (cylindrical rollers) used in this study were machined from three different materials that are used in rolling bearing manufacturing (21MoMnCr12XS steel, 41MoCr11 steel and RUL 1 steel). The loading rollers were manufactured from 21MoMnCr12XS steel. The materials and the treatments applied to induce different stress distribution in the superficial layer are presented in Table 1.

Table 2 shows the chemical composition of the materials used in this study.

***Table 1.** Materials and applied treatments*

Materials	**Treatment**	**Hardness,** HRC
21MoMnCr12XS	C+H+LT	62±3
41MoCr11	FH+LT	54±2
RUL 1	H+LT	62±2
21MoMnCr12XS	C+H+LT	62±2
C-carburizing; H-hardening; LT-low tempering; FH-high frequency hardening		

***Table 2.** Chemical composition of the materials*

Materials	**Elements, %**							
	C	**Mo**	**Mn**	**Cr**	**Si**	**Ni max**	**S max**	**P max**
21MoMnCr12XS	0.18-0.24	0.20-0.30	0.80-1.20	1.00-1.40	0.17-0.37	-	0.035	0.035
41MoCr11	0.38-0.45	0.15-0.30	0.40-0.80	0.90-1.30	0.17-0.37	-	0.025	0.025
RUL 1	0.95-1.10	max 0.08	0.25-0.45	1.35-1.65	0.17-0.37	0.30	0.002	0.027

2.2. Experimental test setup

In order to carry out the test a pitting testing machine having four pressing rollers has been used [3].

The contact Hertzian stress was 4 GPa. The tests were performed by loading from 0 to 12 cycles, in steps of 2 cycles. The schematic representation of the test machine is presented in Figure 2. The fine structural changes [4-6] in the superficial layer of the tested materials have been estimate during testing cycles.

These structural changes were obtained by X-ray diffraction method, using a DRON-3 equipment (u=40kV, I=20mA, λ=0.70926 Å) [4].

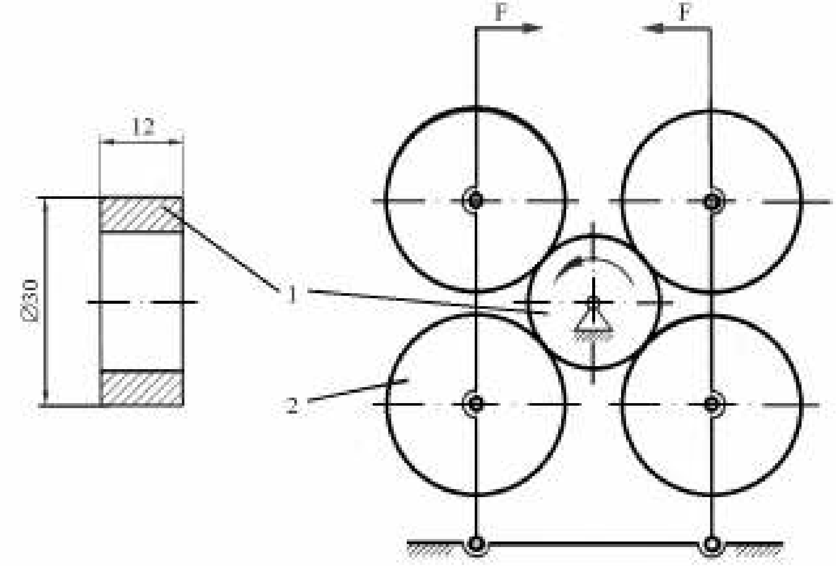

***Fig. 2.** Schematic representation of test setup:
1-specimen roller; 2-loading (pressing) roller*

3. Experimental results and discussion

3.1. Evolution of the fine structural changes

The fine structure of the ferrite phase in tested steel specimens was determined by the X-ray diffraction method. The distribution of $B_{(110)}$ size vs. number of cycles is presented in Figure 3. $B_{(110)}$ is inversely proportional to the dimension of the mosaic blocks within the ferrite phase.

The evolution of the mosaic blocks for the tested steel samples is the same.

The decreasing of the dimension of the mosaic blocks is due to the fragmentation of the crystalline lattice under loading. The RUL 1 steel specimens present smaller mosaic blocks. This shows that RUL 1 steel has superior strength.

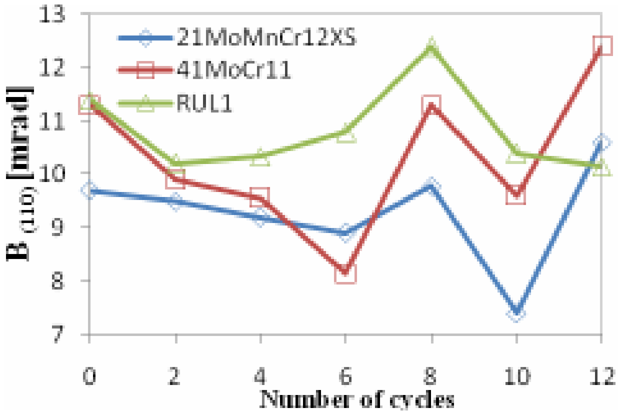

***Fig. 3.** Distribution of $B_{(110)}$ size vs. number of cycles*

The distribution of $B_{(220)}$ size vs. number of cycles is presented in Figure 4. $B_{(220)}$ is directly proportional to inner second order stresses.

The carburizing and through hardening steels have a similar behaviour from the point of view of the inner second order stresses and show higher stability. The high frequency hardening steel presents important changes when the number of testing cycles increases.

These changes can be explained taking in account the presence of a meta-stabile tension state induced by the initial thermal treatment.

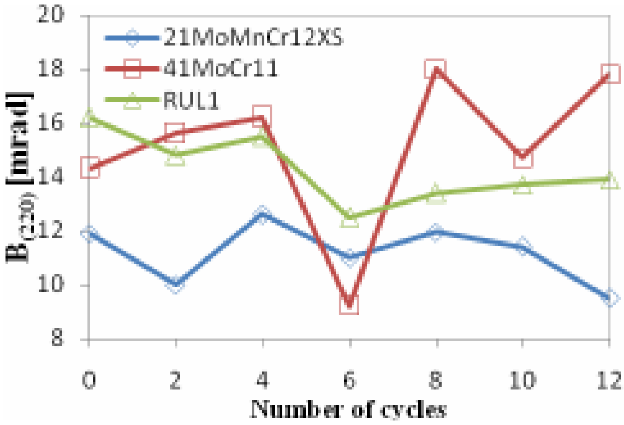

***Fig. 4.** Distribution of $B_{(220)}$ size vs. testing cycles*

The distribution of $(I_{bkg}/I_{max})_{220}$ ration vs. number of cycles is presented in Figure 5. This parameter is directly proportional with the dislocation density level. The evolution of the density level in the ferrite phase during the testing process is the same for all the tested steels. As the number of testing cycles increases the level of density dislocation shows a common value. This confirms that the superficial layer presents an energetically stabilised state.

The distribution of $2(\Delta\theta)_{220}$ vs. number of cycles is presented in Figure 6. This is directly proportional with the first order tension. For the RUL 1 steel there is an initial tensile state that varies relatively less than high frequency hardening and carburizing steels.

These different stress states in the superficial layer of tested steels have a favourable influence on their durability.

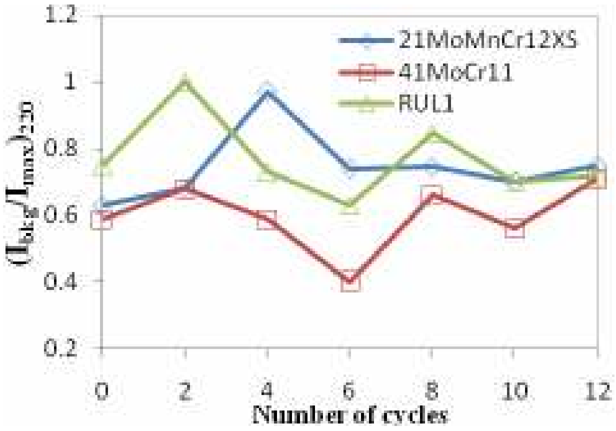

Fig. 5. *Distribution of* $(I_{bkg}/I_{max})_{220}$ *ratio vs. testing cycles*

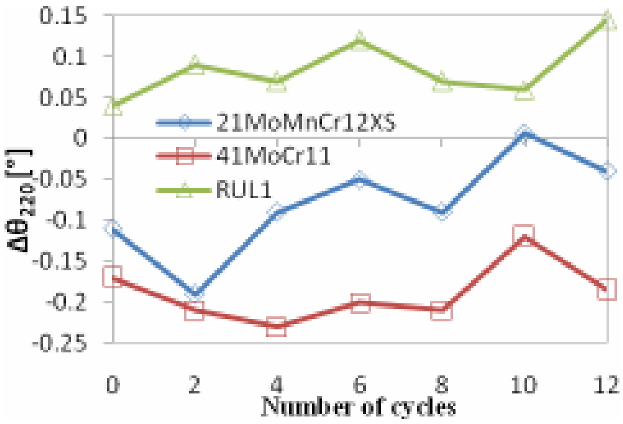

Fig. 6. *Distribution of* $2(\Delta\theta)_{220}$ *vs. testing cycles*

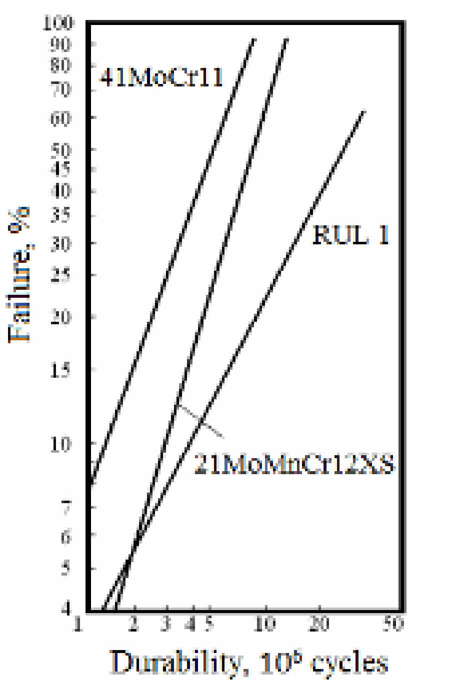

Material	**$L_{10,}$ 10^6 cycles**
21MoMnCr12XS	2.55
41MoCr11	1.24
RUL 1	3.47

Fig. 7*. Estimation of* L_{10} *durability for the tested materials*

3.2. Fatigue tests

Contact fatigue experimental tests were made using the four-roller testing machine (Figure 2). To detect and record the rolling contact microcracks without destroying the steel, a special type of non-symmetrical ring was used for the specimens [6].

For each material 10 specimens were tested. All tests were conduced at ambient temperature, in a laboratory environment, with a Hertzian pressure of 1520MPa and at specimen rolling speed of 4000rpm. The Hertzian pressure was calculated neglecting the end effect. The lubricant was mineral oil T80EP2 recirculated at the temperature of 52^{o}C.

The fatigue life for each observed specimen was recorded. Figure 7 shows the fatigue life data used to estimate L_{10} of Weibull distribution (Figure 7).

4. Conclusions

The main conclusion of this research can be drawn as follows:

-from the structural point of view the response of the tested steels is relative identically during the first loading cycles, but RUL 1 steel showed superior durability;

-the evolution of the inner second order tensions shows a superior behaviour for RUL 1 and carburised steels;

-the Hertzian rolling contact loading leads to the same level of dislocation density in the superficial layer for all tested steels. A superficial energetic equilibrium occurred and in corrosive environments the steels will have the same behaviour.

-the initial first order stress state does not change the sign during testing process.

-the structural and stress states changed in the superficial layer in the first 12 loading cycles.

These were concluded based on the X-ray diffraction method. It allows to state that the durability of the rolling tribosystem is conditioned by an optimal relationship between the parameters studied.

References

[1]. V. L. Popov - *Contact Mechanics and Friction, 1st Edition*, Springer, (2010).

[2]. L Pilloni, F Attura, A Calza-Bini, G De Santis, G Filacchioni, A Carosi, S Amato - *Physical metallurgy of BATMAN II Ti-bearing martensitic steels,* Journal of Nuclear Materials, 258–263 (1998) 1329–1335.

[3]. I. Crudu, et. al. - *Wear testing machine*. Patent of invention no. 83160/1982.

[4]. T. Shintani, Y. **Murata** - *Evaluation of the dislocation density and dislocation character in cold rolled Type 304 steel determined by profile analysis of X-ray diffraction*, Acta Materialia 59, 4314-4322, (2011).

[5]. N.E. Dowling - Mechanical Behavior of Materials: Engineering Methods for Deformation, Fracture, and Fatigue, 2nd edition, Pretince Hall, (1998).

[6]. Y. Ohue, K. Matsumoto - *Sliding–rolling contact fatigue and wear of maraging steel roller with ion-nitriding and fine particle shot-peening*, Wear 263 (2007) 782–789.

THE ANNALS OF "DUNAREA DE JOS" UNIVERSITY OF GALATI.
FASCICLE IX. METALLURGY AND MATERIALS SCIENCE
N^{0}. 1 – 2012, ISSN 1453 – 083X

MODERN APPROACHES IN DESIGN OPTIMIZATION OF PARTS AND THE DEVELOPMENT TREND OF SURFACE TREATMENTS

Elisabeta VASILESCU, Ana DONIGA
"Dunărea de Jos" University of Galaţi
email: elisabeta.vasilescu@yahoo.com

ABSTRACT

This paper summarizes the surface engineering technologies having a substantial contribution to increasing operational performance of the parts as well as current trends in the implementation of surface processing technologies that imply technical benefits and minimum negative impact on the environment The experimental results illustrate the influence of during superficial thermal treatment by high frequency current heating and thermochemical treatment (ionic nitriding) on the structural and physic - mechanical characteristics of heat treatable steel pieces. Also experimental results allowed conclusions on optimal regimes of surface processing and comparative analysis of properties obtained through different methods of processing.

KEYWORDS: surface, high frequency current heating, steel, mechanical characteristics, ionic nitriding

1. Introduction

For a more efficient recovery of materials and in order to achieve functional parameters and sustainability in service products, a judicious analysis of the functional conditions highlight most accurate quantification of the nature and intensity of demands is now an essential condition in the design of parts. The correlation of the surface functionality of the parts (provided by an appropriate choice of the method to ensure properties) with requests from its operation in a defined environment is a key factor in surface engineering [1]. Superficial heat treatments are procedures that can contribute to achieving success and improving surface properties, the base material (core or substrate) does not hold. These properties are obtained by structural or chemical structural modifications (thermo chemical treatments) in superficial layer of the work piece and/or by depositing a coating (Fig. 2).

***Fig. 1**. Steel parts whose surface properties can be improved by different methods [9.10]*

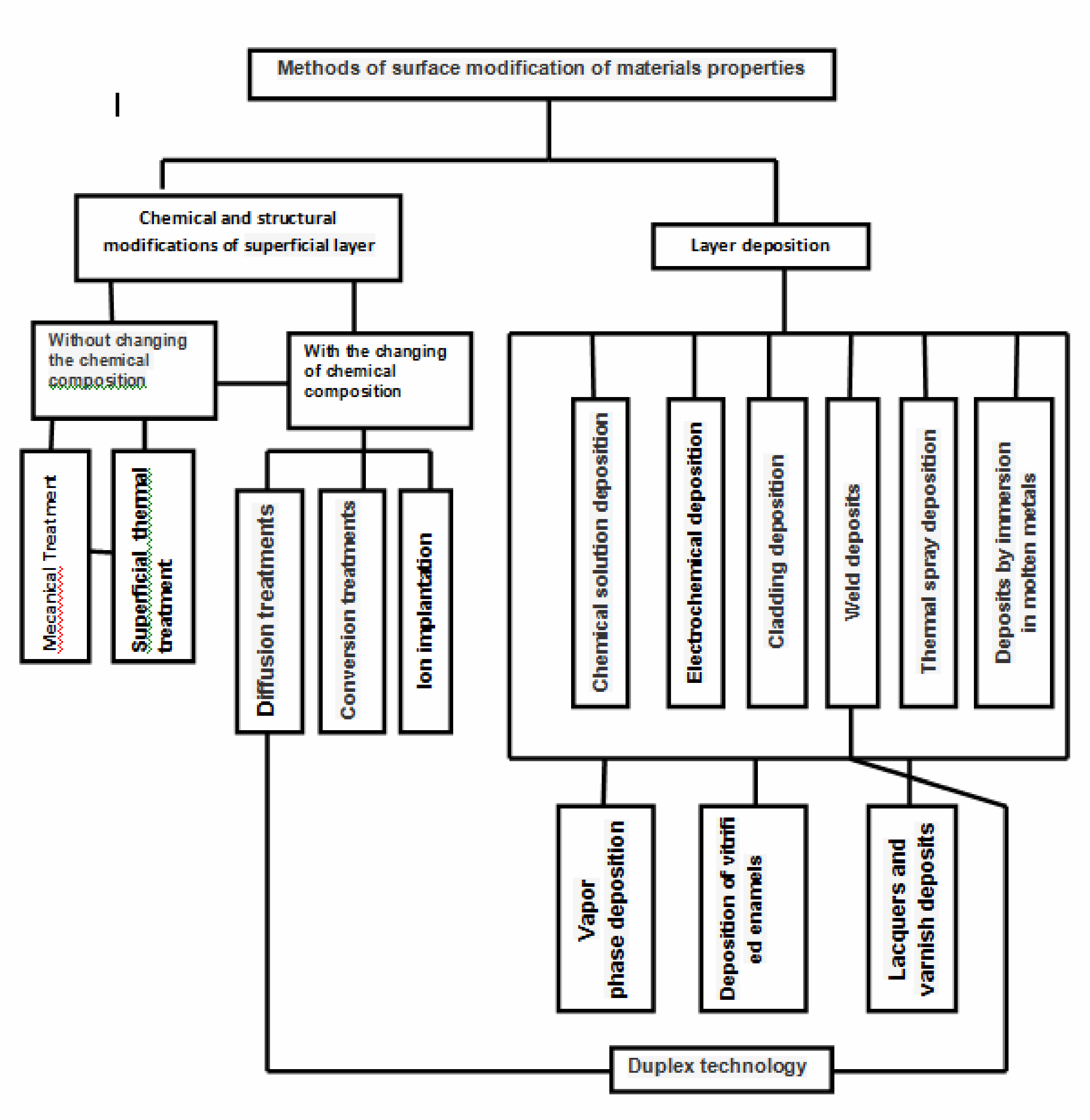

Fig 2. *Classification methods amending superficial properties of materials [1]*

Traditional treatments and therapies thermochemical surface hardening are still the main ways of improving surface properties of the parts, especially the resistance to wear and fatigue.

The development of thermochemical treatments, especially of those made in vacuum and plasma, lead to a more rigorous control of the depth and properties of the modified layer, increasing productivity and reducing adverse environmental effects.

2. Experimental conditions

Experimental investigations were performed on samples of steels to improve the quality of 41MoCr11 OLC45, to which different thermal or thermochemical treatments were applied in order to observe structural changes and properties.

The chemical composition of steel qualities is presented in Table 1. Further, in some samples were tested regimens surface tempering with heating currents of high frequency plasma nitrating regimes and specialized equipment.

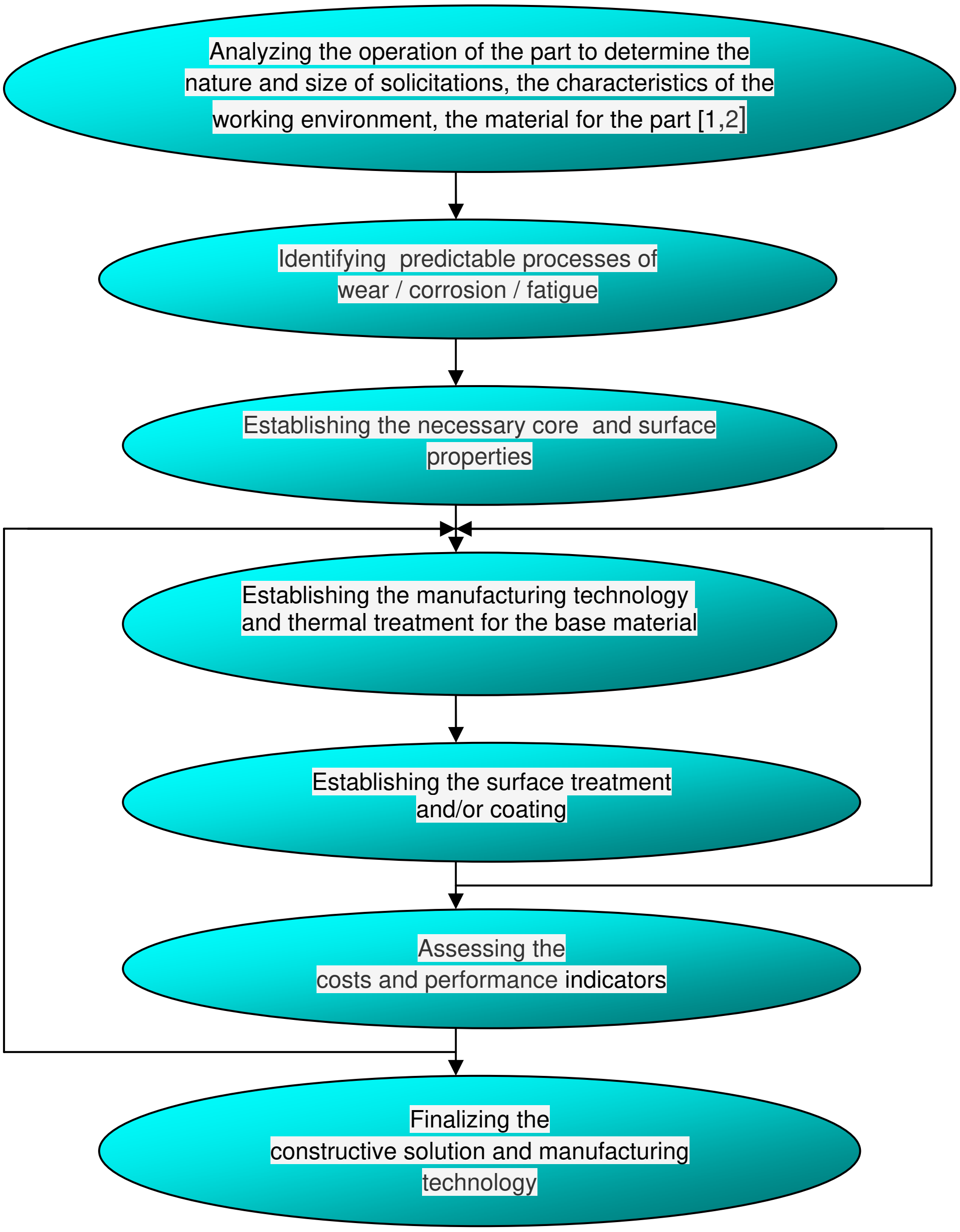

***Fig. 3**. Sequences of a the product design of a given part [9.10]*

2. Experimental conditions

Experimental investigations were performed on samples of steels to improve the quality of 41MoCr11 OLC45, to which different thermal or thermo chemical treatments were applied in order to observe structural changes and properties. The chemical composition of steel qualities is presented in Table 1.

***Table 1**. Chemical composition of samples*, %

Steel quality	**C**	**Mn**	**Si**	**S**	**P**	**Cr**	**Mo**
OLC45	0.42-0.50	0.50-0.80	0.17- 0.37	0.020-0.45	max. 0.04	-	-
41MoCr11	0.38-0.45	0.60-0.90	0.17- 0.37	max. 0.035	max. 0.035	0.90- 1.20	0.15- 0.30

There have been conducted experiments on determining the optimal process parameters to improve heat treatment (quenching and high tempering Fig. 4 followed by surface treatments. Further, in some samples were tested regimens surface tempering with heating currents of high frequency plasma nitrating regimes and the specialized equipment.

Table 2. *Experimental heat treatment regimes in volume (41MoCr11)*

Sample/ experimental regime	**Hardening temperature** [^{0}C]	**Cooling environment**	**Comeback Temperature** [^{0}C]	**Cooling environment**	**HB**
1	840	oil	200	air	381.2
2	840	oil	250	air	369
3	840	oil	300	air	341
4	840	oil	350	air	300.2
5	840	oil	400	air	288.6
6	840	oil	450	air	335.5
7	840	oil	500	air	269.6
8	840	oil	550	air	250.6
9	840	oil	600	air	253
10	840	oil	650	air	204.55
11	880	oil	200	air	358.8
12	880	oil	350	air	375.6
13	880	oil	500	air	299.6
14	880	oil	650	air	215.8
15	850	air	-	-	217

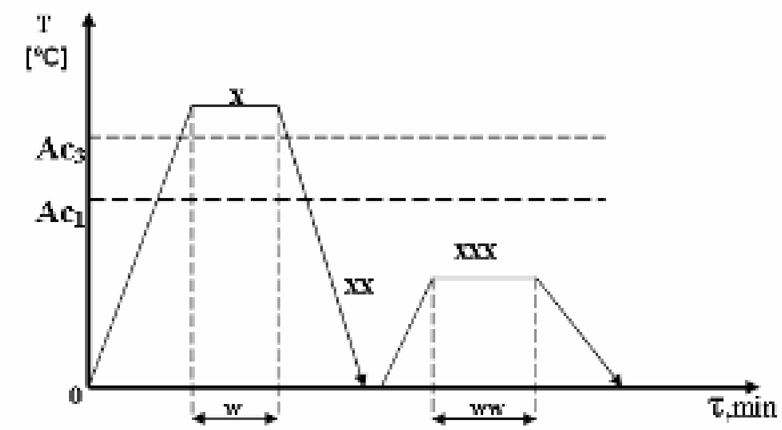

Fig. 4. *Experimental heat treatment regimes for determining optimal parameters of improvement. Annealing temperature X: XX-Cooling medium: XXX-temperature recovery: W term maintenance the annealing temperature (2min/mm) ww-temperature maintenance during recovery*

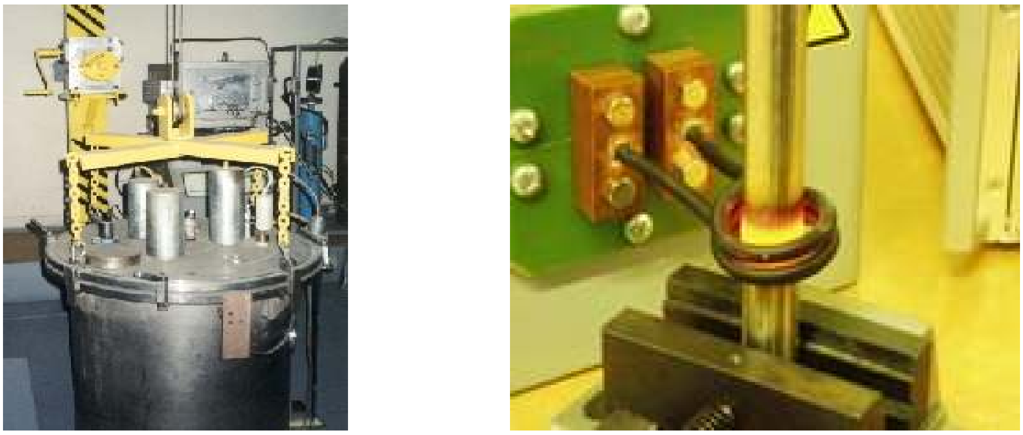

a b

Fig. 5. *Experimental equipment*
a). Ion nitriding facility, b). Installation for high frequency heating quenching CIF)

The thermochemical nitriding treatment was performed in gas dissociate demonian, by heating to 550°C and maintaining 1 the ion nitrating for 16 hours in a special facility (in Arcelor Mittal SA, Figure 5).

Further experiments aimed at establishing the correlation between the structural state of the core due to the heating treatment (by volume) and the method of surface treatment to achieve maximum efficiency in the design of the improved steel to parts.

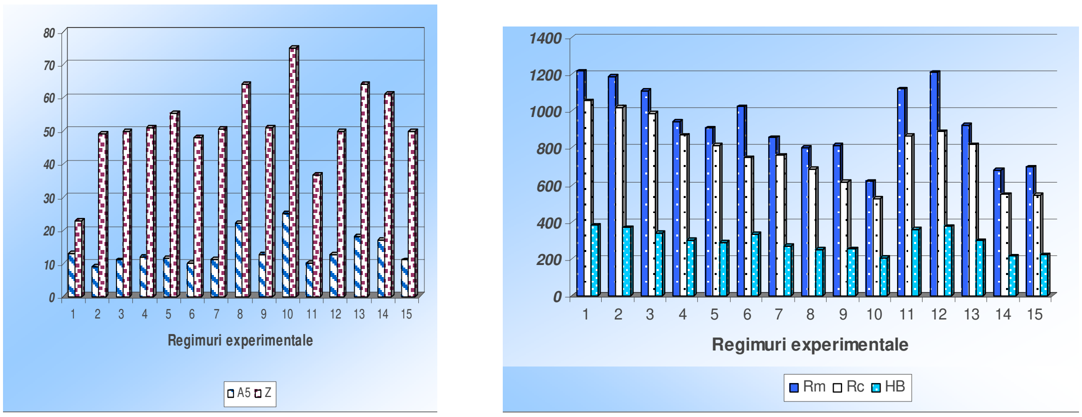

***Fig. 6**. Mechanical properties of 41MoCr11 steel samples*

Microstructural aspects. X100, 2% natal attack

Core

Nitrided layer

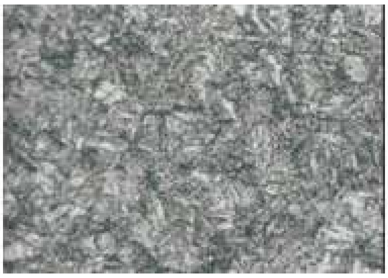

Center hardness: 329 HV

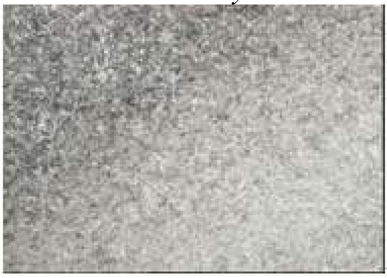

Middle layer hardness: 412 HV, 516 HV, 549 HV

Microstructure feature layer

Layer hardness: 713 HV, 739 HV, 745 HV

4. Conclusions

This paper presents the study of the new approach in designing optimal surface engineering technologies, but is also part of the research results on some superficial heat treatments applied to improve steel parts. Experimental results illustrate the influence of the main technological parameters specific surface heating with high frequency currents of nitride ion on the properties of the surface layer of steel parts of the improvement. Moreover, experimental results allowed conclusions on the optimum processing volume to obtain optimal characteristics in all the parts by applying light heat processing methods.

References

[1].*** - *Tratamente termice şi ingineria suprafeţei*, nr.1/2002, nr.1-2/2003

[2]. Levcovici M.S., Vasilescu E., Gheorghie, L. - *Ingineria suprafetelor* - E.D,P. Bucureşti, (2003).

[3]. Bhushan B, Gupta B. K - *Handbook of Tribology- Materials, Coating and Surface Treatments*- Krieger Publishing Company-Malabar, Florida, (1997).

[4]. Popescu N, Constantin Ghe, Popescu O. - *Tratamente termice neconvenţionale*, Ed. Tehnică, Bucureşti, (1990).

[**5**]**. Minkevici A.N. -** *Tratamente termochimice ale materialelor şi aliajelor*, Ed. Tehnică, (1968).

[6]. Gilfrich K V - *Characterization of Solid Surfaces*, New York, (1974).

INTEGRATED ANALYTICAL STUDY FOR THE SOMES METALIC ARTEFACT DISCOVERI IN IBIDA SITE, ROMANIA

Viorica VASILACHE[1,2], **Dan APARASCHIVEI**[2], **Ion SANDU**[1],
Violeta VASILACHE[3], **Ioan Gabriel SANDU**[4]
[1]„Al.I. Cuza” University Iasi, ARHEOINVEST Platform
[2]Institute of Archaeology Iasi
[3]„Stefan cel Mare” University of Suceava, Faculty of Food Engineering
[4]„Gh. Asachi” Technical University of Iasi, Department for Teacher Training
email: sandu_i03@yahoo.com

ABSTRACT

The paper presents the results of the analyses conducted using the SEM-EDX and micro-FTIR co-assisted techniques, on several metallic artefacts unearthed during the excavations at the (L)Ibida archaeological site in Slava Rusă, Tulcea County, Romania, that took place between 2001 and 2008. The data produced is of use in identifying several archaeometrical structural and compositional features which allow for the identification of the origin of the ores, of the alloy type, and of the manufacturing technology. A series of new data is thus produced, that can consolidate the three databases of scientific conservation of metallic artefacts (i-archaeometallurgy/archaeometry/historiography, ii-museum exhibiting, iii-itinerate/transfer/exchange/trade).

KEYWORDS: metal, SEM-EDX, micro-FTIR, archaeology

1. Introduction

The investigation of metallic artefacts requires a close collaboration between specialists from various domains of study: archaeology, history, chemistry, physics, metallurgy, geology, etc. They seek to establish: the nature of the material, the manner of processing the raw material, the manufacturing of the object itself, the subsequent preserving and restoring activities the object underwent.

To these purposes, they most often employ interdisciplinary methods of analysis, such as optical microscopy, scanning electron microscopy (SEM) alongside an EDX detector, micro-FTIR, calorimetry by reflexion, etc. [1].

The present study will provide the results of the SEM-EDX and micro-FTIR analyses performed on several objects discovered during the excavation conducted between 2001 and 2008 at the *(L)Ibida* archaeological site from Slava Rusă, Tulcea County, Romania.

As with any valuable cultural heritage asset, metallic artefacts can "travel", from the manufacturer who created them to the museum which exhibits them, by one of the following routes:

- Normal route of artworks, with a range of specific contexts (creation, acquisition, classification, display, preservation/ restoration, etc.);
- abandonment route, with contexts of creation, acquisition, use, loss of use functions, abandonment, archaeological discovery, preservation/restoration, ranking, showdown, etc.;
- concealment and oblivion route (especially for hoards), with contexts of creation, acquisition, use, loss of use functions, abandonment, archaeological discovery, preservation/restoration, display etc.;
- route through theft, with contexts of creation, acquisition, use, loss of use functions, abandonment, archaeological discovery, preservation/restoration, display or reuse etc.;
- route through falsification, reproduction/ copying, destruction, etc. with contexts of creation, acquisition, use, unlawful/illegal activities and their discovery, recovery of heritage functions, reintegration by display setup;
- route by disaster (earthquake, flood, fire, volcanic eruption, landslide, crash, etc.), with contexts of creation, acquisition, use, loss of use functions, abandonment, archaeological discovery, preservation/ restoration, display;

- Route by plagues (cholera, health disasters etc.), with contexts of creation, acquisition, use, loss of use functions, abandonment, archaeological discovery, preservation/restoration, display;

Some routes may modify a series of heritage elements (patina, share value, conservation status, etc.) as well as the main heritage function, the aesthetic and artistic.

An outline of areas of interest, the purpose of conservation and scientific activities integrated bronze artefacts in accordance with codes of ethics, is shown in Figure 1.

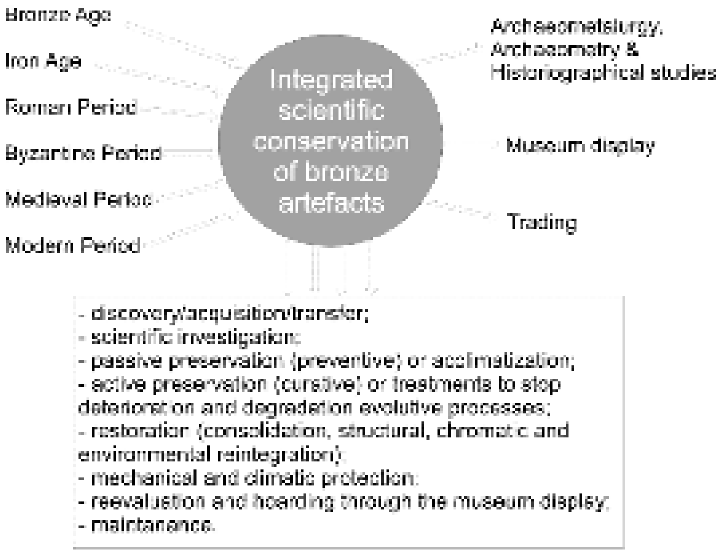

Fig. 1. *Scheme of the areas of interest (left), goals (right) and specific integrated scientific conservation activities (bottom) of ancient bronze artefacts*

For the value of a piece of bronze coming from archaeological sites there are some basic steps to be followed, namely [1, 2, 3]:

-excavation;

-cleaning;

-scientific investigation;

-the coherent reconstruction of the shape from fragments;

-completion of form and ornament;

-mechanical and climatic protection by coating;

-display and maintenance.

Depending on the circumstances and purposes, these steps may be detailed or developed with other activities or interventions.

2. Materials and methods

The artefacts selected for investigation have been discovered by the specialists from the Institute of Eco-Museal Research in Tulcea, the Institute of Archaeology in Iasi, and the Institute of Anthropology in Bucharest, during the archaeological diggings of the *Ibida* site at Slava Rusă [4].

They are presented in Figure 2 and consist of:

-*haft – P1* (Figure 2a), discovered at *Ibida* in 2006, G Curtain wall, S3, survey C1, inventory no. 48237. The item is 44mm in length, rectangular, and ends with a pommel with a diameter of 8mm. At approximately 32.6mm from the end with the pommel, the handle has two diagonal asymmetrical incisions, and at 5.75mm from them another two very fine incisions. The weight is 6.47g. On the side to which the blade was attached, two rivets were preserved; they are positioned at approximately 25mm from each other, and most probably were part of the fixing mechanism.

-*blade of pocket-knife – P2* (Figure 2b), discovered at *Ibida* (*passim*), Nichifor donation, inv. no. 40344. The length is 51.64mm and the maximum width is of 10.65 mm. The weight is 5.52g. Only the blade is preserved, without the handle. Unfortunately, neither the connecting mechanism has been preserved. The piece was dated between the 2nd and 4th century A.D.

-*fragment of knife* - *P3* (Figure 2c), discovered at *Ibida* in 2002, G Curtain wall, S1, square 24, -1.50m, on the level (north of the wall), inventory no. 45889. The length of the blade is of 48.83 mm, and the width at the base is 24.70mm. A 19.40mm fragment of the haft has been preserved. The rivet fixating the blade to the handle can still be observed. The weight is 17.44 g. Given the current shape of the blade, its original length was probably around 130mm. The artefact was dated between the 4th and 6th century A.D.

Fig. 2. *Items discovered during the archaeological diggings at (L) Ibida (Tulcea County): a. Haft, inv. no. 48237; b. Blade of pocket-knife, inv. no. 40344; c. Fragment of knife, inv. no. 45889; d. Scissors, inv. no. 31978; e. Pincers, without inventory number; f. Fragment of knife, without inv. number*

-*scissors – P4* (Figure 2d), inventory no. 31978. The two blades have been preserved almost entirely. The length of the piece is 67.87mm, the width is 23.84mm, and the weight is 13.49g.

-*pincers – P5* (figure 2e), discovered at Tufani, without an inventory number. The artefact survived entirely, and it is composed of a 6.58mm-wide metal band, with the arms of 55mm each, curly, and with a coil with a diameter of 9.87mm. The piece weights 5.56g.

-*fragment of knife – P6* (Figure 2f), discovered at Noviodunum in 2007, without an inventory number. A 31.30mm fragment of the blade has survived, as well as a 41mm of the handle. Only one edge was usable, and the maximum width of the blade is of 15.21mm. The weight of the artefact is 6.12g.

The SEM-EDX and micro-FTIR methods were employed to investigate the above-mentioned archaeological pieces, in order to identify the materials used in their manufacturing.

a. SEM-EDX analysis

A SEM (model VEGA II, produced by the Czech TESCAN company) electronic scanning microscope was used co-jointly with an EDX detector (QUANTAX QX2 type, produced by the BRUKER/ROENTEC in Germany).

This method, alongside the visual inspection of the micro-photogram, allows for the mapping (deployment) of the atoms from the investigated area, while alongside the X-ray spectra it allows for the determining of the elemental composition (in gravimetric or molar percentages, of a micro-structure or of a selected area) and the assessment of the compositional variation along a vector running across the investigated area or section.

b. Micro-FTIR analysis

The spectra were recorded using TENSOR 27 FT-IR spectrophotometer, coupled with a HYPERION 1000 microscope; both pieces of equipment were produced by Bruker Optic, Germany.

The FT-IR spectrophotometer is a TENSOR 27 model that is most appropriate for near-IR (NIR) measurements. The standard detector is the DlaTGS, which covers the spectral range 400–600cm^{-1} and which works at room temperature. The resolution is in most cases of 4 cm^{-1}, but it can reach up to 1 cm^{-1}.

The equipment used for the investigation was made available by the Laboratory for Scientific Investigation and Conservation of Cultural Heritage Items within the Interdisciplinary Research Platform in the Field of Archaeology – *ARHEOINVEST* from the "Alexandru Ioan Cuza" University of Iasi.

3. Results and discussions

Following the SEM-EDX analysis of the structures from the surface and the cross-section, the elemental composition, in mass percentages, of the objects found during the archaeological excavations, was established (Table 1). On the basis of these results, it was possible to establish the nature of the materials used in manufacturing the objects. Thus, in the P1 haft and in the P5 pincer the main elements are copper and zinc, while in the P2 blade of pocket-knife, alongside copper and zinc, tin is also present.

The P3 fragment of knife, the P4 scissors and the P6 fragment of knife, all have iron in their composition.

Table 1. *Chemical composition of investigated items*

Index	Item/ Inv. no.	Elemental composition – mass percentages (%)													
		Cu	**Sn**	**Zn**	**Fe**	**O**	**C**	**S**	**P**	**Cl**	**Na**	**K**	**Ca**	**Al**	**Si**
P1	**Haft/ 48237**	63.659	-	14.743	0.752	8.463	9.639	-	-	0.299	-	-	-	1.149	1.295
P2	**Blade of pocket-knife/ 40344**	83.191	2.544	5.317	0.496	6.673	0.900	-	-	0.879	-	-	-	-	-
P3	**Fragment of knife/ 45889**	-	-	-	54.489	31.730	5.466	-	-	-	3.606	0.559	1.209	1.796	1.144
P4	**Scissors/ 31978**	-	-	-	67.129	30.478	0.501	0.328	0.327	-	-	-	0.329	0.591	0.317
P5	**Pincer/ w/o inv. no.**	75.877	-	16.719	-	4.939	2.465	-	-	-	-	-	-	-	-
P6	**Fragment of knife/ w/o inv. no.**	-	-	-	84.226	13.326	0.696	-	0.442	-	-	-	0.604	0.705	-

Iron, just like copper, is the main metal to be found in processed alloys that is often corroded while lying buried. The processes of chemical alteration, monolithisation, and mineralisation occurring *in situ* means that the following elements should also be present: C, O, Si, Al, Cl, etc. [3, 5, 6].

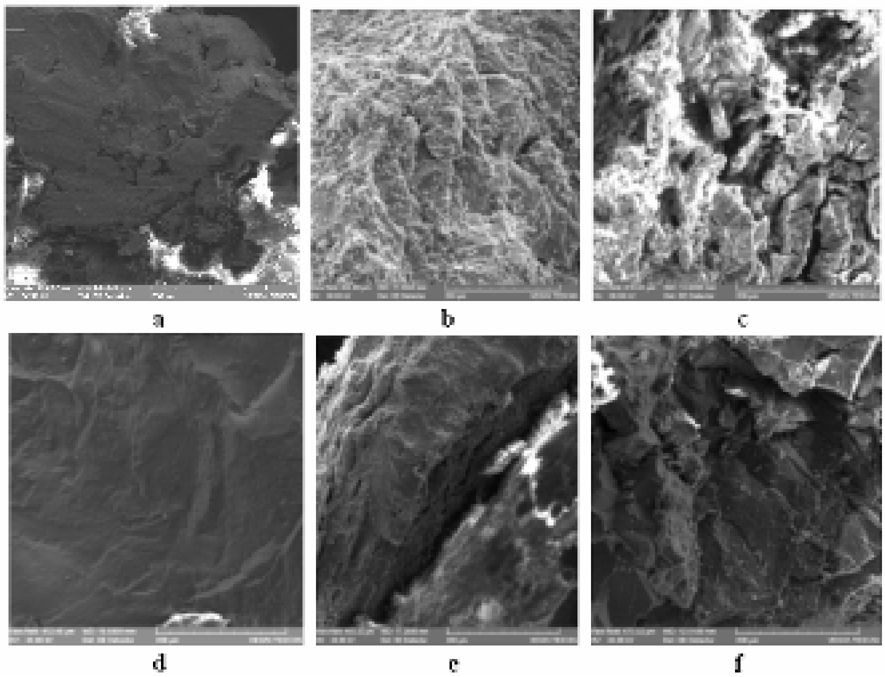

Fig. 3. *SEM images of investigated objects:*
a. Haft, inv. no. 48237; b. Blade of pocket-knife, inv. no.40344; c. Fragment of knife, inv. no.45889; d. Scissors, inv. no. 31978; e. Pincers, without inventory number; f. Fragment of knife, without inv. number

In our case, the following contaminants were identified: C, O, Si, Al, Na, K, Ca, S, P and Cl.

Because of the interaction between the soil and the metallic pieces, processes of chemical, electro-chemical, biological, etc. corrosion occur. The altered metal alloy presents on its surface a crust; nonetheless, the mechanism by which this crust is formed cannot be generalised for all types of artefacts. This crust can be thin, smooth and with a homogenous structure, or thick, rugged and with a non-homogenous structure. Significant similarities or differences can be found on objects of the same type, historical period, manufacturing technology, etc. [5, 6, 7, 8]. In the SEM images (Fig. 3), the internal structure of the analysed samples can be observed. Using the micro-FTIR analysis based on group characteristic vibrations, the nature of the corrosive products from the surface structures has been confirmed.

By comparing the obtained spectral bands with the ones from spectra libraries and from the dedicated literature [9, 10], the main components formed on the surface of the objects were identified; they constituted the residual patina which remained after the cleaning operations. Table 2 (Annex 1) presents the main spectral bands, with the representative peaks and their corresponding ions.

4. Conclusions

On the basis of the results obtained by corroborating the results of the SEM-EDX and the micro-FTIR analyses we can conclude that objects P1, P2 and P5 are made from copper-based alloys, while P3, P4 and P6 are made from iron. The objects suffered from prolonged processes of segregation towards the surface of the active metals, and deteriorated, from the surface towards the interior, by redox, acidic-basic and complexing processes assisted by monolithisation by the inclusion of contaminating elements. These features prove the considerable age of these artefacts. Oxide compounds (CuO, Cu_2O, Fe_2O_3, Fe_3O_4, SiO_2, etc.), hydrated basic carbonates ($CuCO_3{\cdot}Cu(OH)_2$, $CuSO_4{\cdot}\ 3Cu(OH)_6$, etc.), chlorine compounds ($Cu_2(OH)_3Cl$, $CuCl_2{\cdot}3Cu(OH)_2$, etc.) and other compounds were formed by the alteration processes caused by the underground lying environment [5, 6].

Acknowledgement

This work was made possible with the financial support of the Sectorial Operational Programme for Human Resources Development 2007-2013, co-financed by the European Social Fund, under the project number POSDRU/89/1.5/S/61104 with the title “*Social sciences and humanities in the context of global development - development and implementation of postdoctoral research*”.

References

[1]. I.G. Sandu, I. Sandu, A. Dima - *Modern Aspects Concerning the Conservation of Cultural Heritage,* vol. III, Autentication and Restauration of the Inorganic Material Artefacts, Ed. Performantica, Iaşi, (2006).

[2]. I. Sandu, N. Ursulescu, I.G. Sandu, O. Bounegru, I.C.A. Sandu, A. Alexandru - *The pedological stratification effect of corrosion and contamination products on Byzantine bronze artefacts*, in **Corrosion Engineering Science and Technology**, Maney Publishing, vol. 43, 3, (2008), pp. 256-266.

[3]. I. Sandu, O. Mircea, A.V. Sandu, I. Sarghie, I.G. Sandu, V. Vasilache - *Non-invasive Techniques* in the Analysis of Corrosion Crusts formed on Archaeological Metal Objects, **Revista de Chimie**, Bucharest, vol. 61, 11, (2010), pp. 1054 -1058.

[4]. D. Aparaschivei - *Cercetările arheologice de la (L?) Ibida (Slava Rusă, jud. Tulcea), Sector X (campania 2008) (I),* in Arheologia Moldovei**,** XXXII, (2009), pp.167-182.

[5]. D. A. Scott - *Copper and Bronze in Art: Corrosion, Colourants and Conservation*, Getty Conservation Institute, Los Angeles, (2002).

[6]. De Ryck, A. Adriaens, E. Pantos, F. Adams - *A comparison of microbeam techniques for the analysis of corroded ancient bronze objects*, Analyst, 128, (2003), pp. 1104–1109.

[7]. I. Sandu, C. Marutoiu, I.G. Sandu, A. Alexandru and A.V. Sandu - *Authentication of Old Bronze Coins I. Study on Archaeological Patina***,** Acta Universitatis Cibiniensis Seria F, Chemia, 9 (2006-1), pp. 39-53.

[8]. V. Vasilache, D. Aparaschivei, I. Sandu, *Scientific investigation on ancient jewels found in Ibida site, Romania*, International of Journal Conservation Science, 2, 2, (2011).

[9]. K. Nakamoto - *Infrared and Raman Spectra of Inorganic and Coordination Compounds,* Parts A and B, John Wiley & Sons, New York, (1997).

[10]. John Coates - *Interpretation of Infrared Spectra, A Practical Approach*, Encyclopedia of Analytical Chemistry, R.A. Meyers (Ed.), John Wiley & Sons Ltd, Chichester, (2000), pp. 10815–10837.

Annex 1

Table 2. *Representative peaks and spectral bands of the ions identified in the analyzed objects*

Spectral bands (cm^{-1})	**Functional group**	**Peak present in analyzed objects** (cm^{-1})	**Analyzed objects**
670-745; 800-890; 1040-1100; 1320-1530	Carbonate ion	724. 1378.1465	P1
		1340. 1497	P2
		1413. 1482	P3
		1462. 1515	P4
		723. 1376. 1465	P5
940-1120	Orto-phosphate ion	1001	P3
830-920; 1600-1900; 2150-2500; 2750-2900;	Orto-phosphate dibasic ion	1719. 1896. 2304. 2851	P1
		1675. 2635. 2307. 2862	P2
		1753.	P3
		1613. 1676. 2829	P4
		1743. 2851	P5
570-680; 960-1030	Sulphate ion	618	P3
600-660; 610-630; 900-1150	Chloride ion	965. 1126	P1
		640. 929	P4
600-700	Tin ion	654	P2
		698	P4
860 – 1175	Silicate ion	889	P1
		1130	P2
		1044	P3
		1036. 1123	P4
		887	P5
		888	P6
800 - 920	Aluminate	889	P1
		878	P2
		865	P3
		837	P4
2550-3500	Aquo and hydroxo-compounds. water of coordination	2636. 2920. 3278	P1
		3241	P2
		2999. 2585. 3173	P3
		3318. 3374. 3040. 2950	P4
		3329. 2955. 2922	P5
3500-4000	Waters related physically	3603	P1
		3527	P2
		3651	P3
		3509	P4
		3508	P6

THE ANNALS OF "DUNAREA DE JOS" UNIVERSITY OF GALATI.
FASCICLE IX. METALLURGY AND MATERIALS SCIENCE
N^0. 1 – 2012, ISSN 1453 – 083X

COMPOSITION OF SYNGAS PRODUCED BY GASIFICATION OF AGRICULTURAL RESIDUE BRIQUETTES

Daniela TASMA, Tănase PANAIT, Krisztina UZUNEANU,
Cătălin MOCANU, Raluca-Cristina BUȚURCĂ
"Dunărea de Jos" University of Galati
email: dtasma@ugal.ro

ABSTRACT

This paper summarizes the results of an experimental study on the gasification of briquettes made from different agricultural residues. There were investigated the effects of operating parameters such as temperature and excess air ratio both with a direct influence on the composition of syngas and the heating value. The results indicate that the concentrations of N_2, CO_2 and CH_4 increase with the increase in excess air ratio, while the concentrations of H_2 and CO decrease. The heating value of the syngas was found to decrease with the increase in excess air ratio.

KEYWORDS: gasification, agricultural residues, excess air ratio, syngas

1. Introduction

The use of biomass to provide partial substitution of fossil fuels has an additional importance as concerns global warming since biomass combustion has the potential to be CO_2 neutral. This is particularly the case with regard to agricultural residues or energy plants periodically planted and harvested. During their growth, these plants have removed CO_2 from the atmosphere for photosynthesis and released it again during combustion [1].

Agricultural residues have acquired considerable importance as biofuels for domestic cooking, industrial process heating, electrical power generation, and are used directly as well as in briquetted form for a variety of energy end uses [2].

Biomass gasification is a thermal conversion of solid biomass to gaseous fuel, into which the energy stored in the biomass is converted to calorific value of the produced gas.

The fuel gas obtained from gasification is called syngas, and has the following major components: carbon monoxide CO, hydrogen H_2, carbon dioxide CO_2, and small fractions of methane CH_4. The fraction of each component gas in syngas is known to vary with the type of biomass, the initial moisture content of the feedstock, particle size, operating temperature, and excess air ratio [3].

This paper presents the syngas composition resulted from the gasification of the briquettes made from agricultural residues. The results indicate that the concentrations of H_2 and CO decrease with the increase in excess air ratio, while the concentrations of N_2, CO_2 and CH_4 increase. The syngas composition is found to be similar to those reported by other researchers [4].

2. Experimental procedure

The gasification process consists of drying, pyrolysis or devolatilization, combustion or oxidation and gasification or reduction [5]. These processes are largely dependent on the parent biomass composition, moisture content, local stoichiometry, reactivity of biomass, and gasifier design [6].

Briquettes made of agricultural residues were used in the experiments. The elemental and proximate analyses of the fuels are listed in Table 1 where it can be seen that the sawdust briquettes have the highest carbon content and the lowest ash content, while the reed briquettes have the highest ash content. The briquettes obtained from 50% sawdust and 50% corn stalk have the highest content of oxygen.

***Table 1.** Fuel properties*

Fuel sample	Reed briquettes	Sawdust briquettes	Sawdust 50% + corn stalk 50% briquettes	Sawdust 50% + wheat straw 50% briquettes
Ultimate analysis (% of dry fuel with ash)				
C	52.4	53.3	49.41	50.63
H	5.91	6.28	5.90	6.12
N	0.65	1.91	0.43	0.53
S	0.0	0.0	0.0	0.0
O	33.55	35.75	40.73	38.08
A	7.85	2.77	3.54	4.64
Proximate analysis (% of wet fuel)				
Fixed Carbon	29	24.85	22.60	20.30
Volatile matter	56.70	66.55	67.40	70.10
Ash	7.30	2.60	3.30	4.40
Moisture	7	6	6.70	5.20

3. Results and discussions

The variation in the composition of the syngas produced syngas is studied by varying the different operating conditions. The operating conditions in this study are gasification temperature and excess air ratio. The main components of the syngas are CO, H_2, N_2, CO_2, H_2O and CH_4. The molar fractions of these components were measured before the second air injection. Table 2 presents the molar composition of syngas produced through gasification of sawdust briquettes, gasification temperature and excess air ratio. The influence of temperature on syngas composition is illustrated in Figure 1. The molar fraction of the CO_2 increases with the decrease of excess air ratio.

***Table 2.** Molar composition of syngas produced by gasification of sawdust briquettes*

Temperature [°C]	Excess air ratio	CO_2	CO	H_2	CH_4	N_2	NH3	H_2O	LHV
700	0.33	0.0638	0.253	0.1950	0.0049	0.4518	0.0011	0.0304	5.47
750	0.27	0.0344	0.311	0.2286	0.0039	0.4018	0.0011	0.0193	6.53
800	0.23	0.0168	0.3465	0.2511	0.0029	0.3704	0.0011	0.0112	7.18
850	0.22	0.008	0.3648	0.2641	0.002	0.3538	0.0011	0.0063	7.52
900	0.21	0.0039	0.3735	0.271	0.0014	0.3456	0.0011	0.0036	7.68

The molar fraction of CO is the most significant contribution to the heating value of the syngas, its value increasing with the gasification temperature.

The increase of the gasification temperature causes a linearly decrease of the N_2 molar fraction.

The useful energy content in the syngas can be quantified by the syngas heating value. Figure 1 shows the variation of lower heating value against temperature.

It is evident that the lower heating value increases with the increase of temperature.

The lower heating value of the syngas ranges from 5.47 MJ/Nm^3 to 7.68 MJ/Nm^3.

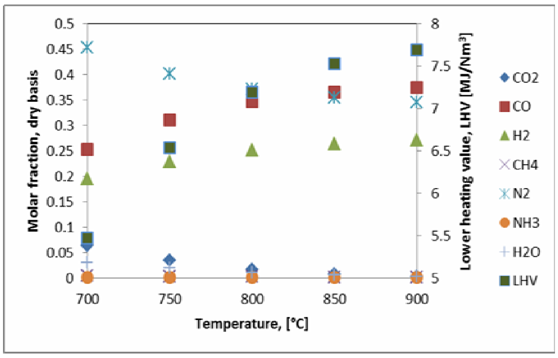

***Fig. 1.** Influence of the temperature on syngas composition for sawdust briquettes*

Figure 2 presents the variation of H_2 molar fraction as a function of the gasification temperature for all briquettes made from agricultural residues. As can be seen, the increase in temperature causes an increase of the H_2 molar fraction.

The highest content of the H_2 in the syngas was obtained by gasification of briquettes made from sawdust 50% + wheat straw 50%. The minimum value of the H_2 molar fraction was obtained by gasification of sawdust briquettes.

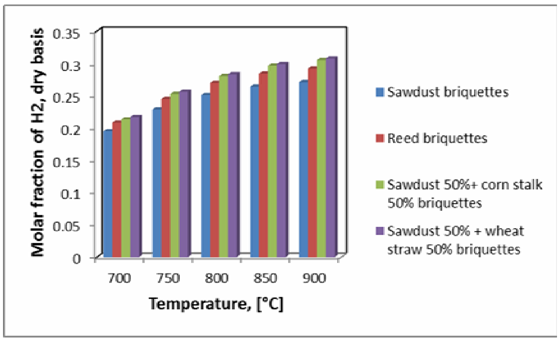

Fig. 2. *Variation of molar fractions of H_2 with temperature*

The molar fraction of H_2 has an important contribution in the calculating of syngas heating value.

Figure 3 shows the variation of the CO_2 molar fractions with temperature. It can be observed that the increase in temperature decreases the CO_2 content in the syngas.

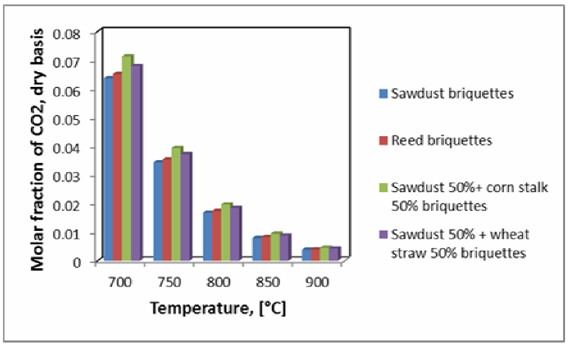

Fig. 3. *Variation of molar fractions of CO_2 with temperature*

Figure 4 shows the variation of the CO molar fractions with temperature.

The increase in temperature increases the CO content in the syngas. The highest content of the CO in the syngas was obtained by gasification of briquettes made from sawdust 50% + corn stalk 50%.

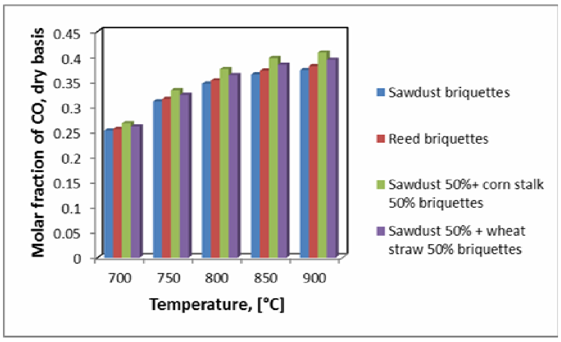

Fig. 4. *Variation of molar fractions of CO with temperature*

Figure 5 presents the variation of CH_4 with temperature. The molar fraction of CH_4 is very low and this decreases with the increase of the temperature. The highest concentration of CH_4 was obtained for gasification of sawdust 50%+wheat straw 50% briquettes.

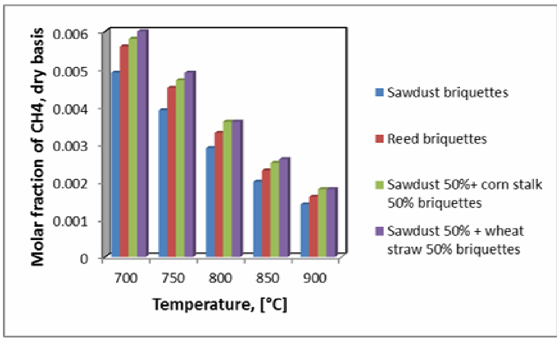

Fig. 5. *Variation of molar fractions of CH_4 with temperature*

5. Conclusions

The syngas composition is strongly influenced by temperature and excess air ratio. An increase in temperature resulted in an increase in the concentrations of H_2 and CO and a lower CO_2 production.

The highest content of the H_2 in the syngas was obtained by gasification of sawdust 50% + wheat straw 50% briquettes for an excess air ratio $\lambda=0.18$ and a temperature equivalent with 900°C. The minimum value of the H_2 molar fraction was obtained by gasification of sawdust briquettes for an excess air ratio $\lambda=0.33$ and a temperature equivalent with 700°C.

The highest contents of the CO and CO_2 in the syngas were obtained by gasification of briquettes made from sawdust 50% + corn stalk 50%.

The molar fraction of CH_4 is very low and this decreases with the increase of the temperature.

The lower heating value of the syngas was found to decrease with the increase in excess air ratio.

Acknowledgements

The work of this paper was supported by Project SOP HRD – EFICIENT 61445/2009 and SOP HRD – TOP ACADEMIC 76822.

References

[1]. J. Werther, M. Saenger, E.-U. Hartge, T. Ogada, Z. Siagi - *Combustion of agricultural residues*, Progress in Energy and Combustion Science, (2000), Vol. 26, pg. 1–27.

[2]. A. Kumar, P. Purohit, S. Rana, T. C. Kandpal - *An approach to the estimation of the value of agricultural residues used as biofuels,* Biomass and Bioenergy, (2002), Vol. 22 , pg. 195 – 203

[3]. S. M. Atnaw, S. A. Sulaiman, S. Yusup - *Prediction of Calorific Value of Syngas Produced from Oil-Palm Fronds Gasification,*. 3rd National Postgraduate Conference, Tronoh. (2011).

[4]. J.F. González, S. Román, D. Bragado, M. Calderón - *Investigation on the reactions influencing biomass air and air/steam gasification for hydrogen production,* Fuel Processing Technology, (2008), Vol. 89, pg. 764 – 772.

[5]. K. Jaojaruek, S. Jarungthammachote, M. K. B. Gratuito, H. Wongsuwan, S. Homhual - *Experimental study of wood downdraft gasification for an improved producer gas quality through an innovative two-stage air and premixed air/gas supply approach,* Bioresource Technology. 2011, p.doi:10.1016/j.biortech.2010.12.024.

[6]. P. C. Roy, A. Datta, N. Chakraborty - *Modelling of a downdraft biomass gasifier with finite rate kinetics in the reduction zone,* International Journal of Energy Research, (2009), Vol. 33, pg. 833-851.

THE ANNALS OF “DUNAREA DE JOS” UNIVERSITY OF GALATI.
FASCICLE IX. METALLURGY AND MATERIALS SCIENCE
N^0. 1 – 2012, ISSN 1453 – 083X

OBTAINING AND CHARACTERIZING TIN-LEAD COATINGS ON STEEL BAND

Tamara RADU, Anisoara CIOCAN, Maria VLAD, Stela CONSTANTINESCU
„Dunărea de Jos” University of Galati
email: tradu@ugal.ro

ABSTRACT

The experimental research was at the basis of the hot immersion coating technology with Sn-Pb alloy of the steel bands presented in the study. The characterization of these layers was achieved through microscopic analyses and the analysis of resistance to corrosion. Coatings with four tin-lead alloys were carried out. The micro-structural aspect of the tin-lead alloys, the aspect of the covered band surface, the micro-structure of the layers, the layer thickness variation according to the duration of the immersion and the chemical composition of the layers are presented. The resistance to corrosion was assessed through the gravimetric index. The samples were exposed in sea water for five weeks. The corrosion speed was determined for every type of coating, according to the period of exposure to the corrosive environment and the kinetic process for the time intervals studied.

KEYWORD: tin lead coatings, structure, corrosion

1. Introduction

The tin alloys are important in the production of coatings through hot immersion. The most important of these are the tin-zinc, tin-nickel, tin-cobalt, tip-copper and tin-lead alloys. The tin-lead coatings are mainly used for protection against corrosion and for preparing the surfaces for soldering. The protective layer made of Pb-Sn alloys gives the steel plate a good resistance to corrosion, a very good capacity for welding and soldering, and improves deformability.

The coating presents a high resistance to corrosion in the atmosphere which contains sulphur agents, in environments with oil products, in sulphuric and phosphoric acids. In the case of corrosion resistance of the plate covered in Pb-Sn alloys, a very important role is played by the Fe-Sn transition layer, formed at the separation limit of the steel-coating. According to the iron-tin equilibrium diagram, the inter-metallic compound $FeSn_2$ is formed with 80.95% tin, stable up to 496°C. Like tin, this material presents a crystalline tetragonal structure. The $FeSn_2$ layer gives a good coating adherence to the steel support but, because of its fragility, it is not recommended to go beyond a certain thickness.

The reduction of the tin content during the coating, through its replacement with lead, influences the $FeSn_2$ layer by reducing it and worsens its adherence properties. In order to compensate this shortcoming, modifications were made in the fabrication technology of the lead plate with a low content of tin, respectively applying a more intense capping process, using new fluxing etc., to activate the surface.

2. Experimental research

For obtaining Sn-Pb alloy coatings, the following technological steps were followed:

-preparing the surfaces of the steel bands;

-development of tin alloys with different lead concentrations;

-achievement of deposits through immersion in melt;

-cooling of the samples.

Preparing the steel surface in view of coating is a very important stage, because the perfect cleaning of the surface determines the obtaining of an adherent layer, uniform and without flows.

The surface of the samples was chemically degreased and then degreased in organic solvents (acetone), etched in hydrochloric acid (17% concentration) and covered in zinc chloride flux and ammonium chloride dried at 150 °C.

The sample steel bands on which the deposit was achieved were 0.18mm thickness; their chemical composition is shown in Table 1.

***Table 1.** Chemical composition of the support steel bands, in %*

C	Si	Mn	P	S	Al	As	Ti	V	Cu	Ni	Cr	Mo
0.025	0.015	0.210	0.013	0.010	0.046	0.004	0.002	0.001	0.005	0.008	0.025	0.001

***Table 2.** Elaborated Sn-Pb alloy chemical composition*

Alloy code	Composition, [%]		Alloy melting temperature [˚C]
	Sn	Pb	
1	80	20	180
2	70	30	185
3	50	50	220
4	32	68	260

The immersion temperature was 30-50°C above that of the alloy melting temperature, and the immersion duration varied between 3 and 12 seconds.

A first observation is that a growth in the alloy lead concentration influences the aspect of the surface. The aspect of the surface varies from silver in the case of coating with an alloy with a high content of tin (80%Sn-20%Pb), to opaque dark grey in the case of the layers obtained in alloy code 4 (32%Sn-68%Pb). The surface analysis through optical microscopy shows a difference in the solidification process, respectively a structure with fine dendrites for alloy code 1 compared to the other alloys, as can be observed in the micrographs in Figure 1.

The increase of the dendrite dimension is influenced by the increasing of the solidification interval [1] of the alloy codes 2 and 3, as compared to 1 and 4.

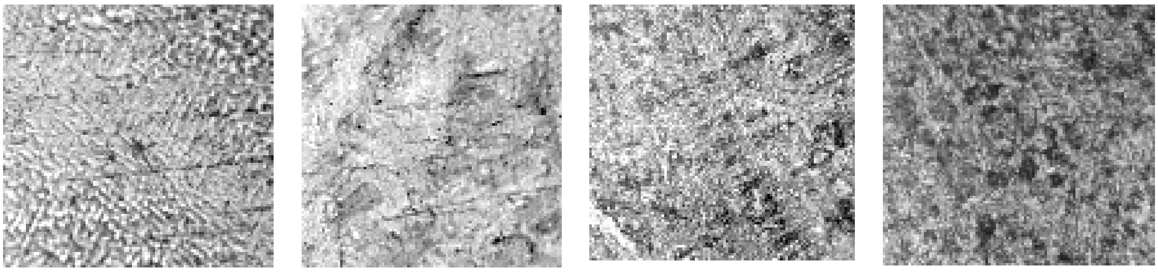

a) 80%Sn-20%Pb b) 70%Sn-30%Pb c) 50%Sn-50%Pb d) 32%Sn-68%Pb

***Fig. 1.** Aspect of the probe surfaces covered with tin- lead alloys (immersion duration 9 seconds), X100*

Figure 2 presents the micro structural aspect of the lead-tin alloys, elaborated in view of coating the steel bands. According to the phase equilibrium diagram [2], depending on the lead content, what may be observed is an increase in the eutectic quantity, with the solid solution α in the case of hypoeutectic alloys [3, 4] codes 2 and 3 and with the solid solution β in alloy code 4.

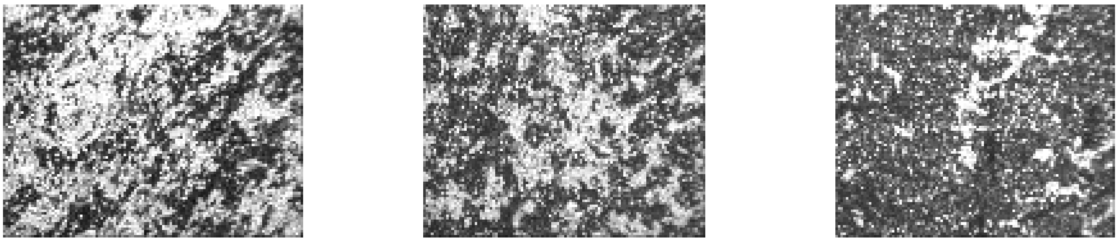

a) 70%Sn-30%Pb b) 50%Sn-50%Pb c) 32%Sn-68%Pb

***Fig. 2.** Microstructural aspect of the tin-lead alloy, X100*

During the research carried out, the determination of the alloy layer thickness deposited on the steel bands was achieved metallographic ally as the average of three measurements in different areas. As can be observed from the data presented in Figure 3, the layer thickness depends on the immersion duration, as well as on the chemical composition of the alloy deposited.

The increasing of the lead concentration and immersion period over 6 seconds determined increasing of thickness for the alloy coating codes 3 and 4. In the case of alloys with a low content of lead (20-30% Pb), the immersion duration does not influence the layer thickness significantly. This can be explained due to the much better flow of the alloys which are rich in tin [5, 6].

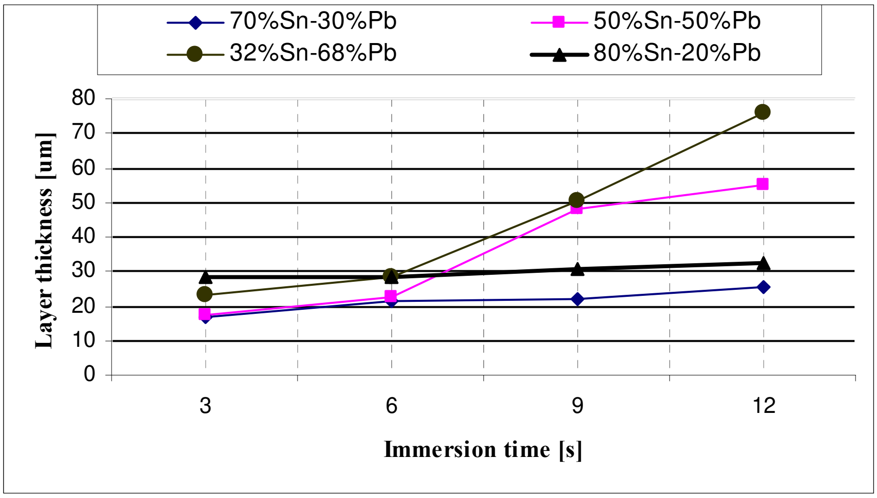

Fig. 3. *Thickness variation of the Sn-Pb alloy layers according to the immersion duration*

The analysis of the microstructures deposited shows that these are uniform and present a structure similar to that of the alloys, thickness varying according to the immersion duration. Figures 4 and 5 show the microstructural aspects of the coatings, with the layer thickness specified.

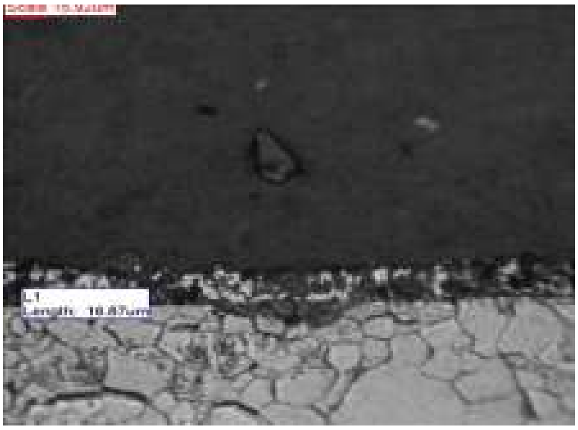

Fig. 4. *Microstructure of the 70% Sn 30% Pb alloy coating, immersion duration: 6 seconds, temperature 185[˚C]*

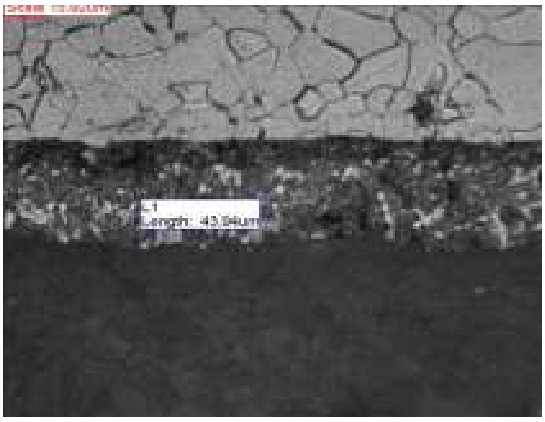

Fig. 5. *microstructure of the 32%Sn-68% Pb alloy coating immersion duration: 9 seconds, temperature 185[˚C]*

In order to determine the corrosion speed, some samples were extracted from each type of coating resulting from a 6 second immersion, where the layer thickness was approximately equal.

The corrosive environment used was a 3% NaCl solution. The study was carried out for five weeks. The samples were weighed at 7 days intervals, after they were washed in water and then dried.

In order to determine the corrosion speed, the gravimetric method was used. The corrosion speed was determined using the relation:

$$v_{cor} = \frac{m_{cor}}{S \cdot t} \qquad (1)$$

where: v_{cor} - gravimetric index [g/m^2·h]; m_{cor} - mass loss through corrosion [g]; S - surface area, [m^2]; t - corrosion duration [h].

Both the corrosion speed at different time intervals and the speed during the intervals were determined; the variation curves were also drawn.

The corrosion speed depends of the chemical composition of the alloy deposited on the steel bands, on the thickness of the deposited layer and of the exposure duration of the samples to the corrosive environment [7, 8, and 9]. Figure 6 shows the behavior to corrosion of the analyzed layers, according to the duration exposure to the corrosive environment. Analyzing the corrosion test results, we may observe a similar behaviour of the alloy coatings 2 and 3.

This represents a continuous decrease of the corrosion speed after the first three weeks (504 hours). The alloy layers with a lower content of alloying elements (codes 1 and 4) have a lower corrosion speed after 168 hours of exposure, but an increased corrosion speed after two weeks and a decreased one after 504, with larger values however as compared to alloy codes 2 and 3.

The behaviour after 672 hours and after 840 hours respectively becomes the same for all types of alloy, in the sense of a strong increase of the corrosion speed.

The best behaviour is at 32% Sn and 68% Pb. The increase of the lead content in the coating alloy improves the resistance to corrosion in the studied conditions.

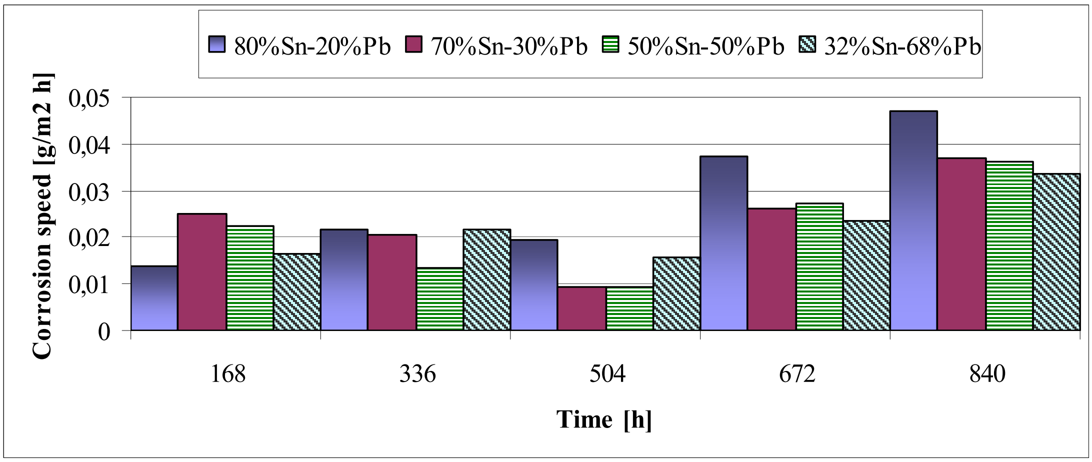

***Fig. 6.** Corrosion behaviour of the analysed layer*

Analysing the kinetic corrosion process for each alloy presented in Figure 7, we may also observe the similar behaviour at corrosion of the alloy layer codes 1 and 4, and of those in code 2 and 3 respectively.

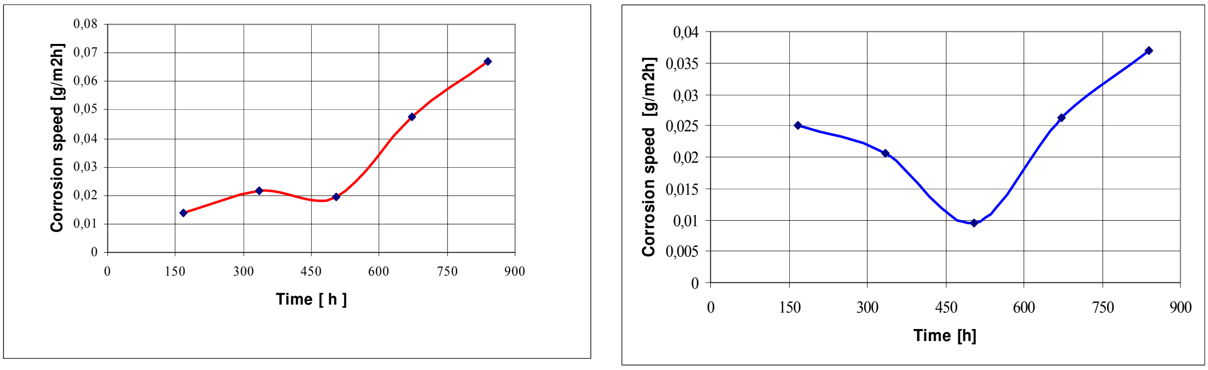

a) 80%Sn-20%Pb

b) 70%Sn-30%Pb

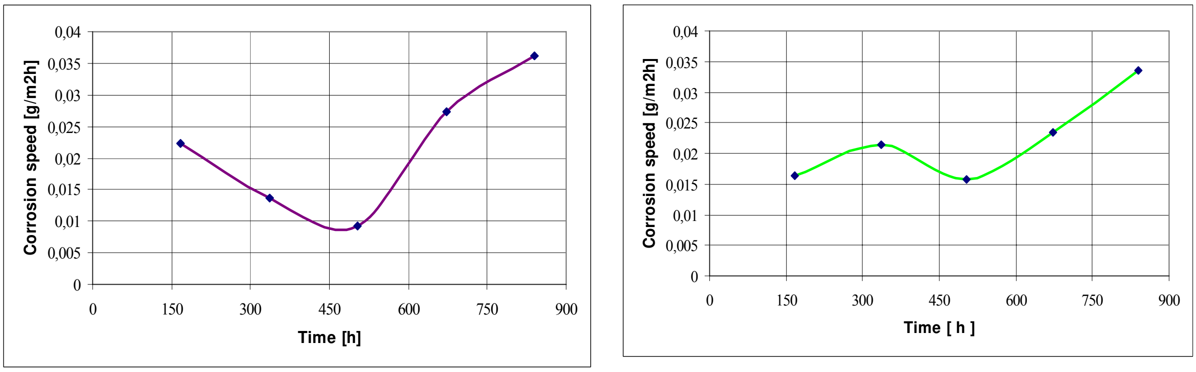

c) 50%Sn-50%Pb *d) 32%Sn-68%Pb*

Fig. 7. *Kinetics of the corrosion process for each type of coverage studied*

3. Conclusions

-The increase in the alloy’s lead concentration influences the aspect of the surface, which varies from silver in the case of a coating made from alloys with high tin content (80%Sn-20%Pb) to opaque dark grey in the case of the layers obtained from alloys with 32% Sn and 68% Pb.

-The increase of the immersion duration above 6 seconds leads to a significant increase of the layer thickness, in the case of alloys which are rich in lead.

-The microscopic aspect of the surface also shows a difference in the solidification process of the layer: a structure with fine dendrites in the case of alloy with 80 % Sn – 20 % Pb respectively, as compared to the other alloys (thank to increasing of the alloys solidification interval).

-The tin-lead alloy microstructure shows an increase in the eutectic content, along with the solid solution α (in the case of hypoeutectic alloys) and along with small quantities of solid solution β in the hypereutectic alloy.

-The analysis of the microstructures of the deposited layers shows that these are uniform and present a similar structure to that of the alloys.

-The corrosion test shows good deposit behaviour at corrosion; analysed, they present values close to the corrosion speed in time.

-The kinetics of the corrosion process shows a significant increase of the corrosion speed in weeks 4 and 5 for all the studied layers.

-The increase of the lead content in the coating has a positive influence on the resistance to corrosion.

References

[1]. Alexandru H.V., Berbecaru C. - *Ştiinţa materialelor - Creşterea cristalelor*, Ed. Universităţii din Bucureşti, (2003).

[2]. Yancy W.Riddle - *Metals Conservation*, Summer Institute, Alloys & Their Phase Diagrams, University of California (2006).

[3]. William D.Callister - *Binary Phase Diagrams*, 2nd ed., Vol. 3.

[4]. Harsh Menon - *Lab.Report on Lead-Tin Phase Equilibrium,* (2006).

[5]. W. E. Hoare, E. S. Hedges & B. T.K. Barry - *The Technology of Tinplate,* Ed. Arnold (Publishes) Ltd., London, (2004).

[6]. Silviu Crăciun - *Cositorirea la cald a materialelor metalice,* 1976.

[7]. Tamara Radu, Stela Constantinescu, Lucica Balint - *Materiale metalice rezistente la coroziune.* Editura Ştiinţifică F.M.R., (2004).

[8]. Opre Flore, Florentina Ionescu, Tamara Radu - *Coroziune materialelor metalice,* Editura Ştiinţifică F.M.R., (2000).

[9]. Stefan Dragomir, Silviu Macuta, Mirela Dobrot - *Functional parameters and vibration measurement, performed on a strip tandem mill cold,* 28-th Danubia Adria Symposium on Advances in experimental mechanics, Siofok Hungary, 28sep-01oct.2011.

THE ANNALS OF “DUNAREA DE JOS” UNIVERSITY OF GALATI.
FASCICLE IX. METALLURGY AND MATERIALS SCIENCE
N^{0}. 1 – 2012, ISSN 1453 – 083X

CHARACTERISATION OF CVD NIOBIUM CARBIDE COATINGS ON HARD CARBIDE SUBSTRATE

Stela CONSTANTINESCU, Maria VLAD, Tamara RADU
University “Dunarea de Jos“ of Galati
email: constantinescu_stela@yahoo.com

ABSTRACT

Hard coatings are often used for mechanical properties such as wear and friction resistance. The corrosion behaviour may also be an important criterion for industrial applications of these coatings. In this paper, the protective behaviour of niobium carbide coatings onto hard carbide substrate was investigated in 3% NaCl and 1M H_2SO_4 solutions. The corrosion behaviour of the carbide coatings depends not only on the intrinsic electrochemical properties of the coatings, but depends also by the surface defects such as roughness, deposited droplets during CVD process and mainly by pinholes, cracks and scratches. The experiments conducted to obtain thin layer of carbide through the vapour chemical deposition method have followed an original path to obtain NbC directly in the working room thus avoiding the import of these hazardous substances.

Characterisation of coating deposed by CVD method was done using scanning electron microscope (SEM), X-ray diffractometer (XRD) and Knoop hardness. Scanning Electron Microscope was used to investigate the coating morphology and interface structure. X-ray mapping were also performed to characterise the elements in a semi-quantitative analysis. Dron X-ray diffractometer with Mo K_{α} radiation operating was used for phase(s) identification. Microhardness value (Knoop hardness) measured in the coating layer was 30.000 MPa.

KEYWORDS: niobium carbide, hard coatings, saline and acidic solutions, corrosion

1. Introduction

Niobium carbide coatings find extensive applications in tribological, mechanical and even decorative applications. CVD NbC coatings usually show only moderate or even poor corrosion protection for hard carbide substrates.

The poor corrosion performance is not due to the intrinsec corrosion behaviour of the carbide coating itself. It results from small structural defects, pores and crack formed during or after deposition, which act as channels for the corrosion of substrate [1].

We investigated the corrosion behaviour in saline and acid solution of niobium carbide coatings elaborated by CVD process. If the vapour chemical deposition takes place within a tubular continuous reactor, a gas carrying the reacting species is passed over the sub-layer. At the sub-layer surface, the reacting elements undergo a numbers of chemical reactions leading to product formation. Parts of the products are deposited on the sub-layer and part of it goes back to the gas stream. Before examining the vapour chemical deposition reactions it must be determined if the reaction is possible thermodynamically. The reaction will be possible thermodynamically if the calculated concentrations (partial pressures) of the reactants, under equilibrium conditions, are less than their original concentrations.

The calculation of the equilibrium concentrations from the equilibrium constant involves a good choice of the number of gas spaces which can be higher than two and the number of independent relations a relation implies the equilibrium expression depending on the free standard reaction energy and temperature.

The other relation consists in that the system pressure is the sum of the partial pressures. If some reactants possess more than one valence state, the reaction should contain the reactant under its most stable valence state. Hard alloys made out of metallic carbides manufactured to an industrial scale for cutting processing can be divided in two categories, according to their use. The second category of industrial products comprises the alloys out of many types of carbide used in cutting process of materials with long and continuous chips (all sorts of steel).

2. Methods

2.1. Experiments

The electrochemical techniques used to characterize the corrosion behaviour of coated samples are linear voltammetry [2]. Linear sweep voltammograms were recorded in the potential range from - 1000mV to 1000mV at the scan rate of 50mV/min using PGP 201 potentiostat.

A three electrode system with an electrochemical cell volume of 100mL was used to perform the experiments [3].

The auxiliary electrode was a platinum sheet and the reference electrode was saturated calomel electrode. The working electrode was the experimental samples which has an electroactive area of 1cm^2.

The sample geometry is shown in Table 1.

Table 1. *The constructive and active geometry of the plates*

Plates type	**Utilisation group**	**The worked material**	**The plate geometry**							
			Constructive				**Active**			
			α	γ	χ	λ	α	γ	χ	λ
SNUN 15.04.08	K20	White Cast iron	0	12	60	0	8	4	40	0

The corrosion behaviour of the layers has been determined by introducing in two corrosive environments: 3%NaCl and 1M H_2SO_4 solutions, at room temperature.

2.2. Characterisation

Characterisation of coating deposed by CVD method was done using scanning electron microscope (SEM) and X-ray diffractometer (XRD). The NbC coated plates feature higher endurance capabilities than those uncoated for the same cutting speed both for steel and white cast iron.

The parameters of the cutting conditions were chosen in the range of the values used on the working machines at the Arcelor Mittal Steel Galati [4].

Table 2. *Domains of the parameters values of the cutting conditions*

Plate type	**Processed material**	**n**	**v**	**s**	**t**
		[rot/min]		[mm/rot]	[mm]
SNUN 15.04.08 K20	white castion	450	110	0.096	0.5
		500	123	0.096	0.5
		530	130	0.096	0.5
		570	140	0.096	0.5
		610	150	0.096	0.5
		630	154	0.096	0.5

In Table 2 the values of the parameters of the cutting conditions are: n - rotation speed [rot/min]; v - speed cutting [mm/min]; s - advance [mm/rot]; t - deep cut [mm].

The operation of the latter is based on a housing which cuts the deposited NbC layer. Samples for metallographic analyzes were prepared by polishing, this prevented damage to the dissimilar interface (strate – substrate) during polishing SEM was used to investigate the coating morphology and interface structure. X-ray mapping were also performed to characterise the elements in a semi-quantitative analysis. Dron X-ray diffractometer with Mo K_α radiation operating was used for phase(s) identification.

The micro hardness tests show that we have NbC, value $HV_{0,05}$ = 30000MPa is in good agreement with the data from the literature [5].

3. Results and discussion

The optimum layers in the cutting process are the NbC layers having thickness within 4 - 10μm above these values, the layers loose tenacity and become fragile. As result of the thermal treatment which means heating up to 1130^{0}C degrees for various exposure times, layer thickness with 2.5-10μm were achieved [6]. The thickness of the thin layers increases with the time of exposure to the working temperature as illustrated in fig.1.

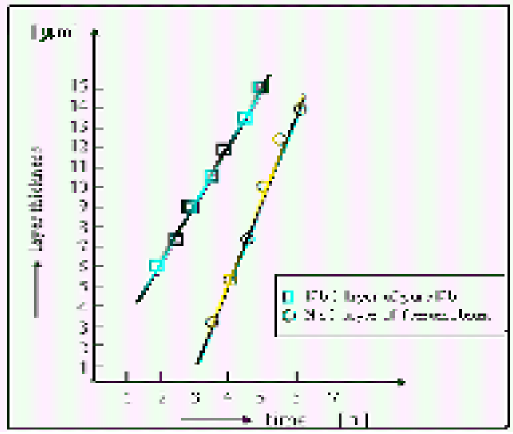

Fig. 1. *The thickness of the thin NbC layers increases with time*

Micro-hardness of WC-NbC-Co alloys is affected by a large number of elements connected to the raw material, purity and component dispersion in the alloy and the solid solution quality and grain size of components. In the factory process, these elements are playing an ultimate role in effective micro-hardness measurement of the material with a given chemical composition (fig. 2).

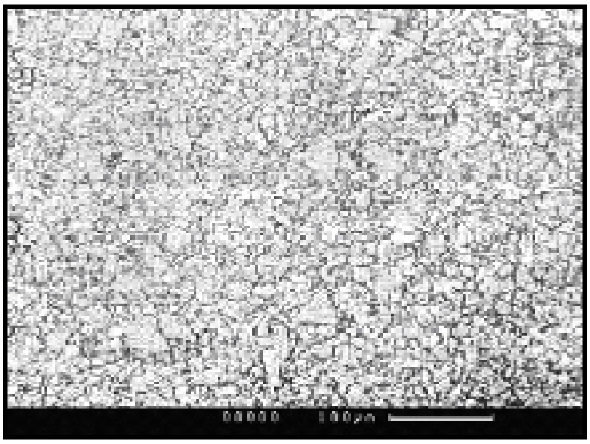

Fig. 2. *Metallographic appearance of alloy with 80%WC, 12%NbC, 8%Co, x1500*

Micro-hardness is not a constant like Vickers hardness, in spite of the geometrical similarity, but decreases with higher testing charges depending on the size of the print.

Measurements were made on NbC covered thin plates which thickness range between 6, 8 and 10µm [7, 8].

Micrographies, figs. 3, 4 and 5 shows a layer which is uniform and homogenous over the entire depth.

Figure 3 clearly show a strong interface between NbC and the substratum.

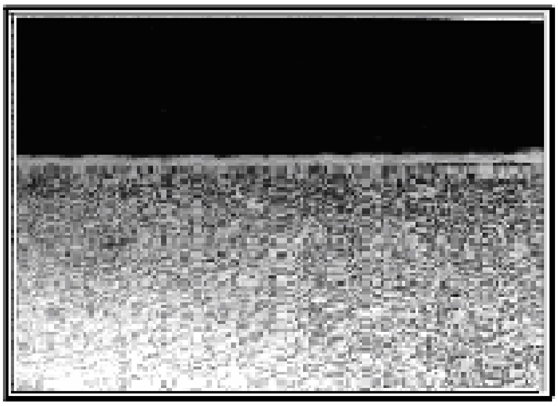

Fig. 3. *SEM micrograph of the cross section of NbC coating showing strong stratum - substratum interface, x2000*

There is a clear indication that metallurgical bond formed at the fusion zone. Figure 4 exhibits the coating morphology at a higher magnification. A fine grained structure of the coating is observed with some surface porosities. However, the coating is free from any cracks.

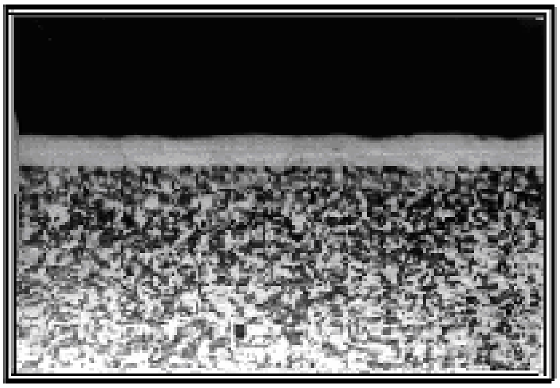

Fig. 4. *SEM micrograph of the NbC coating showing coating morphology, x2000*

Fig. 5. *SEM micrograph of the cross of NbC coating showing micro-hardness, x2000*

Microhardness value (Knoop hardness) measured in the coating layer was 30,000MPa while on substrate the hardness was 17,000MPa. Figure 5 is the SEM micrograph of the cross section of the coating and substrate with microhardness indentations. The small indentations in the coating layer are indication high hardness values as compared to the substrate which shows a large indentation.

The indentation at the interface is of intermediate size in accordance with micro- hardness values. No crack initiation or propagation is observed from any of these indentations.

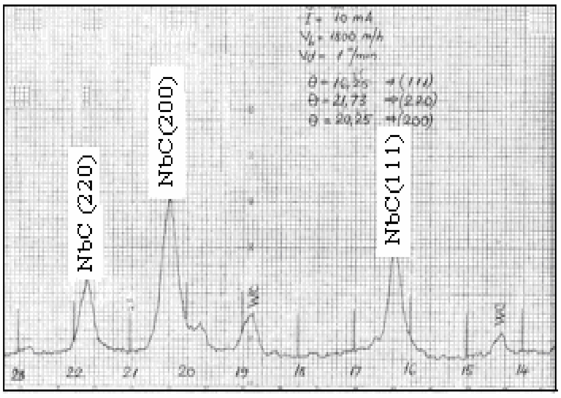

Fig. 6. X- ray diffraction spectrum of NbC coating

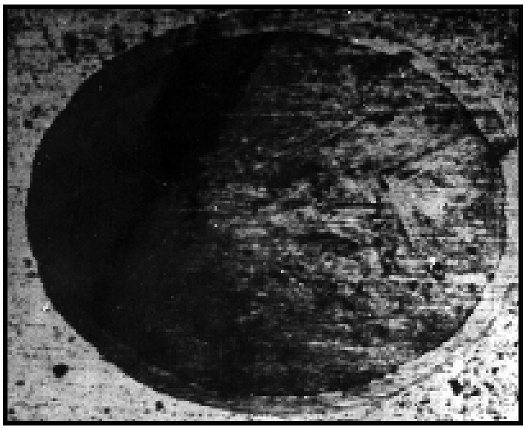

Fig. 7. The sphere shell of NbC by the Kalotest

The niobium carbide coating diagram (Figure 6) presents diffraction lines which are characteristic the most intense peak of NbC compound corresponds to the (200) diffraction plane.

The values of the thin NbC layers as measured by the Kalotest (fig.7) device are in good agreement with the values measured by microscopic analysis but slightly lower.

The steel ball diameter is 12mm. Since the shell diameter is much less than that of the ball.

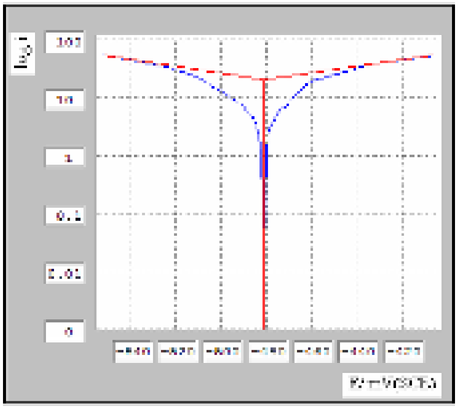

Fig. 8. Tafel method applied for corrosion in 3%NaCl

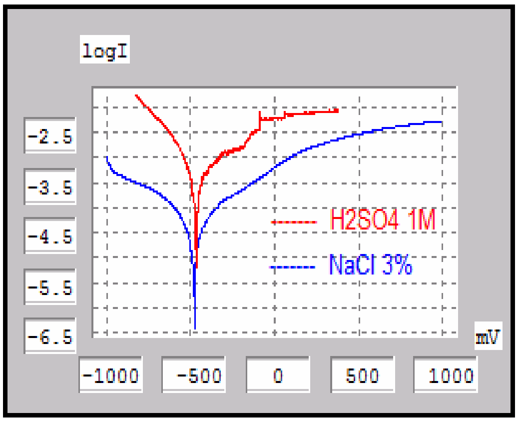

Fig. 9. Tafel curves in two corrosive environments 3% NaCl solution and 1M H_2SO_4

From the experimental data obtained from electrochemical measurements we chose the Tafel method to study the corrosion behaviour (exemplified in figure 8 for polarization curves obtained in 3%NaCl). The figure 9 presented the Tafel curves obtained in two corrosive environments tested. Corrosion potentials are very close but the corrosion current is higher in H_2SO_4 solution [9].

The parameters from Tafel curves are summarized in table 3.

Table 3. Electrochemical parameters of the corrosion process

Corrosive environments	**E_{corr}**	**i_{corr}**
	[mV]	[μA/cm^2]
3%NaCl	-480.7	0.0209
1M H_2SO_4	-467.0	0.0966

Figure 10 shows the anodic polarization curve in case of NbC layer immersed in 3%NaCl. This curve presented the specific zones: active, passive and trans-passive. The corrosion process take place into active zone, respectively the metal passes into corrosive media as ions [10].

In this interval the current density is increased up to a critical value (i_{crt}) and then start to decline until the passivation potential (app. 250mV). The passivation is the result of formation of corrosion products film [11]. In transpassive zone, the oxide film starts to dissolve oxidative.

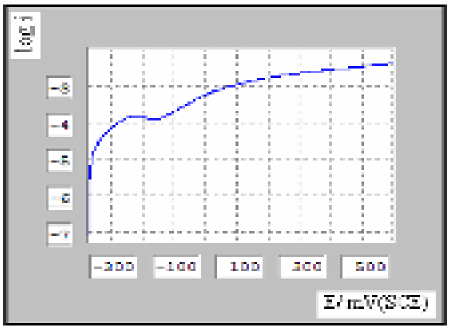

Fig. 10. *Anodic polarization curves in 3% NaCl solution*

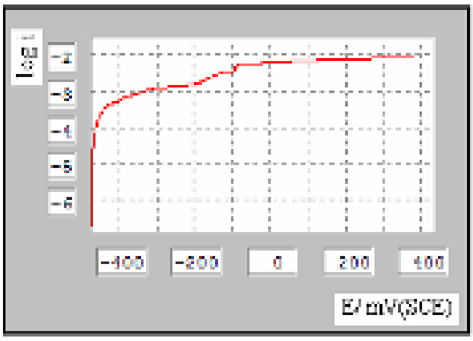

Fig. 11*. Anodic polarization curves in 1M H_2SO_4 solution*

Figure 11 shows the anodic polarization curve in case of NbC layer immersed in 1M H_2SO_4 solution. This curve shows the absence of passivation process and quickly corroded to 480mV. At increase the potential, above 400mV, continue the corrosion process slowly but constantly [12]. Test results shows a good corrosion behaviour of the NbC layer in corrosive environments tested. Higher polarization resistance and lower corrosion current shows better corrosion behaviour in 3%NaCl solution.

4. Conclusions

These coatings have good wear resistance, abrasion resistance, corrosion resistance and a strong stratum -substratum interface. We would like to underline that our condition tests are rather severe for the coated samples and lead to high corrosion rates. Nevertheless, long immersion duration does not alter the morphology of the NbC coating.

The coating is fine grained, adherent, dense and fee from cracks. However, some porosity is observed in the coating layer.

For NbC coatings, new open porosity appears and induces the peeling off of the coating due to corrosion products accumulation. These pores essentially come from the detachment of droplets previously deposited during the CVD process.

The NbC layers presented good corrosion behaviour in two corrosive environments: 3%NaCl solution and 1M H_2SO_4 solution, tested at room temperature. Corrosion potentials are very close but lower corrosion current shows better corrosion behaviour in 3% NaCl solution. The later coating should be considered for corrosion applications only if the porosity, inherent to the CVD process, is post-sealed (for instance oxidation, treatment). The niobium carbide coating would provide a very efficient protection against corrosion in saline solution.

References

[1]. S. Constantinescu - *Metals properties and physical control methods*, Didact. and Pedag. Publishing House, ISBN 973 – 30 – 1709, Bucharest, Romania, (2004).

[2]. M. D. Gavril (Donose), C. Gheorghies, A. M. Cantaragiu, D. C. Vladu (Radu), S. Donose - *Effect of acidic environment on Cu-Al_2O_3 codeposition,* The Annals of" Dunarea de jos "University of Galati, Fascicle IX. Metallurgy and Materials Science, No.4, (2011), ISSN 1453 – 083X, p.16.

[3]. P. Hagioglu, C. Gheorghies, A. M. Cantaragiu, Boiciuc, N. Tigau - *Corrosion behaviour of Tombac used in cult objects manufacturing,* The Annals of" Dunarea de jos "University of Galati, Fascicle IX. Metallurgy and Materials Science, No.2, (2009), ISSN 1453 – 083X, p.1159.

[4]. S. Constantinescu, T. Radu - *Advanced methods of obtaining thin coats,* Ed.Ştiinţifică F.M.R. ISBN 973-8151-25-2 Bucureşti, (2003).

[5]. S. Constantinescu - *Studies on Thin Carbide and Nitride Layers Deposition on Metal Basis*, Based on Chemical Reaction at High Temperatures, Academic Thesis, Galati, (1998).

[6]. S. Constantinescu, T. Radu, M. Vlad, L. Orac - *Wear-resistence of the WC-Co alloys used for short chip materials cutting,* Proceedings GEOENV 2008, Geoenvironment and Geotechnics, Publisher by Heliotopus Conferences, ISBN 978-960-6746-01-7, Millos, Greece, (2008).

[7]. S.E. Rodil, J.J. Olaya, S. Muhl, B. Bhushan, G. Wei - Surf. Coat. Technol. 201 (2007) 6117.

[8]. S. Constantinescu - *Nitride coatings on widia substrate for mechanical applications*, **J**ournal Surface Engineering vol., p.77-81, (2009), ISSN 0267-0844, www.ingentaconnect.com.

[9]. M Tawfik., A. A. Alfantazi, E. Asselin - *Corrosion of niobium in sulphuric and hydrochloric acid solutions at 75 and 95°C*, Corrosion Science, 49 (2007) 694–710.

[10]. A. Robin- *Comparative study of Nb, Nb–10W, and Nb–16Ta–12W corrosion behavior in sodium hydroxide solutions*, Electrochimica Acta, 49 (2004) 1915–1923.

[11]. A. Robin - *Corrosion behaviour of niobium in sodium hydroxide solutions,* Journal of Applied, Electrochemistry 34 (2004) 623–629.

[12]. L. Orac, V. Grechanyuc - *Corrosion resistance of the composites Cu-Mo obtained by PVD method,* METAL 2010, Ostrava, Czech Republic, p. 932-937.

VIBRATIONS AND TORQUE MONITORING PROCESSES FOR A COLD ROLLING MILL

Stefan DRAGOMIR, Nicolae DIACONU,
Marian BORDEI
“Dunărea de Jos” University of Galati
email: ddragomir@ugal.ro

ABSTRACT

This paper presents researches made on a system of monitoring and other parallel systems for diagnose used in a cold rolling mill.

The first system (with specific measurement sensors) is an online vibration monitoring system for control (on-line) of the sheet quality and mill maintenance in relation with diagnostic in work for a cold rolling mill machine.

The second system is used for monitoring the torque measuring and mill parameters (force, mill speed, the gap between work roll etc.), part of the integrated process control.

KEYWORDS: cold rolling mill, torque, vibration, quality control, maintenance

1. Introduction

In the new globalizing economical system, the product of cold thin strip (in conditions of the total quality concept) is very important. For obtaining a low cost for the laminated strip it is necessary to increase the productivity of the cold rolling mill by in conditions of diminishing all the losses and using human and material resources at a maximum.

If we make a continuous monitoring of a working cold rolling mill machine we can reduce maintenance costs, increase productivity and improve product quality.

In the context of on-line monitoring for the cold rolling mill process we study the vibration for the most important parts of the cold rolling mill equipment. When in work, the rolling mill, causes severe damage for the mill machine and has a negative influence on the strip quality (Fig. 1).

When we talk about steel strip quality, we take into account the geometrical dimensions and the influences on the strip material due to the rolling mill chatter. Another imperfection or fault can be represented by the marks on the steel strip due to the marks possibly existing on the work rolls.

The integrated control process is undertaken to analyze the vibrations produced on the work roll chocks and backup roll chocks.

The noise and chatter signals are carried out in the time and frequency range. The noise has to be eliminated to obtain reliable strip quality in conformity with predicted dimensions.

In time, we can create a database used for comparison between an initially vibration signal and a vibration work signal for the cold rolling mill machine and finally to archive a quality standard for each laminated roll strip. We created a parallel system of comparison between the initial torque (when the strip is not between the work rolls) and the torque during the rolling process.

The purpose of this study is to find the cause of steel strip faults, to diagnose [1] the state of the mill machine, and to predict when some of its parts can encounter working problems.

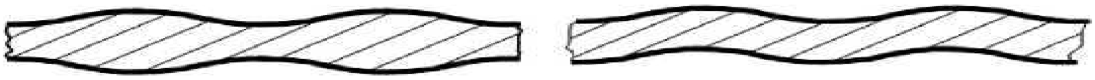

Fig. 1. *Faults of a laminated strip due to rolling mill vibration*

The accuracy of the sheet thickness (texture or surface roughness) is important for the beneficiary of this product.

In working conditions, vibrations or oscillations may occur, which again cause gauge chatter or chatter marks on the rolling sheet.

Gauge chatter are periodical faults in thickness or shape of the strip or regular shades on the surface of the strip transverse to the rolling direction.

Heavy vibrations of the roll stand may even cause ruptures of the strip. The amplitude and wave length of periodical strip faults depend on the vibration system and the vibration frequency.

2. Experimental procedure

2.1. Measurement of vibrations in a cold rolling mill machine

If we take into consideration the incitation system, free vibrations may occur when a single impulse (the rolling stand or parts of it oscillate with their own natural frequency) determines an oscillatory signal in the mill systems.

On the other hand there are excited vibrations in the rolling stands determined by damage that exist in parts of rolling mill machine.

In this context, vertical vibrations exist [2] from the roll stand (1- 16 Hz.), torsion chatter of the main drive (5- 20 Hz.), interspaces chatter or third-octave chatter (100 - 300 Hz.), roll vibration or fifth-octave chatters (500-700 Hz.).

In practice, the differentiations of interfering frequencies into those which are proportional to the speed and those which are not are the first step in describing the phenomenon of vibration and its manifestations. In Figure 1 we see the influence of vibration on the laminated strip on a 5-stand of cold rolling mill machine. The strip pattern is due to the rolls bearing eccentricity and damage of the drive system of the rolling mill machine. Another cause of strip geometry damage is due to displacement of shaft roll gap fluctuation and to excessive free motion.

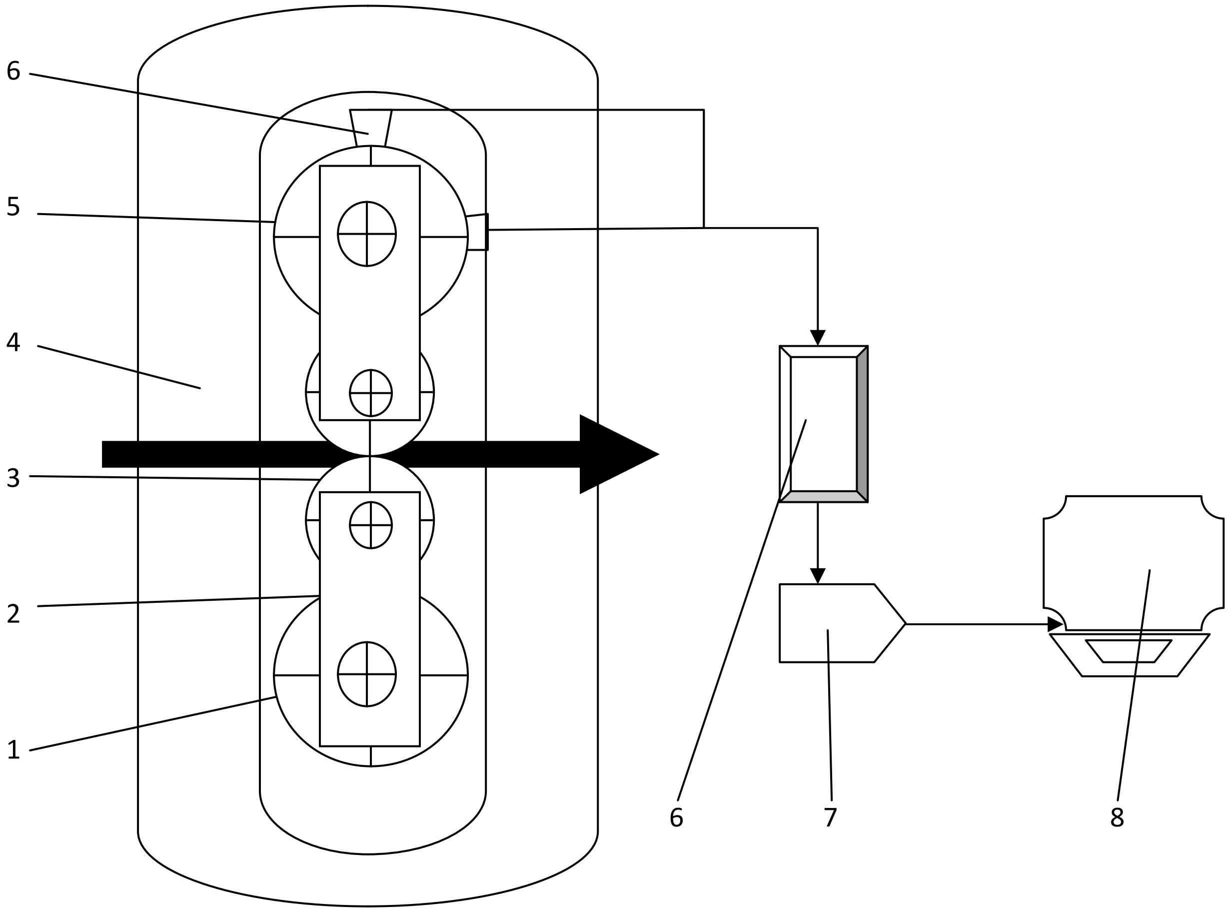

Fig. 2. *Schedule for parameters measured in the cold rolling mill machine: 1-work roll; 2-rolls support; 3-beckup roll; 4-mill stand (frame); 5-horizontal accelerometer; 6-vertical accelerometer; 7-signal preamplifier; 8-process computer*

Experiments were made on the 3, 4, 5 frames of the rolling mill (accelerometers are placed as in Figure 2) because on them there are the highest values of displacements, acceleration and frequency vibrations and that in fact, represents the latest stage in the achievement of the finished product. We use this schedule for automatic online diagnosis of the vibration in the working of a rolling mill machine.

The measurements were performed on 22 rolls, after which the change was made on the working cylinders of five stand of the rolling mill.

The frequency of the vibrations is directly influenced by the speed of rotation of the cylinders, the rolling force, the tension between frames, the emulsion used. The parameters of the vibrations were recorded over the period May - October 2012.

During the measurement campaign there has also been measuring and recording of the functional parameters for the five stand tandem (Table 1.a), the rolling forces, the tensions in the band and the rotation speed of the cylinders - for one of the rolling rolls.

Table 1.a

Frame	1	2	3	4	5
Rolling force, x10^{4}N	1260	1170	1120	1070	1025
Rotation speed of the working cylinders, rot/min	380	475	560	650	780
Tension between the frames, x10^4	1-2 48	2-3 37	3-4 21	4-5 14	

The rolled material was a strip of 12 Ust having [3]: 1.88 mm nominal thickness (entrance in tandem); 0.362-0.408 mm (output of tandem), chemical composition and mechanical characteristics as shown in Table 1.b.

Table 1.b

<table>
<tr><th colspan="6">Chemical composition, [%]</th></tr>
<tr><th>C</th><th>Mn</th><th>P$_{max}$</th><th>Si$_{max}$</th><th>S$_{max}$</th><th>Al</th></tr>
<tr><td>0.12</td><td>0.44</td><td>0.033</td><td>0.052</td><td>0.042</td><td>min 0.016</td></tr>
<tr><th colspan="6">Mechanical properties</th></tr>
<tr><th colspan="2">R$_m$</th><th colspan="2">Flow’s limit R$_{p0.2}$</th><th colspan="2">A$_5$</th></tr>
<tr><td colspan="4">[N/mm^2]</td><td colspan="2">[%]</td></tr>
<tr><td colspan="2">244</td><td colspan="2">275-375</td><td colspan="2">35%</td></tr>
</table>

2.2. Type, location and recording of variables

In the following stage, we made another set of measurements regarding the vibration amplitude, accelerations, frequency spectrum in stands 3, 4 and 5 of the tandem rolling mill. The measurements were made on the support of lower and upper cylinders, on the operator side and on the drive system.

The measurements were made with transducers placed on cylinders bearings support of lower and upper work cylinders in horizontal and vertical position.

After the working parameters analysis we observed the greatest value for tension, force, speed, acceleration recorded at the 3, 4, 5 stands of the rolling mill (Table 1a)

For frame number 4, the measurement values recorded are presented in the subsections below:

a. Measurement of stand displacement

The maximum displacement measured on the cylinder back-up upper support (operator-action) was 355x10^{-6} m, 370x10^{-6}m.

The maximum displacement measured on the lower support of the cylinder (operator-action) emphasized lower values, meaning 36x10^{-6}m and 178x10^{-6}m.

By comparing these data, it will be noticed that the highest value of the movements was on the upper support of the cylinder (drive side). This is due, perhaps, to the existence of some vibrations coming from the chain of cinematic shareholders.

b. Measured and recorded of accelerations

The measured and recorded maximum of acceleration was about 4m/s^2, at the drive side, and about 3m/s^2, at the operator side.

c. Measured and Recorded Frequencies

The frequency spectrum (operator) is presented for the block of lower and upper cylinders, and the graphs of the frequency spectrum for the block of upper cylinders with values ranging 100-300Hz.

They made the same kind of measurements, namely: displacement, acceleration and frequency (on the upper and lower support of the cylinders - the side of shareholders and operator.

d. Accelerations measured in stand number 3

The maximum value was about $2 m/s^2$, which represents about 50% of the acceleration value in the stand number 4.

e. Accelerations measured in stand number 5

The maximum recorded acceleration was about $2.5 m/s^2$ so it is situated between maximum values from stand number three ($1.6 m/s^{2)}$ and stand number four ($4 m/s^2$).

3. Results and discussions

Monitoring of the vibration system may reduce the risk of gage or roll chatter and help to obtain quality products. Secondly, the torque monitoring is necessary for the optimization of the milling process and condition-based maintenance.

After measurements and records made, it resulted that:

-the highest vibration amplitude has been identified in the 4 rolling mill frame (action side), compared with frames 3 and 5;

-accelerations and frequencies had the greatest values at action sides, for all three frames (3, 4, 5);

-the vibrations caused the appearance of some wavy parts on the band surface (rolls 14 and 16; thickness output 0.37; width 1660mm), in the shape of cross stripe, with up to 20-40 mm;

-on the surface of the last 5 rolls strip, before the change of the working cylinders, there could be observed traces and printings belonging to these cylinders.

Analyzing the spectra frequency related to 3, 4, and 5 stands of the rolling mill machine, two maxima were noticed, respectively:

-frequency in range of 100-300 Hz **-** generally speaking, characteristics for spent camps and games of positioning system interspaces, for the quality of surface decks working cylinders, for lubricant but not the last for variations of cylinders rotation speed;

-frequency in range of 500-800 Hz - may generally show a wear stressed of decks of the cylinder support, of their camps (with games in the camps).

Areas of graphs frequency – related to the 500-800Hz range - in particular, the value of the vibration magnitude compared to the area relating to the range 100-300 Hz.

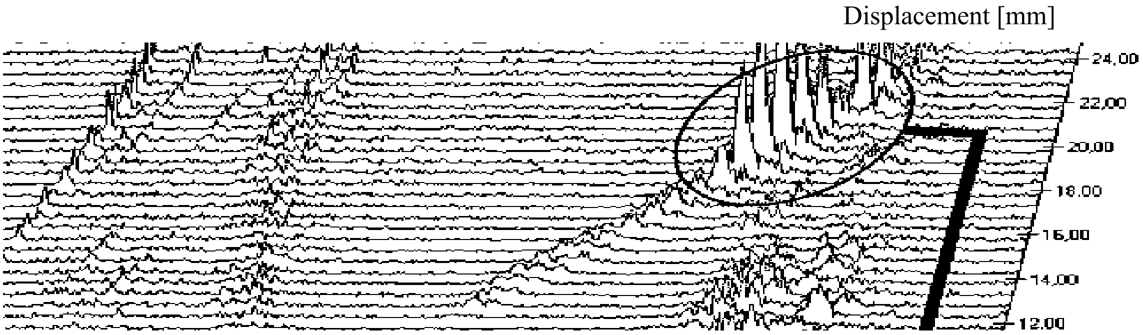

Fig. 3. *Vibration recorded at the drive side (marked with a black line) and at the operator side (left side) [4].*

We can conclude that surface defects occur due to some reasons presented up to a point but also in correlation with the state of wear of the rolling mill in general, the working cylinders, the camps etc.

During a temporary measurement the vibration initiating roll stand had to be identified. The results of the analysis showed that stand number 5 initially caused the gage chatter. The vibrations propagate via the strip to stand 4 and from there to stand 3 (identical constructions). The vibration showed a frequency of roughly 125Hz.

Finding the speed-proportional excitations is of crucial importance, as they allow the detection of the original, mechanical causes of the excitations.

However, the analysis of cumulative [4] spectrum is often time consuming as the excitation effects depend on many strip parameters (material, width, thickness etc.), and thus do not appear during each pass. It has been developed to simplify the evaluation of the spectra to compared to the cumulative spectrum, the benefits of the frequency-speed-collective are the greater time basis and a balanced distribution in the cinematic of the mill.

At rolling speeds between 600-1250m/min., and vibration frequencies not exceeding 450Hz, we have not registered print and sudden wave variations in the thickness of the rolling strip.

At vibration frequencies between 450 and 1150Hz, we noticed wave surface bands with 2-20mm step pronounced wear in the work and back-up rolls support.

Following the experiments carried out during 2011, for a number of rolls rolled over in 250 rolls strip, consisting mainly in measurement and analysis of the vibrations, the following range of common characteristics were established: vibrations in the range of frequencies 5-90Hz corresponding for gearing, gear box.

Vibrations with frequencies of 125-300Hz, corresponding to games in interspaces of positioning system, for wears in the work and support of rolls bearings and because of the lubricant used.

Vibration frequencies in the range of 500-980Hz related to wears in the drive system (work and back-up rolls support, motor-couplings bare-coupling, some types of wave on strip surface, emulsion used etc.). The vibrations are caused by the torsion occurring in the middle of the pass and determine a lot of marks on the strip surface and causing severe damage to the drive system.

A process work parameters optimization may be carried out if such events are recorded and analyzed. In this case, the lubrication system was improved. During the first pass the entering torque impact is very high.

The paper discussed two types of quality and maintenance-related monitoring systems for rolling mills [5].

Experiments in tandem operation revealed: the growing tendency in vibration amplitude at high speed lamination where the rolling speed is increased with about 50% per rolling mills, registered a magnitude vibrations that increased about 35% per frame of rolling mill.

On the other hand, the band widths with narrow and heavy sea manifest the same tendency of increasing amplitude vibrations, unlike bands with great width and thickness, where the effect of damping vibrations is considerably higher [7].

The torque sensors used in rolling mills must be very robust due to the rough ambient conditions.

Although this material represents only a small percentage of the yearly overall production at this mill stand, the arising torque loads damages components of the universal joint at a roughly ten times higher percentage in terms of residual lifetime.

The practical examples presented here on the monitoring systems confirm their efficiency.

For the cold rolling mill tandem - 1700 mm – after measurement of dynamic couples, we observed values exceeding the dynamic torque, when calculated with about 17% at stands I, II, and approx. 23.5% at stands III, IV and V. These differences are based on the following: the shock due to the clamp lane between rollers; games due to components usage chain training, inadequate emulsion; games related positioning system; the usage of the decks cylinders.

Of all the research results obtained, the current problem is to analyze the conditions for a scientific running of the rolling mills, the identification and quantification disturbing factors and, finally, the modern design, for increasing resistance, reliability, reduce consumption, ensure continuity processes and final quality products.

All this led to the development of a general concept for the establishment of dynamic influences on complex machinery and quantification of the dynamic forces [8].

The modern analysis of the tensions leads to the design with a minimum of approximation and uncertainty of sub-assemblies of equipment.

4. Conclusions

A major conclusion of the investigation on the basis of which some research contracts were concluded with ARCELOR MITTAL S.A. is a pressing need for reduction and possible elimination of vibrations in order to increase the reliability of all the rolling mills and the production of rolling strip in accordance with international standards.

If we do not take into account the effect of internal and external loaded (dynamic forces of inertia in starting and braking periods, games in components from inside the spaces of the cinematic drive system, wear subassemblies), severe repercussions will appear concerning the reliability and quality of the production process.

Under the action of variable loads (charging the forces and resistance on the mill parts), the materials of these parts suffer from damage and in time the phenomenon of fatigue is installing. This is the most frequent cause for the deterioration of equipment subassemblies.

Dynamic effects for the tandem studied permit to appreciate that the most important dynamic effects occur in the mill in tandem, in the positioning system, in drive system (motor-couplings bare-coupling, emulsions etc.)

We can take measures to reduce the load in the design stage of the rolling mill machine and the design of the cinematic and constructive schedules, correlated with the drive system. It is important to determine the size of dynamic moments that may occur during operations.

We must know the real physical processes that occur in the equipment, taking into consideration the parts mass distribution, the game inside of the drive system and electrical characteristics.

We use computer modeling to determine, simulation of cinematic and dynamic parameters and to optimization the drive system.

It is necessary to develop models that combine aspects of dynamic mechanical and electrical systems and through computer simulation to provide functionality and efficiency as well as deficiencies in work.

References

[1]. N. Portman - *Applications of neural networks in rolling mill automation*, Iron and Steel Eng., vol.72, no.2, pp.33-36. (1995).

[2]. Asch, A., Hohn, W. - *Monitoring System for Roll Stand Drives using Strain Gage Technology*. Proceedings of the 9th IF AC Symposium on Automation in Mining, Mineral and Metal Processing, pg 175 - 180, /ASC98/ IF AC International Federation of Automatic Control (1998).

[3]. Tamara Radu, Florentina Potecasu, Maria Vlad - *Researchon obtainingand characterization of zinc micro-alloyed with bismuth coatings,* Metalurgia International nr. 1/2011 ISSN 1582-2214, pag. 44-48.

[4]. Donkle H. I., L. - *Fifth octave chatter problem solved using vibration analysis,* AISE Steel Technology, Volume 76 No. 11 (1999). /LOU99.

[5]. Mackel, A., Cerv, H. KeBler, H.-W., Luckmann, F. - Mill Diagnostic System (Mi-DaS) - a monitoring system with quality- and maintenance-related diagnostic functions, Aluminium, pg 137. Volume 74 /MAC98/ (1998).

[6]. Mackel, J., Asch, A., Seeliger, A. – *Brummerschwingungenan Walzgeriistenvol-lkontinuierlicherKaltwalzanlagen*, Detektierung, Verifikation, Vermeidung./ MAC95/ VDI-BerichteNummer pg.1220 (1995).

[7]. Mackel, J., Seeliger, A. – Qualitatssicherun ganschnelllaufenden Walzanlagen. Pg. 187, Alma Mater Aquensis MAC96/RWTH-Aachen (1995/96).

[8]. Mackel, J., Seeliger, A., Georges, D. - *Measurement and Diagnosis of Process*-Disturbing Oscillations on Plants for Machine Condition Monitoring and Quality Control. Pg. 98. In: Proceedings of the XIV Imeko World Congress (1997)/ MAC97.

THE ANNALS OF “DUNAREA DE JOS” UNIVERSITY OF GALATI.
FASCICLE IX. METALLURGY AND MATERIALS SCIENCE
N^0. 1 – 2012, ISSN 1453 – 083X

INFLUENCE OF NORMAL LOADS ON CORROSION BEHAVIOUR OF Ti-6Al-4V ALLOY DURING FRETTING IN ARTIFICIAL SALIVA

Eliza MARDARE[1], **Lidia BENEA**[1,*], **Jean-Pierre CELIS**[2]
[1]Dunarea de Jos University of Galati, Metallurgy, Materials Science and Environment Faculty,
Competences Center: Interfaces-Tribocorrosion-Electrochemical Systems, Galati, Romania
[2]Katholieke Universiteit Leuven, Dept. MTM, B-3001 Leuven, Belgium
[*]Corresponding author: Lidia.Benea@ugal.ro

ABSTRACT

The fretting corrosion behaviour of untreated Ti-6Al-4V alloy in artificial saliva solution was evaluated based on the change in open circuit potential (OCP) measured as a function of time. Fretting corrosion experiments were performed using a unidirectional reciprocating fretting experimental set-up which was mechanically and electrochemically instrumented, under various solicitation conditions. The effect of applied normal force on corrosion-wear of the tested material was determined. Before the onset of fretting a large increase of the OCP in the noble direction for the Ti-6Al-4V alloy was observed. With the onset of fretting it was observed a cathodic shift in OCP, shift which decreases linearly with increasing normal load. The restoration ability of Ti-6Al-4V alloy after the passive films damaged during fretting was observed after the fretting motion ceased. It was confirmed a decrease in friction coefficient with gradually increasing load. The morphological features of the fretted zone and the wear mechanism were assessed using scanning electron microscopy and non-contact optical profilometer.

KEYWORDS: implant application, fretting corrosion, wear, electrochemistry, Ti-6Al-4V alloy

1. Introduction

Pure Ti and Ti-6Al-4V are mainly used for biomedical applications and satisfy most of the demand for implant materials in the medical and dental fields [1-2]. The increasing use of Ti-based metals for implantation is due to high strength, low density, high specific strength, good resistance to corrosion, enhanced biocompatibility, moderate elastic modulus compared to other metallic biomaterials [2].

Titanium based metals derive theirs resistance to corrosion from formation of an adhesive TiO_2 oxide layer at the surface to a depth of approximately 5 nm [3-7]. As long as oxygen is present, the spontaneous formation of a titanium oxide film on their surface leads to an extremely stable film and gives a passivating effect to the metal.

The passivation effect does not by itself mean that the metal will not corrode but the percentage of corrosion is much lower in the presence of a stable oxide layer [8]. This high corrosion resistance of titanium alloys can be strongly decreased by damage of the passive film when a mechanical stress is loaded on the sample [3].

There are very few studies in literature which use artificial saliva as test solution in the fretting corrosion behaviour of Ti-6Al-4V, compared with other simulated body fluids (Hank solution, Ringer solution, sodium chloride solution) [9-13].

Moreover the combination of mechanical parameters used in the present research such as load, frequency, displacement amplitude and number of cycles, is different compared to the same studies mentioned above [9-13].

The aim of this research is to investigate the wear and corrosion behaviour as a function of normal load of Ti-6Al-4V alloy in artificial saliva solution.

2. Experimental procedure

2.1. Materials

Annealed grade 5 Ti-6Al-4V alloy, according to the international standard ISO 5832-3, with mechanical properties in accordance with ASTM B265 and whose chemical composition and mechanical properties are presented in Table 1 was used as base material. The samples of Ti-6Al-4V used, in the form of plates, were cut to dimensions of 25 x 25 x 2 mm and then successively polished with waterproof abrasive paper with grit (320 - 4000 µm), diamond paste (3 and 1 µm size) and colloidal silica solution (0.04 µm size of particles), finally achieving a mirror surface. Samples were cleaned in an ultrasonic ethanol bath during 5 minutes and dried using dry, cold air. Then the samples were stored for about 24 hours in a desiccator to allow the formation of a stable surface film on the test samples.

Al_2O_3 balls (G 10 grade) with 10 mm diameter (Ceratec Technical Ceramics BV) were used as counterpart in the sliding tests. The electrolyte utilized in fretting corrosion tests was Fusayama - Mayer artificial saliva [14-15], with the chemical composition presented in Table 2 and having a pH equal to 5. Tests were performed at room temperature (23^{o}C).

Table 2. *Chemical composition of test electrolyte*

Compounds	**Saliva Fusayama - Mayer** [g/L]
NaCl	0.4
KCl	0.4
$CaCl_2*2H_2O$	0.8
NaH_2PO_4	0.69
Urea	1

2.2. Fretting-corrosion tests

Fretting-corrosion tests were performed using a uni-directional reciprocating tribometer shown schematically in Fig. 1.

Ti-6Al-4V alloy samples serve as working electrode and their potential was controlled using Solartron Instruments 1287 Electrochemical Interface potentiostat/ galvanostat with a frequency response analyzer SI 1255. The counter electrode was made of platinum wire and the reference electrode was the Ag/AgCl (saturated KCl solution, E=200mV vs. NHE). These electrodes were placed in the fretting corrosion cell in such a way that only 1 cm^2 area of the working electrode was exposed to the electrolyte. During the tribocorrosion test, the normal force, tangential force, coefficient of friction, number of cycles as well as the electrochemical parameter, were monitored.

The wear tests were carried out with 1, 2 and 5 N normal forces, at 1 Hz reciprocating frequency, with a displacement amplitude 200 µm and 1000 cycles.

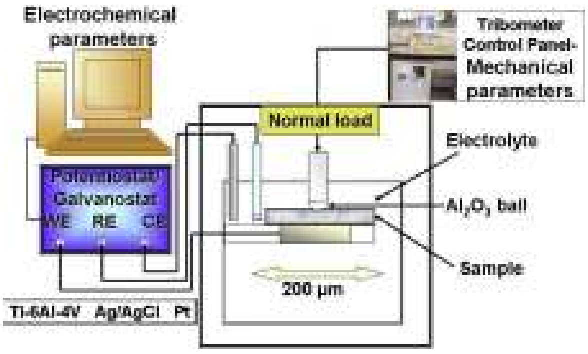

Fig. 1. *Schematic view of the experimental set up for fretting-corrosion tests*

The protocol used for the tribocorrosion tests consisted of two steps: (1) measuring the open circuit potential (OCP) of the sample by immersion for 60 minutes to allow stabilization of potential and (2) fretting test during which OCP was measured.

2.3. Characterization techniques

The surface topography and mass loss of the volume removed from the surface in the wear track were determined by measurements using non contact Wyco NT3300 optical profilometer with white light interferometry and Vision (version 2.210) software. Philips scanning electron microscope XL 30 FEG was used to characterize the morphological features of the fretted zone.

Table 1. *Chemical composition and mechanical properties of Ti-6Al-4V alloy*

Chemical composition									
Specification	**8-12-05832-1**	**N**	**Al**	**C**	**V**	**H**	**Fe**	**O**	**Ti**
Ti-6Al-4V	max. [%]	0.003	6.01	0.008	3.83	0.002	0.083	0.088	89.976
Grade 5	min. [%]	0.003	5.86	0.008	3.73	0.002	0.068	0.084	90.245

Mechanical properties		
Resistance to flow	**Tensile strength**	**Elongation**
[MPa]		[%]
865	937	11

3. Results and discussions

3.1. Evolution of open circuit potential under static conditions

Prior to starting the fretting-corrosion tests, the Ti-6Al-4V alloy was allowed to stabilize in artificial saliva for 60 minutes. In this interval, a large increase of the OCP in the noble direction for the Ti-6Al-4V samples was observed, fact which indicates that a stable passive film grows on the surface (Fig. 2).

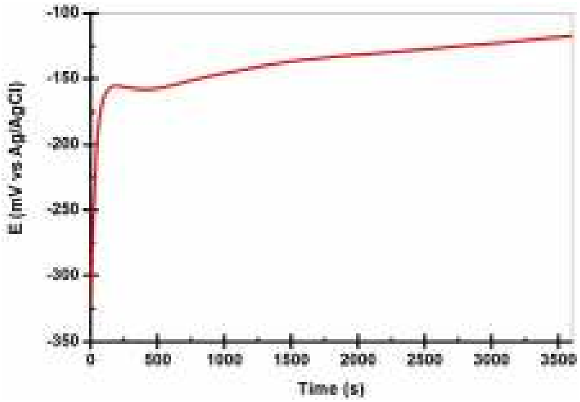

Fig. 2. *OCP evolution of Ti-6Al-4V alloy measured during 60 minutes of immersion*

3.2. Effect of normal force on open circuit potential measurement

After the period of 60 min. when OCP exhibits an anodic shift (from -322 to -117 mV vs. Ag/AgCl) were monitored the effects of normal force on OCP evolution before, during and after sliding wear test, tracked on Ti-6Al-4V samples. These tests were performed at three different normal forces of 1, 2 and 5 N, fretting frequencies of 1 Hz, with a displacement amplitude of 200 µm and finally at 1000 number of cycles.

In Fig. 3 there are shown OCP variations of the Ti-6Al-4V alloy immersed in artificial saliva solutions before (3 min.), during (1000 cycles) and after (10 min.) fretting tests at a 1 Hz frequency with a displacement amplitude of 200 µm, for 1000 cycles, by applying the normal forces mentioned above.

For all tests performed it was observed that with the onset of fretting a sudden decrease of the OCP occurs. This potential shift is associated with the damage of passive film by partial or complete removal of its [10, 16]. In the period of friction were reported some oscillations in the OCP for Ti-6Al-4V alloy and this is attributed to the periodic removal caused by the contact with counter body (depassivation) and growth caused by contact with the electrolyte (repassivation) of the passive film in the fretted zone [17-18].

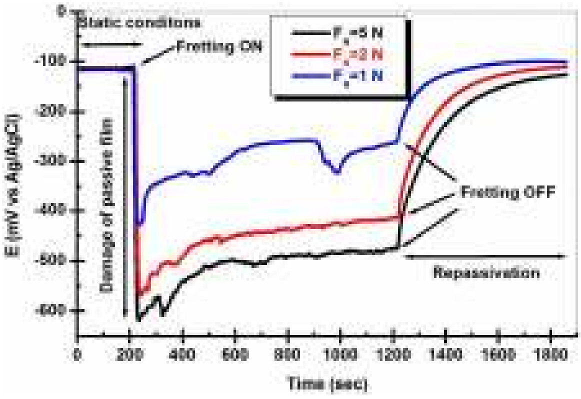

Fig. 3. *OCP variation of Ti-6Al-4V alloy measured vs. time before, during and after loading at 1 N, 2 N and 5 N.*

After unloading, the OCP of Ti-6Al-4V samples shows an anodic shift due to repassivation of Ti-6Al-4V substrate forming immediately a thin film of titanium oxide [10, 16-18].

In conclusion, from Fig. 3 it is observed that the potential measured during the fretting-corrosion tests decreases linearly with increasing normal load.

3.3. Effect of normal force on the friction coefficient evolution

The effect of imposed normal loads (1, 2 and 5 N) on the evolution of friction coefficient for the Ti-6Al-4V alloy at a 1 Hz fretting velocity at with a displacement amplitude of 200 µm, for 1000 cycles, in artificial saliva is observed in Fig. 4.

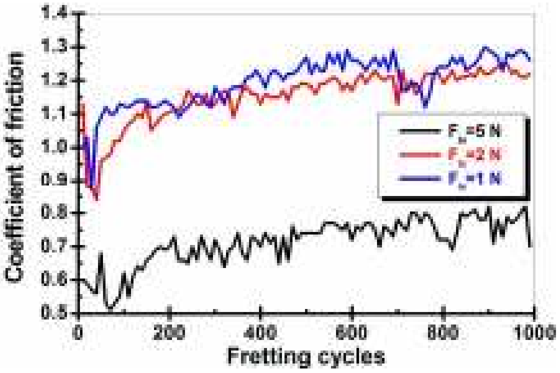

Fig. 4. *The influence of normal loads (1 N, 2 N, 5 N) on the evolution of friction coefficient*

This figure reveals a decrease in the coefficient of friction with increasing normal force at constant frequency and constant number of cycles, due to smoothening of the surface under high load, similar observations which were made by F. Ahmad et al. for Aluminium Matrix Composite [19].

By correlation of potential values recorded during friction with coefficient of friction values is observed that the potential drop events are accompanied by a sudden decrease in the coefficient of friction and this behaviour may explain by the delamination of the tribolayers formed in the contact region, similar observations being made by A.C. Vieira et al. [21].

3.4. Characterization of the wear track

3.4.1. Scanning electron microscopy

The secondary electron images of the fretted zone of Ti-6Al-4V alloy, after subjecting it to fretting corrosion in artificial saliva at normal loads of 1, 2 and 5 N, at a 1 Hz fretting velocity of with a displacement amplitude of 200 μm, for 1000 cycles are shown in Fig. 5.

A first observation that can be made at investigation of the wear tracks from Figure 5 is that with the increase of the normal load the dimensions of the wear track also increase. Also, the damage suffered by the sample is directly proportional with the increase of the applied force.

3.4.2. Profilometric measurements

After the tribocorrosion experiments were finished, the total wear of the Ti-6Al-4V sample was evaluated by profilometry. Three dimensional surface profiles of the fretted zone of Ti-6Al-4V alloy are shown in Fig. 6.

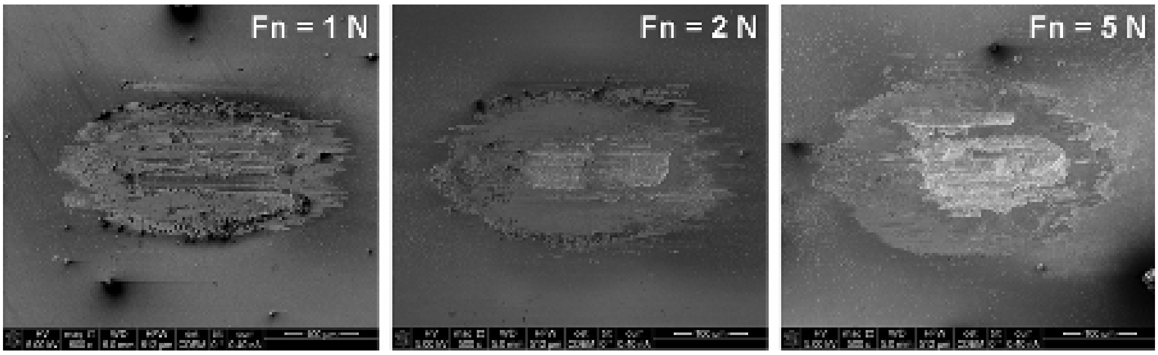

Fig. 5. *SEM images of the entire fretted zone of Ti-6Al-4V after tribocorrosion tests in artificial saliva solution under normal loads of 1, 2, 5 N*

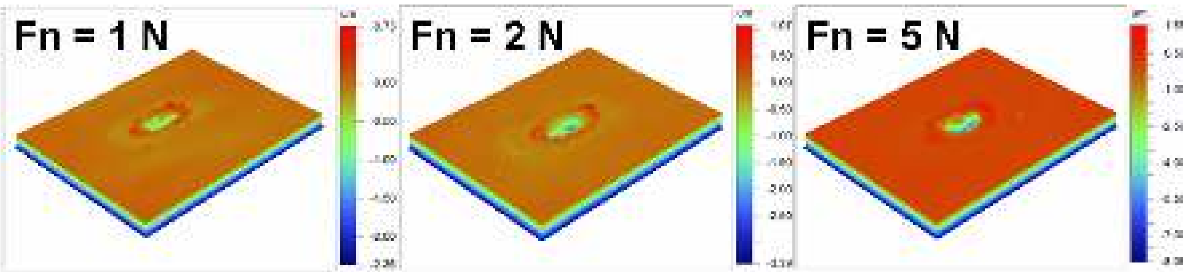

Fig. 6. *3-dimensional profiles of the fretted zone of Ti-6Al-4V alloy after tribocorrosion tests in artificial saliva solution under normal loads of 1, 2, 5 N*

The same trend can be clearly seen as for scanning electron micrographs of the entire fretted zone of Ti-6Al-4V, that with increasing the normal load the dimensions of the wear track also increase.
Also, the irregular surface profile of the wear track in case of higher normal loads points towards the presence of adhered wear debris in the track indicating the abrasive wear mechanism, as it can be seen in Fig. 6.

Once again the fretting-corrosion experiments made on the Ti-6Al-4V alloy in artificial saliva solution have demonstrated that the wear is very pronounced if the normal loads applied are increase.

4. Conclusions

The tribocorrosion behaviour of the titanium alloy Ti-6Al-4V fretting against corundum in artificial saliva solution was investigated in a ball-on-flat contact configuration combined with *in situ* electrochemical measurements (OCP).

According to the evolution of the open circuit potential at immersion for 60 minutes of Ti-6Al-4V alloy in artificial saliva, an increase of the potential in the noble direction was observed, fact which indicates that a stable passive film has grown on the surface. With the onset of fretting was seized a drop in the cathodic domain of OCP, decrease which is linear with the increase of the normal load, due to the removal of the passive oxide layer induced by fretting nd which confirms its increase in susceptibility for corrosion.

The effect of normal force applied on corrosion-wear of the tested material was determined. The applied normal force was found to greatly affect the potential during fretting-corrosion, an increase in the normal force inducing a decrease in potential accelerating the depassivation of the Ti-6Al-4V alloy. Also, depending on the applied normal force, a decrease in coefficient of friction was confirmed, with gradual load increase, due to the smoothening of the surface under high load.

Acknowledgements

The preparation of this paper would not have been possible without the support provided by the Bilateral Research Agreement between Research (Competences) Centre Interfaces – Tribocorrosion and Electrochemical Systems (CC-ITES) from Dunarea de Jos University of Galati and Department of Metallurgy and Materials Engineering (MTM) from Katholieke Universiteit Leuven. The authors express their sincere thanks to technical staff from Department of Metallurgy and Materials Engineering (MTM), Katholieke Universiteit Leuven for giving the permission to do the necessary research work, for the support offered and to use departmental research equipments.

References

[1]. **Mitsuo Niinomi** - D.D.Sc, *Metallic biomaterials*, J Artif Organs 11 (2008) 105-110.

[2]. **Marjan Bahrami Nasab, Mohd Roshdi Hassan** - *Metallic Biomaterials of Knee and Hip - A Review*, Trends Biomater. Artif. Organs, 24(1) (2010) 69-82.

[3]. **M. Masmoudi, M. Assoul, M. Wery, R. Abdelhedi, F. El Halouani, G. Monteil** - *Friction and wear behaviour of cp Ti and Ti6Al4V following nitric acid passivation*, Appl. Surf. Sci. 253 (2006) 2237-2243.

[4]. **R. Chiesa, E. Sandrini, M. Santin, G. Rondelli, A. Cigada** - *Osteointegration of titanium and its alloys by anodic spark deposition and other electrochemical techniques: A review*, J. Appl. Biomater. Biomech. 1 (2003) 91-107.

[5]. **C. Sittig, M. Textor, N.D. Spencer, M. Wieland, P.-H. Vallotton** - *Surface characterization of implant materials c.p. Ti, Ti-6Al-7Nb and Ti-6Al-4V with different pretreatments*, J. Mater. Sci: Mater. Med. 10 (1999) 35-46.

[6]. **C. Fonseca, M.A. Barbosa** - *Corrosion behaviour of titanium in biofluids containing* H_2O_2 *studied by electrochemical impedance spectroscopy*, Corros. Sci. 43 (2001) 547-559.

[7]. **Y. Yang, N. Oh, Y. Liu, W. Chen, S. Oh, M. Appleford, S. Kim, K. Kim, S. Park, J. Bumgardner, W. Haggard, J. Ong** - *Enhancing Osseointegration Using Surface-Modified Titanium Implants*, JOM 58 (2006) 71-76.

[8]. **R. Van Noort** - *Review Titanium: the implant material of today*, Journal of Materials Science 22 (1987) 3801-3811.

[9]. **S. Barril, S. Mischler, D. Landolt** - *Electrochemical effects on the fretting corrosion behaviour of Ti6Al4V in 0.9% sodium chloride solution*, Wear 259 (2005) 282-291.

[10]. **B. Sivakumar, Satendra Kumar, T.S.N. Sankara Narayanan** - *Fretting corrosion behaviour of Ti-6Al-4V alloy in artificial saliva containing varying concentrations of fluoride ions*, Wear 270 (2011) 317-324.

[11]. **É. Martin, M. Azzi, G.A. Salishchev, J. Szpunar** - *Influence of microstructure and texture on the corrosion and tribocorrosion behavior of Ti-6Al-4V*, Tribology International 43 (2010) 918-924.

[12]. **J. Komotori, N. Hisamori, Y. Ohmori** - *The corrosion/wear mechanisms of Ti-6Al-4V alloy for different scratching rates*, Wear 263 (2007) 412-418.

[13]. **S. Hiromoto, S. Mischler** - *The influence of proteins on the fretting-corrosion behaviour of a Ti6Al4V alloy*, Wear 261 (2006) 1002-1011.

[14]. **B. Grosgogeat, L. Reclaru, M. Lissac, F. Dalard** - *Measurement and evaluation of galvanic corrosion between titanium/Ti6Al4V implants and dental alloys by electrochemical techniques and auger spectrometry*, Biomaterials 20 (1999) 933-941.

[15]. **N. Ibriş, J.C. Mirza Rosca** - *EIS study of Ti and its alloys in biological media*, Journal of Electroanalytical Chemistry 526 (2002) 53-62.

[16]. **P. Ponthiaux, F. Wenger, D. Drees, J.P. Celis** - *Electrochemical techniques for studying tribocorrosion processes*, Wear 256 (2004) 459-468.

[17]. **S. Kumar, T.S.N.Sankara Narayanan, S.G. Sundara Raman, S.K. Seshadri** - *Evaluation of fretting corrosion behaviour of CP-Ti for orthopaedic implant applications*, Tribology International 43 (2010) 1245-1252.

[18]. **A. Berradja, F. Bratu, L. Benea, G. Willems, J.P. Celis** - *Effect of sliding wear on tribocorrosion behaviour of stainless steels in a Ringer’s solution*, Wear 261 (2006) 987-993.

[19]. **F. Ahmad, M. Rafi Raza, A. Majdi Ab. Rani, S.H. Jason Lo** - *Wear Properties of Alumina Particles Reinforced Aluminium Alloy Matrix Composite*, J. Appl. Sci. 11 (2011) 1673-1677.

[20]. **C. Navas, I. García, Xingpu Ye, J. de Damborenea, J.P. Celis** - *Role of contact frequency on the wear rate of steel in discontinuous sliding contact conditions*, Wear 260 (2006) 1096-1103.

[21]. **A.C. Vieira, A.R. Ribeiro, L.A. Rocha, J.P. Celis** - *Influence of pH and corrosion inhibitors on the tribocorrosion of titanium in artificial saliva*, Wear 261 (2006) 994-1001.

THE ANNALS OF “DUNAREA DE JOS” UNIVERSITY OF GALATI.
FASCICLE IX. METALLURGY AND MATERIALS SCIENCE
N^0. 1 – 2012, ISSN 1453 – 083X

SELECTIVE GROWTH OF 1D NANOSTRUCTURED OXIDE MATERIALS USING PDMS STAMP

Anca-Ionela DANCIU[1], **Viorica MUSAT**[1*], **Tito BUSANI**[2], **Alexandra GONÇALVES**[2], **Joana V. PINTO**[2], **Mafalda COSTA**[2], **Iwona BERNACKA-WOJCIK**[2], **Rodrigo MARTINS**[2] **and Elvira FORTUNATO**[2]
[1]Centre of Nanostructures and Functional Materials-CNMF, "Dunărea de Jos" University of Galați, Romania
[2]Materials Science Department, CENIMAT/I3N, FCT-UNL, Campus de Caparica, 2829-516 Caparica, Portugal
*email: viorica.musat@ugal.ro

ABSTRACT

The approach for selective growth of 1D nanostructured oxide materials using poly (dimethylsiloxane) (PDMS) stamp consists of using microcontact printing, as such the soft lithography technique, for transferring the pattern of ZnO film on a substrate, followed by the hydrothermal growth of 1D nanowires on patterned areas. The nanowires have been grown in aqueous solutions of zinc nitrate at temperature at 95°C. The wettability of the glass and of the Si/SiO$_2$ *substrates was investigated by contact angle measurements. The morphology of the nanostructures obtained was characterized by optical microscopy and scanning electron micoscopy.*

KEYWORDS: ZnO nanowires, hydrothermal growth, microcontact printing, contact angle, morphology

1. Introduction

One-dimensional ZnO nanostructures (nanowires) have been studied intensively for the realization of various devices, such as light-emitting diodes [1], gas sensors [2], ultraviolet photosensor [3] and field effect transistors [4], due to their simple synthesis route.

Achieving selective, uniform and ordered arrays of ZnO 1D nanostructures on wanted areas of substrates via a one-step approach by the wet solution method remains a prominent challenge. For the selective pattern growth of ZnO nanowires various technologies have been developed: nanosphere litography [5], silane-based self-assembled monolayers [6], electron beam lithography [7] and conventional photolitography [8]. These procedures are time-consuming and require some expensive facilities. The new soft lithography techniques, such as microcontact printing, represent a very attractive alternative a nonphotolitographic strategy, using an element with surface relief (i.e. the stamp) to transfer material to a preselected area of the substrate [9-11]. Usually, stamps are produced by replication against a master that has the desired relief features.

A conventional PDMS stamp has a hydrophobic surface which enables nonpolar chemicals to be transferred onto substrates [12]. In this article, we report a selective growth of 1D nanostructures that combines the direct patterning of ZnO films via microcontact printing (1) and subsequent low-temperature hydrothermal growth of ZnO nanowires (2).

2. Experimental details

2.1. Preparation of Elastomeric Polymer Stamp

For the preparation of the elastomeric polymer stamp, a SU-8 photoresist was spin-coated onto the Si wafer and then exposed at 14.1mW UV radiation, through a photomask with 300x300 and 700x700 µm square model.

The exposed SU-8 thin film was developed to yield the pattern (master mold) and then cleaned with isopropyl alcohol and deionized (DI) water.

An polymer, PDMS (Sylgard 184 Silicone Elastomer KIT, Dow Corning)[13], fabricated by pouring a mixture of silicone elastomer and a curing agent, was poured onto the SU-8 mold and cured at 70°C.

After the curing process, the PDMS was detached and cleaned in ethanol and ultrapure water, and treated with O_2 plasma (***Figure 1a***).

2.2 Patterning of ZnO film and growth of ZnO nanowires

For the deposition of the ZnO film, an alcoholic solution of zinc acetate dihydrate, $Zn(CH_3COO)_2{\cdot}H_2O$, (Sigma Aldrich, 99.5% purity) was used. The solution for the hydrothermal growth of nanowires, zinc nitrate hexahydrate ($Zn(NO_3)_2{\cdot}6H_2O$, 98% Sigma–Aldrich) was used as row material. Zinc nitrate salts provide Zn^{2-} ions required for building up ZnO nanowires, while water molecules in the solution provide O^{2-} ions. HMTA hydrolyze in the water solution and gradually release OH^- (***Figure 1b***).

2.3 Characterization of thin film and nanowire layers

The contact angle measurements were processed at 24°C with goniometer – *OCA 15 plus DataPhysics*, *Germany*. The surface morphology of patterned substrates was investigated by optical microscopy using a Olympus BX51 microscope. The effect of the morphology of the nanowires grown on patterned layers was investigated by scanning electron microscopy using an Zeiss Auriga microscope.

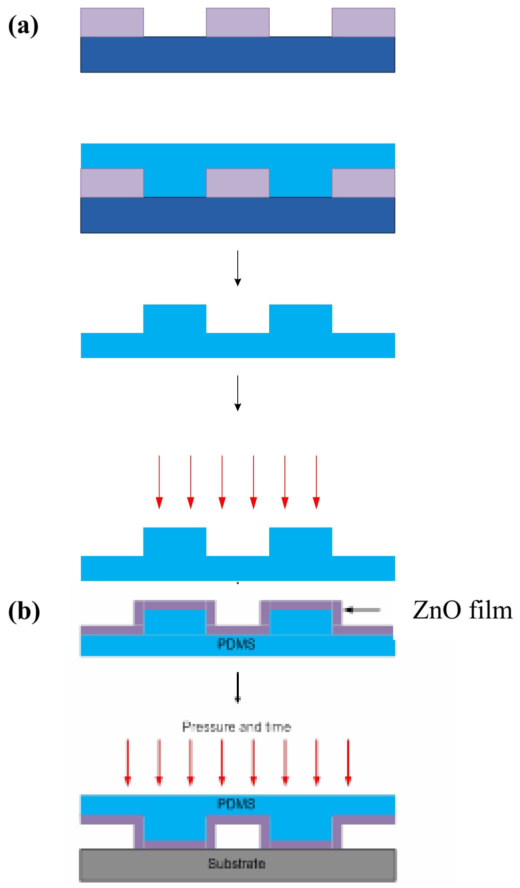

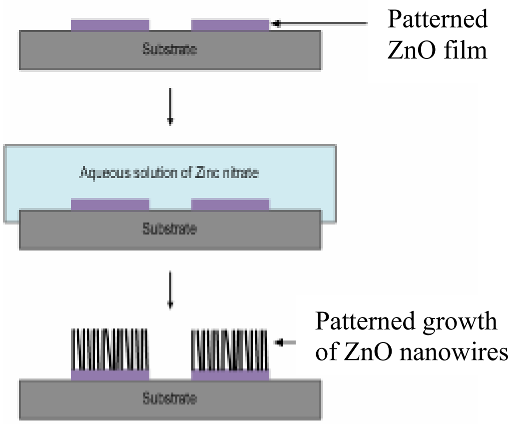

Fig. 1. *Cross illustration of the selective growth process: Elastomeric stamp preparation (a); Pattering of ZnO film and selective growth of ZnO nanowires (b)*

3. Results

Figure 2 shows the contact angle variation when measured on glass and silicon substrates. Using this technique, the wettability, in relation to zinc acetate solution used for the patterning of the ZnO film, was investigated.

The contact angle values show significant variation, it increasing from 37 to 92° for glass substrate, and from 52 to 100° for Si/SiO_2 substrate, when the substrates are pattern with ZnO seeds layer. Taking into consideration these results, one can conclude that the wettability of the glass substrate is higher than that of the silicon substrate, which implies a higher adhesion of zinc acetate dihydrate solution to the glass substrate.

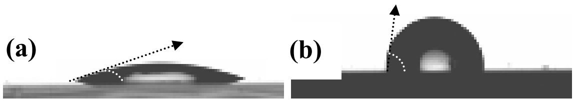

Fig. 2. *Illustration of contact angle variation on glass substrate (a) and silicon substrate (b)seeded with ZnO layer*

The model size and roughness have a significant effect on the quality of the resulted film pattern and on the aspect of the grown nanowires.

To control the geometry of patterned areas, the size of the square models of PDMS stamp was modified from 300x300 to 700x700 µm and the pressure carrying stamping was kept constant.

The optical images of the patterned substrates with different size of model are shown in ***Figure 3.*** The smoothest pattern surface was obtained for the 500x500 µm size.

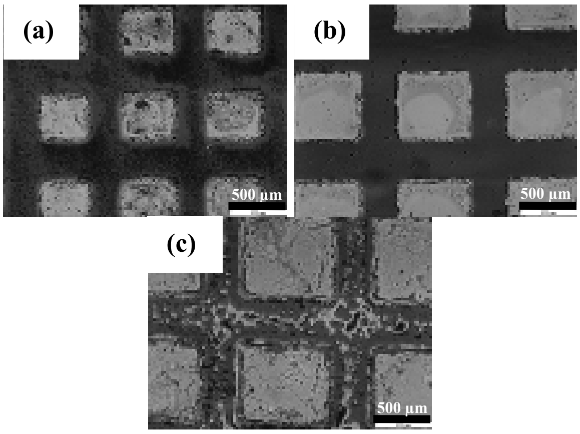

Fig. 3. *Optical images of Si/SiO$_2$ substrates stamped with PDMS stamp with dimension models 300x300 (a), 500x500 (b) and 700x700 µm (c)*

From the optical images, one can observe that the size model can affect the quality of the patterned areas. The square shape present a number of irregularities, but the advantage is that a very smooth surface will always be obtained so it will not affect the morphology of the 1D ZnO nanostructures.

In ***Figure 4*** are shown the SEM images of a Si/SiO$_2$ substrate stamped with a square model (right part) and non-stamped (left part). The patterned area obtained by microcontact printing shows some irregularities but very dense vertical nanowires grown inside of the square pattern can be observed (Figure 4c).

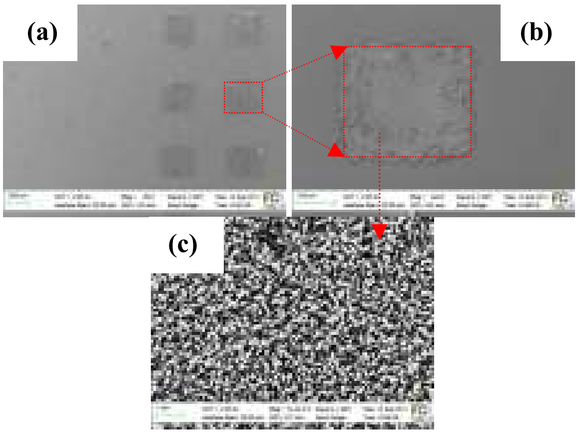

Fig. 4. *SEM images of ZnO nanowires localized grown on Si/SiO$_2$ patterned substrate (square model) by microcontact printing: images with non patterned and patterned zones (a), detail with patterned square model (b), detail with nanowires grown on patterned zones (c)*

The influence of the nature of the substrate on the stamping process is presented in ***Figure 5.***

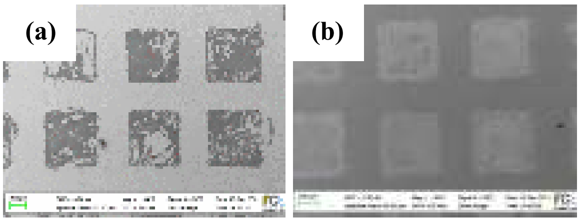

Fig. 5. *ZnO nanowires grown on glass substrate (a) and silicon substrate (b) patterned by microcontact printing*

It was mentioned before that the adhesion of the Zn $(O_2CCH_3)_2$ based stamping solution onto the silicon substrate is higher compared to that on the glass substrate.

On Si/SiO$_2$ substrates, the patterned areas are well shaped and defined, and the grown nanowires are dense and vertical; the edge of the model on the Si/SiO$_2$ substrate is more uniform than on the glass substrate. So, the quality of the created model is influences by the nature of the substrate, and in turn influence the direction and dispersion of the grown nanowires. In order to explore the relationship between the precursor concentration and the density of the ZnO nanowires arrays, the precursor concentration was varied between 0.01 - 0.025 M. As shown in ***Figure 6,*** the dimensions and the density of ZnO nanowires increase with solution concentration.

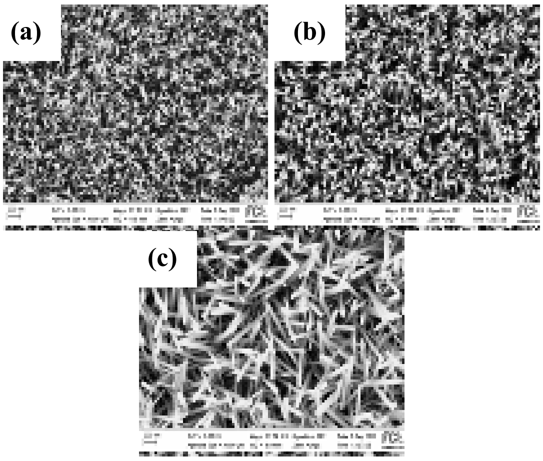

Fig. 6. *SEM images with ZnO nanowires growth with different concentrations of solution: 0.01 M (a); 0.02 M (b); 0.025 M (c)*

From ***Figure 7*** one can clearly see that, with increasing solution concentration, the nanowire length range from 323 to 667 nm, and diameters ranges from 12 to 29 nm.

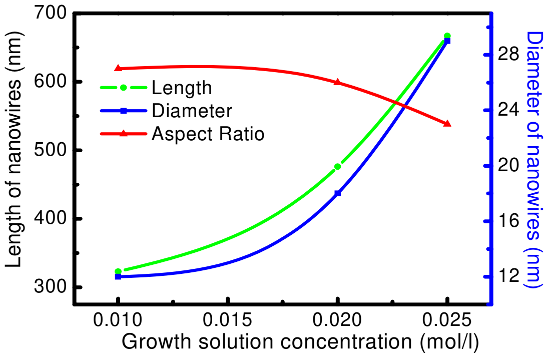

Fig. 7. *Length and diameter of ZnO nanowires vs. the concentration of grown solution*

4. Conclusions

A selective growth of 1D nanostructured oxide materials on glass and silicon substrates was obtained by combining the direct patterning of the ZnO film via microcontact printing and subsequent low-temperature hydrothermal growth.

The nature of the substrate influences the homogeneity of the patterned ZnO film and subsequently the direction of the growth and the aspect ratio of ZnO nanowires. Ordered and very good quality single-crystal ZnO 1D nanostructures can be grown from solution on a localized area of the substrate patterned by microcontact printing.

Acknowledgement

The research presented in the paper was financed by MNT ERA-NET 7-029/2010 Multinanowires project. The work of Anca-Ionela Danciu was supported by Project SOP HRD – EFICIENT 61445/2009.

References

[1]. Sheng Xu, Chen Xu, Ying Liu, Youfan Hu, Rusen Yang, Qing Yang, Jae-Hyun Ryou, Hee Jin Kim, Zachary Lochner, Suk Choi, Russell Dupuis, and Zhong Lin Wang - *Adv. Mater.* XX, (2010), 1–5.

[2]. Nguyen Le Hung, Hyojin Kim, Soon-Ku Hong and Dojin Kim - *Advances in Natural Sciences: Nanoscience and Nanotechnology*, 2 (2011) 1-6.

[3]. Shi-Ming Peng, Yan-Kuin Su, Liang-Wen Ji, Sheng-Joue Young, Chi-Nan Tsai, Jhih-Hong Hong, Zong-Syun Chen, and Cheng-Zhi Wu - *Ieee Transactions on Electron Devices*, 58 (2011) 2036 - 2040.

[4]. Kyoungwon Kim, Pulak Chandra Debnath, Sangsig Kim, and Sang Yeol Lee - *Applied Physics Letters 98* (2011) 113109-1 - 113109-3.

[5]. S. Garry, E. McCarthy, J.P. Mosnier, E. McGlynn - *Applied Surface Science* 257 (2011) 5159–5162.

[6]. Q. Ahsanulhaq, Jin Hwan Kim, Jeong Hyun Kim, Y. B. Hahn - *Nanoscale Res Lett* 5 (2010) 669–674.

[7]. Duk-I Suh, Seung-Yong Lee, Jung-Hwan Hyung, Tae-Hong Kim, and Sang-Kwon Lee - *J. Phys. Chem.* C 112 (2008), 1276-1281.

[8]. Yongsheng Zhang, Ke Yu, Shixi Ouyang, Ziqiang Zhu - *Materials Letters* 60 (2006) 522–526.

[9]. In-Sung Hwang, Yoon-Sung Kim, Sun-Jung Kim, Byeong-Kwon Ju, Jong-Heun Lee - *Sensors and Actuators* B 136 (2009) 224–229.

[10]. Hyun Wook Kang, Junyeob Yeo, Jin Ok Hwang, Sukjoon Hong, Phillip Lee, Seung Yong Han, Jin Hwan Lee, Yoon Soo Rho, Sang Ouk Kim, Seung Hwan Ko, and Hyung Jin Sung - *J. Phys. Chem.* C 115 (2011), 11435–11441.

[11]. Zongyou Yin, Qiyuan He, Xiao Huang, Gang Lu, Huey Hoon Hng, Hongyu Chen, Can Xue, Qingyu Yan, Freddy Boey, Qichun Zhang, and Hua Zhang - *Langmuir* 26(7) (2010), 4616–4619.

[12]. Quanguo He, Zhengchun Liu, Nongyue He, Pengfeng Xiao, and Zuhong Lu Rongqing Liang, - *Langmuir 19* (2003), 6982 – 6986.

[13]. Cheng Hung Wang, Andrew See Weng Wong, and Ghim Wei Ho - *Langmuir 23* (2007), 11960-1196.

THE ANNALS OF "DUNAREA DE JOS" UNIVERSITY OF GALATI.
FASCICLE IX. METALLURGY AND MATERIALS SCIENCE
N^0. 1 – 2012, ISSN 1453 – 083X

ALUMINUM FOAMS WITH CLOSED PORES OBTAINED BY CASTING TECHNIQUES

Virgil GEAMĂN, Mihai Alin POP, Vasile JIMAN
Transilvania University of Brasov
email: geaman.v@unitbv.ro

ABSTRACT

Techniques for the preparation of metallic foams, including casting, powder metallurgy and metallic deposition, have been reviewed. There is a present interest in the development of materials capable of plastic deforming to absorb the effects of shock and impact. Solid foams form an important class of lightweight, cellular engineering materials to meet these threats. The foam materials themselves may be divided into two classes according to their morphology. The first group is open cell structured foams containing pores that are connected to each other and form an interconnected network. The second class does not have interconnected pores and is termed as closed cell foams. The paper presents some experimental data for obtaining aluminum foams with hollow pores by casting techniques. The specific equipment used for experiments is also described.

KEYWORDS: aluminum, foam, pore, casting technique, equipment, cell

1. Introduction

Porous materials are known to have a high stiffness combined with a very low specific weight. The fact that even metals and metallic alloys can be produced as cellular solids or metal foams is not as well known as the possibility to foam more traditional engineering materials such as polymers, ceramics or glass.

Metallic foams offer interesting perspectives due to the combination of properties which are related to the metallic character on the one hand and to the porous structure on the other hand.

In the past 40 years many attempts have been undertaken to foam metals or to produce porous metallic structures.

There is no clear-cut and generally accepted definition for the term "foam". First of all, one has to distinguish between liquid and solid foams. A liquid foam is a fine dispersion of gas bubbles in a liquid. Cooling down a liquid foam beneath the melting point of the respective material yields a frozen liquid foam which is then clearly a solid foam. What is generally meant in the context of metallic foams are in general solid metallic foams.

One could restrict the usage of the word "solid foam" to materials which originally were in the liquid state. However, customarily other porous structures such as sintered metal powders are often also called "foams" although they were never in a liquid state. So one often extends the usage of the word "foam" to porous metal structures which are no actually foams, but resemble foams regarding their high porosity, the inter-connectivity of the solid material and their irregular structure.

2. Foams made from metallic melts

A first group of foam making processes starts from the molten metal that is processed to a porous material by either foaming it directly, by using an indirect method via a polymer foam or by casting the liquid metal around solid filler materials which reserve space for the pores or which remain in the foam.

Metallic melts can be foamed directly under certain circumstances by injecting gases into the liquid. Normally, the gas bubbles which are then formed in the metallic melt will tend to rise to its surface quickly due to the high buoyancy forces in the high-density liquid but this rise can be impeded by increasing the viscosity of the molten metal. This can be done by adding fine ceramic powders or alloying elements which form particles in the melt.

It should be noted that numerous attempts to foam liquid metals have been undertaken in the 60s and 70s [1], but apparently the processes then invented could not be sufficiently optimised to yield foams of a satisfactory quality and cost. In the past ten years, however, a number of new developments have taken place so that nowadays better production routes are available.

The second way for foaming melts directly is to add a foaming agent to the melt instead of blowing gas into it [1, 2]. The foaming agent decomposes under the influence of heat and releases gas which then propels the foaming process. Calcium is used to stabilise the melt (probably forming an Al_4Ca intermetallic) and titanium hydride TiH_2 serves as the foaming agent releasing hydrogen gas when it is heated. Typical densities are 0.25 to 0.33 g/cm^3.

The projections of the future fuel crisis, the requirements of achieving high fuel efficiency along with higher passenger safety in the automobile industry, and the needs of creating light weight construction materials have attracted tremendous consideration for ultra light weight metallic foams.

In general, metallic foams possess a range of thermo-mechanical properties that suggest their application in areas demanding impact/blast amelioration, heat dissipation, acoustic isolation and heat exchange [3, 4].

The projected applications of metallic foams have already been recognised and a detailed description of the requirements of various industrial sectors can be seen elsewhere [1, 3, 4].

Recently, National Physical Laboratory (UK) made a survey both in industries and in research institutions to have an idea of potential expectations from metallic foams.

The survey indicated that the major applications of metallic foams, around 32%, in the near future would be directed towards automotive and aerospace industries (Fig. 1).

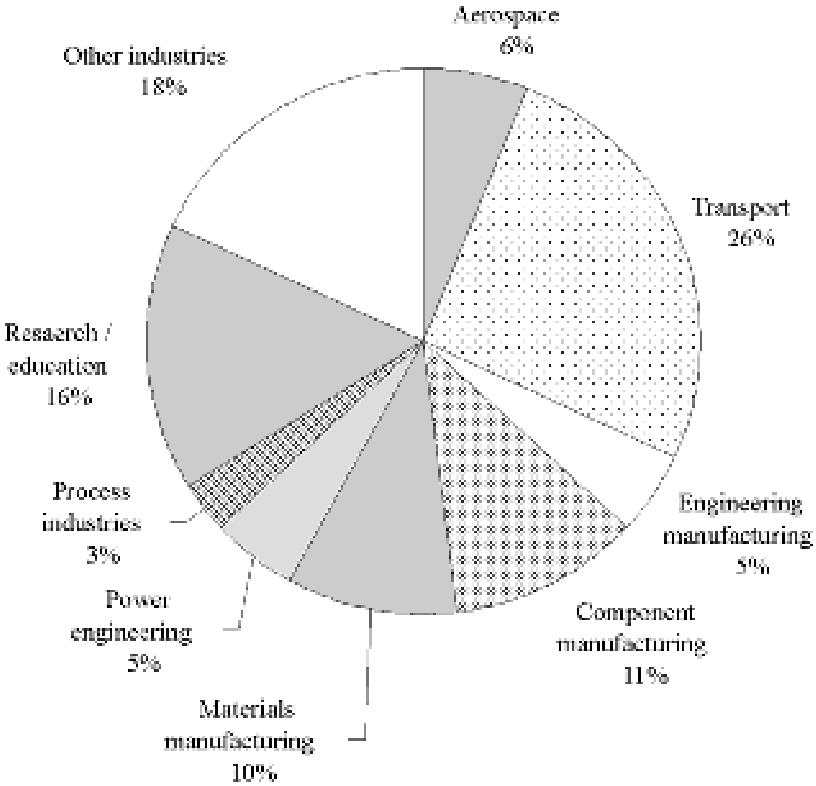

***Fig. 1.** The implementation of metallic foams*

3. Experimental results

Metal alloys can be foamed by mixing into them a foaming agent that releases gas when heated. The widely used foaming agent titanium hydride (TiH_2) begins to decompose into Ti and gaseous H_2 when heated above about 465°C. By adding titanium hydride particles to aluminum melt, large volumes of hydrogen gas are rapidly produced, creating bubbles that can lead to closed-cell foam, provided foam drainage is sufficiently slow, which requires a high melt viscosity [5, 6]. The process begins by melting aluminum and stabilizing the melt temperature between 670 and 690°C. Its viscosity is then raised by adding 1–2% of calcium which rapidly oxidizes and forms fine dispersed CaO and $CaAl_2O_4$ particles. The melt is then aggressively stirred and 1–2% of TiH_2 is added in the form of 5–20μm diameter particles. As soon as these are dispersed in the melt, the stirring system is withdrawn, and a foam is allowed to form above the melt. Control of the process is achieved by adjusting the over pressure, temperature and time. It takes, typically, about ten minutes to totally decompose the titanium hydride. When foaming is complete the melt is cooled to solidify the foam before the hydrogen escapes and the bubbles coalesce or collapse. The volume fraction of calcium and titanium hydride added to the melt ultimately determines the relative density and, in combination with cooling conditions, the cell size. The cell size can be varied from 0.5 to 5mm by changing the TiH_2 content, and the foaming and cooling conditions. In figures 2 and 3 are given some results of the foam obtained from aluminum alloy ATSi5Cu1 in the Casting Laboratory from Materials Science & Engineering Faculty - Transilvania University of Brasov.

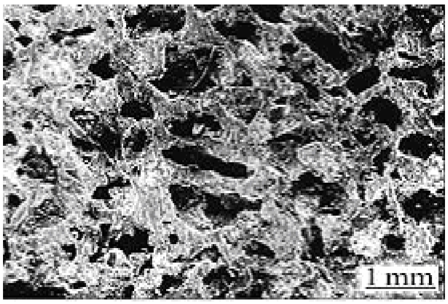

Fig. 2. *Micrography of ATSi5Cu1 – aluminium alloy with 1.5mm average size of pores*

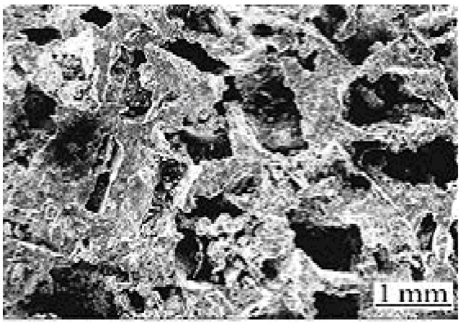

Fig. 3. *Micrography of ATSi5Cu1 – aluminium alloy with 2mm average size of pores*

a).

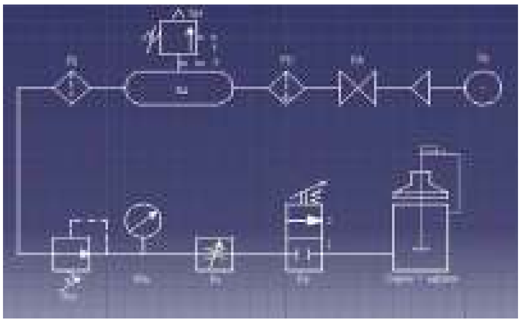

b).

Fig. 4. *Experimental equipment:*
a). view, b). scheme

All the experimental results are made in a specially equipment designed by authors – seen in Figure 4.

3. Concluding remarks

Recent technological advances in the field of metallic foams have led to the development of a wide range of processing techniques for the open, as well as closed cell morphologies.

The processing route has to be decided on the basis of the cost of production, materials properties, and the intended applications of the final product. However, as the cost of production of a good quality metallic foam is still high, continual innovations are underway so as to draw maximum benefit by opening new avenues for a wide range of industrial applications.

References

[1]. Michael F. Ashby, Anthony Evans, Norman A. Fleck, Lorna J. Gibson, John W. Hutchinson, Haydn N.G. Wadley - *Metal Foams - A Design Guide*, (2000), Butterworth-Heinemann Woburn, MA 0180-2041.

[2]. H.N. Wadley, N.A. Fleck, A.G. Evans - *Fabrication and structural performance of periodic cellular metal sandwich structures,* Composite Science and Technology, vol.63, (2003), pp. 2331-2343.

[3]. Haydn N.G. Wadley - *Cellular metals manufacturing*, Advanced Engineering Materials, vol.4, (2002), pp. 726-733.

[4]. J.C.Wallach, L.J. Gibson - *Mechanical behavior of three-dimensional truss materials*, International Journal of Solids and Structures, vo.38, 2001, pp. 7181-7196.

[5]. A.G. Evans, J. W. Hutchinson, M. F. Ashby - *Multifunctional of cellular metal systems*, Progress in Materials Science, vol. 43, (1999), pp. 171-221.

[6]. David J. Sypeck, Haydn N.G. Wadley - *Cellular metal truss core sandwich structures*, Advanced Engineering Materials, vol. 4, pp. 759-764.

THE ANNALS OF “DUNAREA DE JOS” UNIVERSITY OF GALATI.
FASCICLE IX. METALLURGY AND MATERIALS SCIENCE
N^{0}. 1 – 2012, ISSN 1453 – 083X

ASPECTS REGARDING THE TRADITION OF BELL MANUFACTURE AND USE

Ioan CARCEA, Oana BĂLŢĂTESCU, Raluca-Maria FLOREA
”Gheorghe Asachi” Technical University of Iaşi
email: ioan.carcea@yahoo.com

ABSTRACT

The paper presents the casting art of bells, their spiritual significance, as well as their evolution over time. The bells may be made of both metallic or/and non-metallic materials, of various shapes and sizes. While producing the adequate sounds, bells have found a universal use: they served as musical instruments, sound devices used in religious rituals, for communication and warning signals. In the European world, the progress and the performances regarding of bells development are owed to their use in the Christian Church rituals.

KEYWORDS: art casting, bells, multi-criteria analyses

1. Spiritual significance of bells

It is widely known that the shape of the bell, known today mostly from graphical statistics, is a medieval invention. Before this, the bells used to look like flipped pots, bowls, or bee hives, but never like what we know as being a bell: a carved bowl with an enlarged mouth. This shape was the result of an ultimate rupture with all the previous shapes. The main characteristic of the new shape was the transformation of the neck, barely perceptible at first, from convex to concave; however, the fact that the new shape discovered an unknown potential for the use of bronze became obvious: this alloy endowed the bell with a controlled secondary sound, higher than the percussion note but, surprisingly, creating a particular roar, way lower than the main note, and which is rather felt than heard. By the end of the 13th century, the bells adopted a gradual interior hollow, which strengthens its murmur rumble, its whispered vibration [1].

The bells crown was flatted, its shoulders enlarged, its lateral parts opened until the mouth, and the thickness of the walls was calculated and tuned. Following the differences between working with cast iron and metal, the characteristic sound of each region bells became a familiar element for geography in the late Middle Ages.

Thus, the technologic instrument which incorporated the divine word in a metallic sound, coming from the church steeple, and which dressed each parish in a distinct acoustic mantle, was designed: from the bells swinging and knelling in the North-West, answering to the Flemish beats with the tuned sounds of several bells, to the tempestuous and noisy oscillations from around the Mediterranean.

The Chinese used to ring the bells to announce the meetings of the Imperial Gatherings; they used four different tongues to command the soldiers “to fight, and to dance”. As it seems, the noise making instruments have been widely used, and not only to attract the attention, but also to clean

the air of unwanted spirits or to cast away the stormy clouds. According to Josephus, King Solomon suspended a golden bell on the highest beam of the temple to chase away the birds. The Romans used to tie tintinnabula on their shields, to attract the enemy’s attention on the paralyzing face of Medusa, carved on the bronze plate in the middle of the shield. The bells used to open the place for the Bacchante processions. In Astarte’s cult, the priests used to hit a ring that made a sharp sound.

The Greek and Latin authors could not tell the large bell, with the shape of a cup, of the almost enclosed sphere of the spherical bells. Most bells in the Mediterranean Antiquity were small enough to be sewed on the clothes, or held and shaken with one hand. The bigger ones, like gongs or metallic cylinders, were used to announce the fish markets, the baths, and the circus. Plutarch wrote about “bells on nets spread over the river, which rang when people tried to swim, and escape the besieged town Xanthus”.

The dogs, horses, cows, goats, pigs, and sheep were wearing bells on their neck; the skeletons of two horses, each of them wearing three bells, were found in Pompeii. The shepherds wanted to be buried together with the bells they put on their animals’ necks. The ringing kept the vampires and the ghosts away of their goats and cows, and might as well guard their lifeless body of such supernatural beings. A Christian martyr, Sisinnus, was buried wearing a bell on his neck by court order; the Roman magistrate wanted to show, this way, his disregard for the accused, a man that was as irrational as a beast. The Greek night guard was known by the name of codonophor, a bell wearer. The social women in Pompeii used chimes as earrings. In the Middle Ages, the brain-sick, the leprous, the executioners, and the public fouls were forcibly sewed bells on their clothes.

After becoming a symbol for the missionary, the molded bells were treated, in the christened Europe, as being some sort of persons. The bells usually had names; the name and the “vocation” of a bell were carved on its crown. These are several typical inscriptions: *„Laudo Deum verum* [praise the real God] ... *plebem congrego* [gather the people] ... *vivos voco* [call the living] ... *defunctos ploro* [mourn for the dead] ... *pestem fugo* [banish the plague] ... *fulgorem frango* [chase away the stormy clouds] [2].

The oldest text preserved, about the special blessing, for the church bells, comes from Spain, a few years before the Muslims conquered the peninsula. The ceremony starts with the solemn exorcizing of the molten metal; the evil, and the unholy spirits which attached to the metal on its birth in the womb of the Earth are cat away from the mass of boiling metal. The priest prays for the bronze to become as pure as the trumpets used by holy orders in Sinai – for God to endow the sound of this bell with the power to clean the laziness and the stupor in the hearts, to extinguish the flames of lust, and to light the weight of the sin, in everyone it touches – for God to give it the power to strengthen the week ones, to comfort the sad ones, and give courage to repent for the sinners.

It is obviously an austere blessing ceremony; in this early text, no words appear about the peculiar rites that treat the bell, a century later, more as a person than an object – and which determined Carol the Great to forbid the bells “baptizing”, in 798: *ne cloccas baptizent*.

On the contrary, with the large acceptance of bells in churches from Western Europe, in the religious area of the Eastern Roman Empire and the Byzantine Empire, they entered later, and with some difficulty. Although the Constantinople had been given a set of bells ever since 886, they were only used to announce the hours, at the Imperial Palace, and the Latin Rite church. The Orthodox Christians in the East were rather used to the sound of an elder instrument – the vesper – the wooden piece that resonates while hit with mallets, and produces various sounds [3].

The museum association of bells and cannons: the conversion of one to the other, bells to cannons, in time of war, and cannons to bells, in time of peace, was a usual behavior for all the peoples, over all times. Such a situation appeared, for the first time, in Russia, in the time of Tsar Peter the First, who, after losing all the Russian artillery in the battle with the Swedish, near Narva, in 1700, ordered all the laic and monastic communities to donate a third of the total bells they had, to recover the artillery. This operation determined the communities to firstly give away the defective bells, which were later replaced by newer ones, more beautiful and durable, and this aspect may be considered as a refreshing moment for the symbolistical patrimony on a national scale.

2. The Evolution history of bells

Ever since the 16th century, a real competition to produce increasingly bigger bells had started. In 1520, in Pskov, the brothers Michael, Onophreus, and Andrew, cast two bells: one weighting 6 tons, and the other, 3.5 tons, the biggest bell ever cast by them having 6.4 tons. In 1533, under Tsar Basil III, a 16 ton is cast, and in 1551, Ivan IV orders the casting of a 35 ton bell, which, owing to its exceptional ringing, was named “The Swan”.

The 17th century comes with the triumph of the bell casting art in Russia and strengthens the position of the Russian manufacturers on the European bell market, successfully competing with the German or Polish foundries. The customs were equally impressive: it was already traditional in Moscow, for the exact midnight of Easter’s Eve, the first and the only bell which shared the news of Jesus Revival, to be the big bell in the Kremlin Tower; after that, sounds of over 3500 bells burst over the giant city. These bells used to ring for a whole week. In this week, after the Easter, the local rites permitted to any citizen to ring the bells of any church, if he wanted, this being also a good occasion of “live” practice for the aspirants on the sexton job.

The transformation of bells in cannons determined the adjustment of the foundries and, consequently, the regress of bell casting, but the stagnation period was short. For example, the statistics show 13 foundries in the area of the new Capital St. Petersburg that cast, in 1811, 4220 bells and some other tens of thousands of sleigh bells. The famous Russian sleigh bells of the horses carrying troikas have a history close to the times of the first Slavic migration and their settling on the territory which will later become Russia. The most famous chimes and sleigh bells are the “Valday Chimes”, often sung by the Russian classics and quasi-present in the folklore and cult literature. The numeric increase of bells and chimes was favored by the

Russian territorial expansion in the depths of Asia, where the conquered peoples tried to oppose the occupation, cut could not oppose the adoption of some objects (sleigh bells) or some habits (Christianity), together with the use of bells, imposed by the Russian church, which was also trying to expand. This tendency was even found in Alaska and the Aleutian Islands, where the first missionaries, in the 18th century, installed the first bells, for the Orthodox Christian missions created here [4].

Of the most important donations of bells, from the Russian tsars for the North American communities, we can mention those made by Emperor Alexander III – to the Holy Trinity Cathedral in San Francisco, and the Orthodox Church of the American Western Diocese, or the one made by the Martyr Tsar – Nicholas II to the Bridgeport Church, in 1894, to celebrate his coronation.

The great trial for the Russian Church comes with the beginning of the revolution, in 1917, and lasts for all the functioning period of the soviet and communist regime.

In 1941, out of over 60,000 churches and 1000 monasteries and abbeys, there were only about 500 churches still functioning, and just a few of them kept their bells; however, the use of bells was prohibited by a "directive" in 1935, and, as a result, only one set of bells from Kremlin was allowed to ring, as horologe, but with the imposition of a new melody, on a new rhythm.

A set of bells which remained untouched is the three bell set in Rostov; for unknown reasons, these were protected for unknown reasons by the Ministry of Culture, in the regime of Stalin. Later, after the Cuban missile crisis in 1962, the Russian Government disposed an extremely unusual measure: the reposition of these bells as "cultural artifacts" and, even more surprisingly, the recording of an LP called "The Bells of Rostov", but the text accompanying the recording made no reference to religion.

The faith retaliates now: the old armament factories, with insufficient commands, now switched to bell casting, an activity that proves to be profitable, on a continuously growing and long term secure specific market. If the 20th century was one of atheism in the USSR, the 21st - the first of the Second Millennium of the Russian Orthodox Church and the third of the mankind will be a profoundly religious one, or will not be at all.

Other famous bells are those from the Danilov Monastery, of which the biggest, cast in 1654, weighed 131 tons, and its sound could be heard on a distance of over 17 km, and many times, dialogue, were carried between the bell towers of Kremlin and Danilov. It seems that the exuberance manifested by the Danilov Monastery sexton, during such a dialog, produced major damage to the big bell, which had to be restored. The bells in here were reserved an unfair faith, but better than other bells in the Tzarist Russia. When the Soviet Government decided the destruction of these bells in 1930, they had the chance to be redeemed by the American industrialist Charles Crane, which paid for their disassembly and transfer to the USA. Even today, they still resound at Harvard University, although the Russian officials started the redeeming approaches in the 90s, in order to bring them back to their rightful place before 2003 – the Anniversary for 700 years since the Monastery foundation, so they would be the same rang bells which Gogol heard and evoked.

This was not possible due to the very high costs of such an operation, even though the initiative was personally sustained by President Ronald Reagan; this way, the Danilov Monastery had to celebrate the century-old anniversary with the bells cast in 1988, the year when Mikhail Gorbachev considerably lowered the religious persecution imposed for several decades by the soviet regime, and permitted the organization of the manifestations related to the Anniversary of 1000 years of Orthodox Christianity in Russia [5].

The 17th century was marked by the realization of The Grand Bell – TSAR KOLOKOL, but also the set of three big bells in Rostov, of 8, 16, and 32 tons respectively, which can be heard on a distance of over 30 km.

The Tsar of Bells was made and it existed up until now, but the divine grace punished a wish of greatness, maybe unjustified, and the great bell sits unused in the Red Square, in Moscow, close to another vainglory monument: "The Tsar of Cannons" – another dream of greatness, also never utilized, thankfully, this time. The two symbols have been, and still are, just tourist attractions.

The biggest bell ever cast – The Tsar of Bells – was, in fact, realized at the end of a series of four tries, during almost 150 years. Other three bells which preceded this one have previously wore this name. Here is their brief history:

- the first one was cast in 1599, during the regime of Boris Godunov, by the master caster Andrei Chohov: it weighted 35 tons, and ended in the fire in Moscow, in the 17th century;
- the metal from the first bell was melted and used to cast the second Tsar Kolokol: this one was released in 1654, under Tsar Alexei Mikhailovich, by the metallurgical master Emilian Danilov, weighing 128 tons, and being cast in the premise of Kremlin. Satisfied with this result, the Tsar ordered it to be lifted on an improvised stand, and ringed in competition with all the other bells in Moscow, drawn simultaneously. The experiment succeeded, and the arbitrators noted that the sound of the Great Bell dominated, being heard on a 40 km distance, covering

all the others; however, the ardor of the 25 soldiers that made it ring, moving its heavy tongue, possibly combined with a casting imperfection, makes that after only one hour, the bell gives an unnatural sound, and then falls down in pieces. Disappointed, the Tsar ordered the immediate remake of the bell.

- the third Tsar Bell was cast the next year, in the same place, and the honor to coordinate the work was given to a 20 year old master – Alexander Grigoriev. This bell had 160 tons of incorporated metal and was called "The Bell of the Great Dormition", after the Cathedral of the Dormition in Kremlin. Ten years had to pass until it could be provisionally set in a wooden tower, and another 10 years until the definitive settlement in the tower called "Ivan the Great". This one could only be used occasionally, and this only after all Moscow has been previously warned, as its sound would produce such an intense vibration, that it felt similar to a small earthquake. This one resisted until 1701, when a fire in Kremlin leads to its falling and breaking [6]:

- in 1730, Tsarina Anna Ioannovna commanded the collection of the broken bell's remains and the casting of a new one, with the addition of approximately 35 tons of bronze. The task was taken by the master Ivan Motorin who, for 5 years, tried countless solutions, and even a casting – which was a failure, and led to its death, due to fatigue and sadness. His work was continued by his son, Mikhail Motorin, who perfectly organized the whole process and managed to cast the bell from the first try, in 1735. The history recorded this fact as a true performance, the whole quantity of molten metal, 196.556 kg, being cast in the matrix in only 36 minutes; and this really is a performance, as to cast 6 tons of metal per minute is not easy, even now.

Unfortunately, not even this last Tsar Bell was made to ring. As long as it was still on the place where it was cast, and the metal was not cold yet, an unexpected fire started and collapsed the wooden scaffold over the bell. The workers, with a good intention to save it, but unskilled, poured water that made it crack, and a piece of 11 tones disengaged. This way, the Great Bell lay down for almost 100 years, until the 19th century, when its move on an especially built pedestal was commanded, so the greatness and richness of its decorations can be admired. The experts of the time and the ones after consider that, if that bell could ring, it would have become a real danger for all the constructions around it, for an area of a few kilometers, as its vibrations would have collapsed everything, including Kremlin, the palaces and cathedrals around, and everyone in the surrounding area would have become death at the first ring. The bell named "Saint Peter", the largest bell on the Rin, is 3 meters high, weights 24 ton, and its sound is heard over more than 30 kilometers.

Bells like "Saint Peter" have been heard in Europe in an era in which the sense of the place suffered an extraordinary transformation. The technology, stimulated by horses, permitted the people to live together, to move from hamlets to real villages. The urbanization supported the regular gatherings in rural markets. The church created parishes with resident clerics and established a new set of regulations to control the marriages and the communal life. The Central Europe establishment processes populations have earned, during Early Middle Ages, lots of characteristics that were kept up until the 19th century. The communities were spread as far as the bells were heard, mixing up in a new manner.

The use of the tower building to spread a religious sound was an invention born in the Early Middle Ages, taking the form of the bell tower and the minaret.

Starting in the 5th century, the churches started to build towers for bells. San Apollinare Nuovo and San Apollinare in Classe in Ravenna have round towers. A mosaic in Santa Maria Maggiore in Rome, created in the time of Sixtus III (432-440), shows a church with two such round towers.

The wish to hang the bell in a high place precedes the existence of those very powerful and heavy bells; hence a special building was needed to shelter them. In 752, Pope Steven III built a steeple for three church bells in Rome, at Saint Peter. The weight of the tintinnabuli and the wish to make it heard contributed to ordering this special architectural piece of work. In the 11th century, the steeple's tower became a common image, and in the 13th Century, it already became a part of any parochial church or cathedral. Gradually, it started to be also used in the Orthodox Church. Around the year 865, the Doge Orso sent twelve bells from Venice to the Emperor Michael III, known by the name of "The Drunk". These bells have been installed in the magnificent steeple near Saint Sophia and, in less than a century, the bells could be heard in the neighboring Lavra, and then on Mount Athos; however, the bell did not compete with the simandrum as a convocation instrument. There is no doubt that the affirmation that the bell is an occidental invention and that the Orthodox Church had not used it before the 11th century is an exaggeration. Anyway, it is a sure thing that the most prevalent instrument used to summon the believers to the ministry was the "holy wood".

Even more remarkable than the ecumenical acceptance of the bell in the Eastern and Western Churches is the recognition of the important civic role of the bell along the 19th century. During the liberal anti-ecclesial waves in the South-European countries, the "right for the bell" became a major litigation reason between the catholic bishop and the civil authorities. Why would the prefect have the right to silence the bells after 7 in the evening? Or to order the bells to be rang to announce a fire, or to announce the passing of an important person through the city? If this was the case, should not the municipality pay the bell ringer? Does the municipality have the right to forbid the ringing of the “death bell” in case of a pestilence, to avoid general panic? From a survey on the Court Orders and the decisions of the Supreme Court in France, the fact that, until the beginning of the 20th century the sound of bells establishes, in a powerful manner, the sovereignty on the space that it fills, becomes very clear.

3. Bell manufacturing techniques

The bell has its own structure, and for a best functioning, it must be put in an optimal relationship with the mechanism that engages it to make the sound [7].

The first step in the manufacture of a bell is the creation of the core. This one is manufactured the first, in a brute form, close to the final one, from bricks, and then it is finished by adding the formation mixture.

The core is covered with a dust (a layer of grease, in other situations), so the core would not adhere to the surface of the fake bell – the one made of ceramic (or wax, as it was used in older times).

Fig. 1. *Core bell*

“The fake bell”, or the one made of ceramic, is covered with a thin layer of wax which - at the moment when the superior part of the casting matrix becomes dry - melts and permits its separation of the fake bell. Before covering the fake bell with a new layer of a clay (which will become the superior part of the casting matrix), this will be decorated with wax ornaments.

Fig. 2. *Fake bell*

A very fine formation mixture, that should take all its details, is applied in thin layers over the wax surface that covers the fake bell.

A metallic carcass is put around this ensemble, and the free space between them is filled with formation powder.

The ensemble is warmed up in order to dry up the superior part of the matrix, while the thin wax layer melts down; after that, the matrix is lifted to clean the interior of the rests of unmolded wax and other potential impurities [8].

After these operations are over, the fake bell is removed, and the space it used to occupy is filled with molten bronze. This one is poured in the final matrix, at 1050-1100°C. The pouring must be continuous, and under qualified personnel supervision, so no impurities interfere during the cast. The cooling is made very slowly and, for this reason, the casting and the cooling processes are made with the casting matrix on the ground. After the cooling, the formation mixture is removed, and the bell’s sound adjustment is made.

Fig. 3. *The biggest bell in Russia and the whole world is the "Tsar's Bell" or "The Empress' Bell", kept in Kremlin. It is put on a pedestal at the base of "Ivan the Great" steeple's tower. Its dimensions and art are still unequaled in the world*

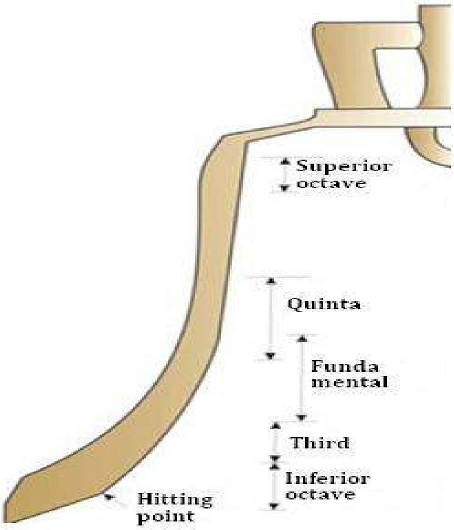

Fig. 4. *Musical tones of the bell*

4. Modeling elements in bells execution

4.1. General

Advanced multi-criteria analysis is a general method to compare products, services or activities that has proven effective.

This chapter aims to analyse various materials used for casting bells. Analysis consists in a performance coefficient derived from calculations for ranking the analyzed products [9].

4.2. Analyses establishing alternatives

In this analysis materials used for casting bells were compared. These materials are presented in Table 1.

Table 1. *Materials and symbols used in the analysis*

M1	*M2*	*M3*	*M4*	*M5*	*M6*	*M7*	*M8*
Special Bronze (20-22% Sn)	Industrial Bronze (6-14% Sn)	Special Brass	Alloyed Iron	Alloyed Stell	Al Alloys	Crystal	Ceramic

4.3. Advanced multi-criteria analysis of variants selected for comparison

To make a comparative analysis in terms of performance following ten criteria were established:

C1 - bell sound amplitude vibrations;
C2 - time maintaining vibration in the ear;
C3 - Specific musicality;
C4 - aesthetics exposed surfaces;
C5 - technological properties of molding;
C6 - technological properties of casting;
C7 - surface processing capacity;
C8 - mechanical resistance characteristics;
C9 - resistance to corrosion;
C10 - manufacturing costs.

Table 2. *Comparing for individual criteria results*

Ci	***C1***	***C2***	***C3***	***C4***	***C5***	***C6***	***C7***	***C8***	***C9***	***C10***	***p***
C1	0.5	0.5	1	1	1	1	1	0.5	0.5	0.5	7.5
C2	0.5	0.5	0.5	1	1	1	1	0.5	0.5	0.5	7
C3	0	0.5	0.5	1	1	1	1	0.5	0.5	0.5	6.5
C4	0	0	0	0.5	0.5	0.5	0.5	0	0	0	2
C5	0	0	0	0.5	0.5	0.5	0.5	0	0	0	2
C6	0	0	0	0.5	0.5	0.5	0.5	0	0	0	2
C7	0	0	0	0.5	0.5	0.5	0.5	0	0	0	2
C8	0.5	0.5	0.5	1	1	1	1	0.5	0.5	0.5	7
C9	0.5	0.5	0.5	1	1	1	1	0.5	0.5	0.5	7
C10	0.5	0.5	0.5	1	1	1	1	0.5	0.5	0.5	7

Weighing coefficients “Y_i” are calculated with Frisco:

$$Y_i = \frac{p + |\Delta p| + m + 0.5}{\frac{N_{CRT}}{2} + |\Delta p'|} \qquad (1)$$

where: p - the amount on line points for each criterion;

Δp - difference between the criterion score and the score criterion taken from the last level;

m - number outclassed criteria;

N_{CRT} - total number of criteria;

Δp’ - difference between the criterion score and the score criterion taken from the first level.

For each material were granted N_{ji} notes to the way they satisfy each criterion of comparison.

The notes represent an integer from 1 to 10.

Table 3. *“Y_i” weighing coefficients calculation results for each criterion*

Ci	***p***	***level***	***Δp***	***m***	***N_{CRT}***	***Δp’***	***Y_i***
C1	7.5	1	5.5	9	10	0	4.5
C2	7	3.5	5	5	10	-0.5	4
C3	6.5	6	4.5	4	10	-1	2.666
C4	2	8.5	0	0	10	-5.5	0.238
C5	2	8.5	0	0	10	-5.5	0.238
C6	2	8.5	0	0	10	-5.5	0.238
C7	2	8.5	0	0	10	-5.5	0.238
C8	7	3.5	5	5	10	-0.5	4
C9	7	3.5	5	5	10	-0.5	4
C10	7	3.5	5	5	10	-0.5	4

Table 4. *Grades given according to performance criteria for the analysed materials*

Material symbol	***Grades given according to performance criteria***									
	C1	***C2***	***C3***	***C4***	***C5***	***C6***	***C7***	***C8***	***C9***	***C10***
M1	10	10	10	10	8	7	9	6	9	1
M2	7	7	5	10	8	7	9	9	8	2
M3	8	8	7	10	9	7	9	7	8	4
M4	5	5	5	7	8	4	8	5	1	8
M5	5	5	5	6	7	2	5	10	1	7
M6	5	5	5	9	10	10	9	8	9	8
M7	7	8	9	10	5	5	8	5	10	6
M8	5	5	4	8	3	3	10	1	9	10

Based on Table 4 for each material were calculated partial coefficients F_{ji} value in relation to each criterion as:

$$F_{ji} = Y_i \cdot N_{ji} \qquad (2)$$

Then for each material the sum of these factors was calculated:

$$FV_j = \sum_{i=1}^{i=10} F_{ji} \qquad (3)$$

Table 5. *Calculation results of partial and total value coefficients and total value of analysed materials*

M	***Partial value coefficients, F_{ji}***										***FV_j***
	C1	***C2***	***C3***	***C4***	***C5***	***C6***	***C7***	***C8***	***C9***	***C10***	
M1	45	40	26.66	2.38	1.904	1.666	2.142	24	36	4	183.752
M2	31.5	28	13.33	2.38	1.904	1.666	2.142	56	32	8	176.922
M3	36	32	18.662	2.38	2.142	1.666	2.142	28	32	16	170.992
M4	22.5	20	13.33	1.666	1.904	0.952	1.904	20	4	32	118.256
M5	22.5	20	13.33	1.428	1.666	0.476	1.19	40	4	28	132.59
M6	22.5	20	13.33	2.142	2.38	2.38	2.142	32	36	32	164.874
M7	31.5	32	23.994	2.38	1.19	1.19	1.904	20	40	24	178.158
M8	22.5	20	10.664	1.904	0.714	0.714	2.38	4	36	40	138.876

Table 6. *Ranking of the materials used for casting bells according to the total calculated coefficient of performance*

Place	***Material symbol***	***Material description***	***FV_j***
1	M1	Special Bronze (20-22% Sn)	183.752
2	M7	Crystal	178.158
3	M2	Industrial Bronze (6-14% Sn)	176.922
4	M3	Special Brass	170.992
5	M6	Al alloys	164.874
6	M8	Ceramic	138.876
7	M5	Alloyed Steell	132.59
8	M4	Alloyed Iron	118.256

5. Conclusions

The results and rankings in Table 6 show that the first material for casting bells is special bronze with a performance coefficient value of FV_j = 183.752. For industrial bronze the performance coefficient value is FV_j = 176.922.

On this score industrial bronze is ranked third in the classification of materials used for casting bells. Even if some estimates may lead to some error margin, of error, the results reveal that bronze occupies a special place in the materials used for obtaining and casting bells.

On the other hand, the research carried out and the results show that the use of the multi-criteria method can be successfully extended in every industry, including the casting alloys.

References

[1]. Michelle E. Garceau -*‘I call the people.’ Church bells in fourteenth-century Catalunya*, Journal of Medieval History, 37, (2011), 197–214.

[2]. Salvador Ivorra, Francisco J. Pallares, *Dynamic investigations on a masonry bell tower*, Engineering Structures, 28, (2006), 660–667.

[3]. Salvador Ivorra, Francisco J. Pallarés, Jose M. Adam - *Dynamic behaviour of a modern bell tower - A case study*, Engineering Structures, 31 (2009), 1085–1092.

[4]. Jernej Klemenca, Andreas Ruppb, Matija Fajdiga - *Dynamics of a clapper-to-bell impac*t, International Journal of Impact Engineering, Volume 44, June 2012, Pages 29–39.

[5]. Giovanni Meneghetti, Barbara Rossi - *An analytical model based on lumped parameters for the dynamic analysis of church bells*, Engineering Structures, Volume 32, Issue 10, October 2010, Pages 3363–3376.

[6]. Marco Lepidia, Vincenzo Gattullia, Dora Foti -*Swinging-bell resonances and their cancellation identified by dynamical testing in a modern bell tower*, Engineering Structures, Volume 31, Issue 7, July 2009, Pages 1486–1500.

[7]. Thomas D. Rossing - *Vibrations of bells*, Applied Acoustics, Volume 20, Issue 1, 1987, Pages 41–70.

[8]. K.N. Strafford, R. Newell, K. Audy, J. Audy - *Analysis of bell material from the Middle Ages to the recent time*, Endeavour, Volume 20, Issue 1, 1996, Pages 22–27.

[9]. I. Ciobanu, D. Tutuianu, S.I. Munteanu, T. Bedo, A. Crisan - *Incursiune in designul pieselor turnate (Journey in casting parts design)*, Ed. Universitatii Transilvania din Brasov, 2011.

MANUSCRISELE, CARŢILE ŞI REVISTELE PENTRU SCHIMB, PRECUM SI ORICE CORESPONDENTE SE VOR TRIMITE PE ADRESA:

MANUSCRIPTS, REVIEWS AND BOOKS FOR EXCHANGE COOPERATION, AS WELL AS ANY CORRESPONDANCE WILL BE MAILED TO:

LES MANUSCRIPTS, LES REVUES ET LES LIVRES POUR L'ECHANGE, TOUT AUSSI QUE LA CORRESPONDANCE SERONT ENVOYES A L'ADRESSE:

MANUSCKRIPTEN, ZIETSCHRITFTEN UND BUCHER FUR AUSTAUCH SOWIE DIE KORRESPONDENZ SID AN FOLGENDE ANSCHRIFT ZU SEDEN:

After the latest evaluation of the journals achieved by National Center for the Science and Scientometry Politics (**CENAPOSS**), as recognition of its quality and impact at national level, the journal is included in B$^+$ category, 215 code (http://www.cncsis.ro/2006_evaluare_rev.php).

The journal is indexed in:
CSA: http://www.csa.com/ids70/serials_source_list.php?db=mechtrans-set-c
EBSCO: http://www.ebscohost.com/titleLists/a9h-journals.pdf
Copernicus: http://journals.indexcopernicus.com/karta.php

The papers published in this journal can be visualized on the "Dunarea de Jos" University of Galati site, the Faculty of Metallurgy, Material Science and Environment, page: www.fimm.ugal.ro.

Publisher's Name and Address:
Contact person: Antoaneta Căpraru
Galati University Press - GUP
47 Domneasca St., 800008 - Galati, Romania
Phone:+40 336 130139, Fax: +40 236 461353
Email: gup@ugal.ro

Editor's Name and Address:
Prof. Dr. Eng. Marian BORDEI
Dunarea de Jos University of Galati, Faculty of Metallurgy, Materials Science and Environment
111 Domneasca St., 800201 - Galati, Romania
Phone: +40 336 130223, Phone/Fax: +40 236 460750
Email: mbordei@ugal.ro

AFFILIATED WITH:

- *ROMANIAN SOCIETY FOR METALLURGY*
- *ROMANIAN SOCIETY FOR CHEMISTRY*
- *ROMANIAN SOCIETY FOR BIOMATERIALS*
- *ROMANIAN TECHNICAL FOUNDRY SOCIETY*
- *THE MATERIALS INFORMATION SOCIETY (ASM INTERNATIONAL)*

Annual subscription (4 issues per year)

Edited under the care of
Faculty of
METALLURGY, MATERIALS SCIENCE AND ENVIRONMENT

Edited date: 30.03.2012
Issues number: 200
Printed by
Galati University Press
accredited CNCSIS
47 Domnească Street, 800036
Galati, Romania